

ABSTRACT

Title of Document: THE UNCERTAINTY OF SPACEBORNE OBSERVATION OF VEGETATION STRUCTURE IN THE TAIGA-TUNDRA ECOTONE: A CASE STUDY IN NORTHERN SIBERIA.

Paul Mannix Montesano, Doctor of Philosophy, 2015

Directed By: Dr. Ralph Dubayah, Department of Geographical Sciences

The ability to characterize vegetation structure in the taiga-tundra ecotone (TTE) at fine spatial scales is critical given its heterogeneity and the central role of its patterns on ecological processes in the high northern latitudes and global change scenarios. This research focuses on quantifying the uncertainty of TTE forest structure observations from remote sensing at fine spatial scales. I first quantify the uncertainty of forest biomass estimates from current airborne and spaceborne active remote sensing systems and a planned spaceborne LiDAR (ICESat-2) across sparse forest gradients. At plot-scales, current spaceborne models of biomass either explain less than a third of model variation or have biomass estimate uncertainties ranging from 50-100%. Simulations of returns from the planned ICESat-2 for a similar gradient show the uncertainty of near-term estimates vary according to the ground length along which returns are collected. The 50m length optimized the resolution of forest structure, for which there is a trade-off between horizontal precision of the measurement and vertical structure detail. At this scale biomass error ranges from 20-50%, which precludes identifying actual differences in aboveground live biomass density at 10 Mg·ha⁻¹ intervals. These broad plot-scale uncertainties in structure from current and planned sensors provided the basis for examining a data integration technique with multiple sensors to measure the structure of sparse TTE forests. Spaceborne estimates of canopy height used complementary

surface elevation measurements from passive optical and LiDAR to provide a means for directly measuring TTE forest height from spaceborne sensors. This spaceborne approach to estimating forest height was deployed to assess the spaceborne potential for examining the patterns of TTE forest structure explained with a conceptual biogeographic model linking TTE patterns and its dynamics. A patch-based analysis was used to scale estimates of TTE forest structure from multiple sensors and provided a means to simultaneously examine the horizontal and vertical structure of groups of TTE trees. The uncertainty of forest patch height estimates provides focus for improving spaceborne depictions of TTE structure patterns associated with recent change that may explain the variability of this change and the vulnerability of TTE forest structure.

THE UNCERTAINTY OF SPACEBORNE OBSERVATION OF VEGETATION
STRUCTURE IN THE TAIGA-TUNDRA ECOTONE:
A CASE STUDY IN NORTHERN SIBERIA.

By

Paul Mannix Montesano

Dissertation submitted to the Faculty of the Graduate School of the
University of Maryland, College Park, in partial fulfillment
of the requirements for the degree of
Doctor of Philosophy
2015

Advisory Committee:
Professor Ralph Dubayah, Chair
Professor Eric Kasischke
Dr. Guoqing Sun
Dr. Bruce Cook
Dean's Representative:
Professor Kaye Brubaker

© Copyright by
Paul Mannix Montesano
2015

Dedication

For Anahí Esmeralda Montesano – I finished before you started. Let me know when you get around to reading this. And don't forget to run those rivers.

Acknowledgments

I'd like to acknowledge my committee for their guidance at various stages of this research: Ralph Dubayah, Guoqing Sun, Bruce Cook, Eric Kasischke and Kaye Brubaker. Additionally, I'd like to thank the coauthors of the published portions of this work that were not part of my committee but provided critical guidance nonetheless: Ross Nelson, Jacqueline Rosette, Peter North, Erik Næsset, Slava Kharuk, and Jon Ranson. I also appreciate the important contributions of those with whom I collected field data used in this research: Wenli Huang, Sergei Im, Pasha Oskorbin, Jeremy Rubio, Wenjian Ni, Mukhtar Naurzbaev, Feng Zhao, and Zhiyu Zhang. Special thanks go out to the Russian scientists Slava Kharuk, Mukhtar Naerzbaev, Sergei Im, and Pasha Oskorbin for their gracious and productive collaborations with myself, Jon Ranson, Guoqing Sun and Ross Nelson over the years, and for helping see us all safely down river many times.

Table of Contents

Dedication	ii
Acknowledgments.....	iii
Table of Contents	iv
List of Tables	vii
List of Figures	viii
Chapter 1: Introduction	1
1.1. Overview	1
1.2. Research Goals and Questions	1
1.3. Background	2
1.3.1. The Taiga-Tundra Ecotone	2
1.3.2. TTE Vegetation Variability: Site and Climate Controls	3
1.3.3. TTE Vegetation of Northern Siberia: Biophysical Relevance and Recent Changes	4
1.3.4. Uncertainty in Spaceborne Observation of TTE Vegetation Structure	6
1.4. Dissertation Organization	7
Chapter 2: The Uncertainty of Biomass Estimates from LiDAR and SAR Across a Boreal Forest Structure Gradient	10
2.1. Abstract	10
2.2. Introduction & Background	10
2.3. Methods.....	14
2.3.1. Remote Sensing Data	14
2.3.2. Ground Reference Inventories	15
2.3.3. LiDAR Waveform Processing	17
2.3.4. Empirical Modeling: Linking Remote Sensing and Ground Reference Measurements	19
2.3.5. Uncertainty Analysis.....	20
2.4. Results.....	21
2.4.1. Empirical Models of AGB vs. Metrics	21
2.4.2. Error and Error Uncertainty within AGB Bins	23
2.5. Discussion	27
2.5.1. Limited Ability to Discern Sparse Forests at Plot Scale	27
2.5.2. Implications for Understanding TTE Vegetation Structure Change	28
2.5.3. Limitations of AGB Uncertainty Estimates	29
2.6. Conclusions.....	31
Chapter 3: The Uncertainty of Biomass Estimates from Modeled ICESat-2 Returns Across a Boreal Forest Gradient.....	33
3.1. Abstract	33
3.2. Introduction.....	34
3.2.1. Global Relevance of the Taiga-Tundra Ecotone	34
3.2.2. Forest Structure in Northern Siberia	35
3.2.3. LiDAR Remote Sensing of Vegetation.....	35
3.2.4. The FLIGHT Model.....	38
3.3. Methods.....	40
3.3.1. Overview.....	40
3.3.2. ICESat-2 ATLAS Parameters for FLIGHT	40
3.3.3. Forest Stand Parameters for FLIGHT	42
3.3.4. Canopy Height Algorithm.....	45
3.3.5. Empirical Modeling	46
3.3.6. Uncertainty Analysis.....	47
3.4. Results.....	47

3.4.1. Simulated Photon Returns.....	47
3.4.2. Simulated Height Metrics	50
3.4.3. Distribution of Bootstrapped R^2 of Predictive Models	53
3.4.4. Error and Error Uncertainty of Derived AGB.....	54
3.5. Discussion	56
3.5.1. Photon Returns & Link-scales	57
3.5.2. Simulated Height Metrics & AGB Uncertainty	58
3.5.3. Implications of AGB Uncertainty	60
3.5.4. Limitations of AGB Uncertainty Estimates	60
3.6. Conclusions.....	62
Chapter 4: The Uncertainty of Plot-Scale Forest Height Estimates from Complementary Spaceborne Observations in the Taiga-Tundra Ecotone	63
4.1. Abstract	63
4.2. Introduction.....	63
4.3. Methods.....	68
4.3.1. Field Data.....	68
4.3.2. HRSI Data Acquisition and Processing	70
4.3.3. GLAS Data Acquisition and Processing	71
4.3.4. Analysis.....	72
4.4. Results.....	74
4.5. Discussion	77
4.5.1. Spaceborne Canopy Height and Its Sources of Uncertainty	77
4.5.2. Future Work	79
4.6. Conclusions.....	81
Chapter 5: Spaceborne Potential for Examining Taiga-Tundra Ecotone Form and Vulnerability	82
5.1. Abstract	82
5.2. Introduction.....	83
5.2.1. The Structure of Vegetation in the TTE.....	83
5.2.2. Influence of TTE Structure on Dynamics	83
5.2.3. A TTE Conceptual Model.....	84
5.2.4. The Scale of TTE Observation.....	85
5.2.5. The Uncertainty of Spaceborne Data of TTE Structure	85
5.2.6. Patch-based TTE Analysis	86
5.2.7. Towards Identifying TTE Form: Remote Sensing Data Integration and Scaling	86
5.3. Methods.....	87
5.3.1. Study Area	87
5.3.2. Remote Sensing Data Acquisition and Processing	89
5.3.3. Forest Patch Delineation and Attribution.....	91
5.3.4. Predicting Forest Patch Height Directly at LiDAR footprints	92
5.3.5. Modeling Forest Patch Height Indirectly (without LiDAR Samples).....	92
5.4. Results.....	93
5.4.1. Forest Patch Delineation and Direct Sample Density	93
5.4.2. Comparison of Stand Height Calibration and Validation Data.....	94
5.4.3. Indirect Forest Patch Height Estimates	96
5.4.4. Uncertainty of Forest Patch Height Estimates	97
5.5. Discussion	100
5.5.1. Forest Patch Height Uncertainty	100
5.5.2. Improving the Modeling of Forest Patch Height	102
5.5.3. Spaceborne Sensing of TTE Form	103
5.5.4. Integrating Horizontal and Vertical Vegetation Structure by Forest Patch.....	103
5.5.5. Implications for Understanding TTE Structure Vulnerability	104

5.6. Conclusions.....	106
Chapter 6: Conclusion.....	107
6.1. Summary of Findings.....	107
6.2. Synthesis and Implications of Findings	109
6.2.1. Synthesis	109
6.2.2. Importance of resolving current TTE structure.....	110
6.2.3. Emerging Potential for Identifying TTE Structure Vulnerability	111
Appendix: Description of Field Sites.....	113
A.1. Introduction.....	113
A.2. Central Maine Field Sites.....	113
A.3. Siberia Field Sites	114
A.4. Norway Field Sites.....	115
Bibliography	122

List of Tables

Table 2-1. Summary of the airborne and spaceborne systems that provided remote sensing data for this study, including the metrics used for this analysis.

Table 3-1. Summary of the parameters used by FLIGHT to simulate photon transport from the planned ATLAS instrument.

Table 3-2. Solar and atmosphere parameters for model simulations with sensor at nadir.

Table 3-3. Summary of the forest stand parameters used for model simulations. Parameters are derived from unpublished field data and previous studies in Larix forests (Bjarnadottir et al., 2007; Kobayashi et al., 2007; Iida et al. 2009; Xue et al. 2011; Wolf et al., 2011).

Table 5-1. Summary of datasets used to delineate or attribute forest patches.

List of Figures

Figure 2-1. Locations in Eurasia and central Maine of ground reference inventories of vegetation structure at LiDAR footprints.

Figure 2-2. Example of an original GLAS waveform and the adjusted “Gaussian-reduced” (GR) waveform that resulted from subtracting the portion of the Gaussian peak above ground elevation from the original GLAS waveform.

Figure 2-3. Plot matrix showing the empirical models used to predict AGB from airborne and spaceborne remote sensing metrics.

Figure 2-4. Each sensor’s results are reported by column. The first row shows the histograms of ground reference plots used in comparison with each sensor’s metrics across a 0-100 Mg·ha⁻¹ structure gradient. The gray bars of the histograms span 20 Mg·ha⁻¹ bins used to report airborne results, and are overlaid with white-outlined bars used to report spaceborne results. Rows 2-4 show error plots in relative terms (RMSE %). Rows 5-7 show error plots in absolute terms (RMSE). Each column’s plot is set up so that each AGB bin aligns vertically with the plot below.

Figure 3-1. Diagram showing the relationship between initial plot-level data and the input FLIGHT parameters used to simulate forest stands for AGB intervals from 10-100 Mg·ha⁻¹.

Figure 3-2. Plots showing how FLIGHT input forest stand parameters varied for each AGB bin. DBH = diameter at breast height (1.3m); FCC = fractional crown cover; PAI = plant area index.

Figure 3-3. (a) An example of simulated returns from FLIGHT along a link-scale (50m). (b) The corresponding histogram of the vertical distribution (0.25m bins) of these returns aggregated for the link-scale. The height on each plot’s Y-axis refers to the height above the bin identified as representing the ground surface.

Figure 3-4. (a) Bar plot of the proportion of simulated LiDAR shots for which there were single or multiple photons returned per shot. (b) Stacked bar plot of the proportion of simulated LiDAR shots for which single or multiple signal and noise photons were returned per shot. Each plot shows proportions across all AGB bins and link scales.

Figure 3-5. A plot matrix showing the distributions of signal photon across all AGB bins at each link-scale.

Figure 3-6. Violin plots showing the distribution of height metrics from simulated returns within each 10 Mg·ha⁻¹ AGB bin for each link-scale. The black dots represent the mean metric value for a given AGB bin and the dashed line depicts the model fit to those mean values.

Figure 3-7. Violin plots showing the distribution of 1000 R2MC values from fitting 1000 empirical models to a randomized transect across a gradient of AGB values. Each random transect was composed of 10 points, where each point was derived from a random selection of a single simulated height within each of the 10 AGB bins.

Figure 3-8. Ribbon plots showing the error (RMSE) and error uncertainty in (a) absolute and (b) relative terms of AGB derived from height metrics for each AGB bin. Note (1) that the rf ribbons for the 20m and 30m link-scales are not shown because the models on which they were based explained < 20% of overall

variation, and (2) the dotted lines, which represent 50% (upper line) and 20% (lower line) error, are shown for reference.

Figure 4-1. The northern Siberia study area showing the spatial coverage of Worldview-1 digital surface models, the spaceborne LiDAR footprints at non-forest sites, and the forested areas where spaceborne LiDAR footprint field sampling was carried out.

Figure 4-2. Histograms showing the distribution of field measured tree heights (Left) and the stem density of trees (Right) for trees >3 cm DBH in the 33 forested field plots centered on GLAS footprints.

Figure 4-3. (a) The relationship of ground surface elevation measurements from GLAS and HRSIWV1 DSMs in Non-Forest and Forest cover types. The 1-to-1 line (dotted) is shown for reference; (b) The distributions of the bootstrapped model RMSD in ground elevation measurements from GLAS and HRSIWV1 DSMs in Non-Forest (0.90 m–1.06 m, 95% CI) and Forest (2.26 m–3.40 m, 95% CI) cover types.

Figure 4-4. (a) The plot showing the linear model for predicting plot-scale maximum canopy height from spaceborne canopy height. The 1-to-1 line (dotted) is shown for reference; (b) the distributions of the bootstrapped R² and RMSE for the canopy height linear model in (a).

Figure 4-5. Histograms of the distributions of spaceborne- and plot-derived maximum canopy height at the scale of an individual field plot.

Figure 5-1. Study area in northern Siberia showing the 9 sites for which forest patches were examined (red boxes) and the field sites along the Kotuykan River (green dots) at which individual tree height measurements in circular plots coincident with ICESat-GLAS LiDAR footprints were collected.

Figure 5-2. (a) The distributions of forest patch size in hectares according to height attribution method. (b) Violin plots, overlain with dots representing individual patches (red), of the distribution of direct height sample density for forest patch size group.

Figure 5-3. (a) Histogram of mean plot and stand heights from calibration and validation data. (b) Map of locations of calibration and validation sites in northern Siberia with the number of stands or plots associated with each site. The circles representing general site locations are sized according to the number of stands. (c) Notched boxplots showing the 25th, 50th, and 75th percentiles as horizontal lines and 1.5 times the interquartile range as vertical lines. Notches roughly indicate the 95% confidence interval.

Figure 5-4. Results from Random Forest indirect forest patch height estimation for 5 spaceborne data predictor sets.

Figure 5-5. The bootstrap-derived distributions of Random Forest model (a) R² and (b) RMSE for the indirect forest patch height prediction method whereby all spaceborne variables were used to predict maximum and mean forest patch height.

Figure 5-6. (a) Patch height and 95% prediction intervals (grey lines) for patches from direct prediction and indirect prediction shown across the continuum of patch sizes. (b) Distributions of relative prediction error (95% prediction interval) for patch height predictions.

Chapter 1: Introduction

1.1. Overview

Earth's forests and the climate system are linked through interactions that remain the subject of intense study, because they affect human well-being. These interactions, both biogeochemical and biogeophysical, are controlled in part by the vertical and horizontal distribution of canopy elements (structure) of forest vegetation spatially, seasonally, and inter-annually. Changes in these interactions are often first observed at biome boundaries. The boundary between the boreal (taiga) and tundra biomes in the high northern latitudes (HNL) is an ecological transition zone (ecotone) known as the taiga-tundra ecotone (TTE) that has experienced particularly strong regional surface temperature warming. Examining the characteristics of forest structure in the TTE is critical for understanding HNL vegetation's responses to, and effects on, climate and the consequences for human well-being.

1.2. Research Goals and Questions

An understanding of how current spaceborne remote sensing tools characterize TTE vegetation structure in Siberia is needed. This need is driven by recent, widespread and variable vegetation change within the Siberian TTE, whose forests are on the leading edge of recent surface warming, are associated with permafrost, and coincide with vast quantities of belowground carbon. The ability to characterize TTE vegetation structure is particularly critical given the central role of TTE vegetation structure patterns in determining ecological processes in the HNL and in influencing global change scenarios.

The goal is to evaluate the uncertainty of current and planned spaceborne remote sensing for monitoring vegetation structure across sparse forest gradients, integrate spaceborne measurements of vegetation characteristics in a data fusion approach, and apply this approach to evaluate forest patch height and its uncertainty within the TTE of northern Siberia. This uncertainty will be examined in light of a conceptual model of regional vegetation structure to assess the potential of spaceborne maps for

depicting ecotone form and TTE forest structure vulnerability. Assessing the uncertainty of spaceborne observations of vegetation structure at the fine spatial scales (10's of meters) at which it changes in the TTE is a first step in understanding how structural variability influences broader ecological processes. In this study, both forest aboveground live biomass density (AGB) and forest canopy height will be the vegetation structural attributes of interest. This study's goal is addressed with the following three research questions:

1. How do the estimates of AGB error and AGB error uncertainty from LiDAR and SAR vary across a vegetation structure gradient in sparse forests?
2. How can estimates of forest structure from spaceborne data be integrated and scaled in a data fusion approach to characterize structure across sparse forest gradients?
3. How well do the estimates of forest patch height and its uncertainty from spaceborne remote sensing depict ecotone form across a latitudinal forest gradient in the TTE in northern Siberia?

1.3. Background

1.3.1. The Taiga-Tundra Ecotone

Earth's longest ecological transition zone (ecotone) between terrestrial biomes, the taiga-tundra ecotone (TTE) of the circumpolar boreal region in the high northern latitudes (HNL) extends for 13,400 km across two continents, varies widely in terms of position and pattern, covers approximately 1.9 million square kilometers, holds vast amounts of subsurface carbon, and can amplify warming through decreases in surface albedo (Bonan, 2008; Callaghan, Werkman, & Crawford, 2002b; Swann, Fung, Levis, Bonan, & Doney, 2010). Generally, the TTE extends from the continuously forested region of the boreal biome northward to the northernmost position of arboreal growth (Payette, Fortin, & Gamache, 2001). However, this transition zone is discontinuous and non-uniform, as reflected in a recent map of the circumpolar TTE extent derived from MODIS data (Ranson, Montesano, & Nelson, 2011).

Paleoecological data suggest this vegetation regime has not been static throughout the last 10,000 years, but has both advanced northward and retreated southward in response to changing climate (Bonan,

2008; Callaghan, Werkman, & Crawford, 2002b; K. B. Liu, 1990; Payette & Gagnon, 1985; Swann et al., 2010). This evidence indicates that during a warming episode nearly 5000 years ago, forested patches appeared in the tundra in central Canada during a transition that lasted ~150 years (G. M. MacDonald, Edwards, Moser, Pienitz, & Smol, 1993; Payette et al., 2001). In northern Siberia, Holocene increases in tree cover were asynchronous, perhaps emerging from refugial stands, while vertical growth has been evident since the first half of the 20th century (Esper & Schweingruber, 2004; G. M. MacDonald, Kremenetski, & Beilman, 2008; Payette, Eronen, & Jasinski, 2002; Ranson et al., 2011).

1.3.2. TTE Vegetation Variability: Site and Climate Controls

Vegetation within the TTE is subjected to a short growing season, varying topographic and edaphic conditions, and changes with shifts in climate (G. MacDonald et al., 2000; Wolfe et al., 2000). Evidence of paleoclimate summer temperature suggests that Arctic summers are warmer now than any time in the last 4 centuries (Chapin, 2005; Overpeck et al., 1997). Recent studies have documented these changes in TTE vegetation under a shifting climate (Elmendorf et al., 2012; Esper & Schweingruber, 2004; M. Harsch, Hulme, McGlone, & Duncan, 2009; Kirilyanov et al., 2011; Sturm, Racine, & Tape, 2001; Tape, Sturm, & Racine, 2006; Vaganov, Hughes, Kirilyanov, Schweingruber, & Silkin, 1999). Many of these studies demonstrate that the ways in which the TTE ecosystem responds to warming depend on changes in the structure and productivity of vegetation, as well as the vegetation's disturbance regime (S. Goetz et al., 2010; Payette et al., 2001). Furthermore, the response of ecotone vegetation to climate depends on the magnitude and rate of environmental change, the sensitivity of dominant species (physiological tolerance), and the resilience of these species to change (Risser, 1995).

While climate is important for determining the extent and pattern of the TTE and the distribution of its vegetation, other controlling factors include local-scale spatial structure of vegetation, species dispersal mechanisms and regenerative potential (Gamache & Payette, 2005; F.-K. Holtmeier & Broll, 2005; K. B. Liu, 1990; Payette & Gagnon, 1985). The geographic variability in site conditions thus influences the spatial heterogeneity of vegetation structure in the TTE (Bergen et al., 2009; Hall et al.,

2011; Ropars & Boudreau, 2012), creating feedbacks to ecosystem structure and function that may also vary spatially. The spatial patterns of vegetation, and their variability, may help explain the variability in vegetation dynamics in the TTE (M. A. Harsch & Bader, 2011).

The structure of vegetation in the TTE also affects climate through a number of feedback mechanisms, and the net effect of vegetation structure's influence on climate is not well understood (Bonan, 2008; Bonan, Pollard, & Thompson, 1992; Chapin et al., 2000; G. MacDonald et al., 2000; Wolfe et al., 2000). These feedback mechanisms can involve vegetation dynamics associated with changes in disturbance regimes (V. I. Kharuk, Ranson, Dvinskaya, & Im, 2011), temperature (A. Soja et al., 2007), hydrology (Kajimoto, Osawa, Usoltsev, & Abaimov, 2009; Miyahara, Takenaka, Tomioka, & Ohta, 2011), and surface albedo (Beck, Goetz, et al., 2011a; Betts, 2000; Loranty, Goetz, & Beck, 2011; Shuman, Shugart, & O'Halloran, 2011; C. Thompson, Beringer, Chapin, & McGuire, 2004). The carbon storage of the unique larch-permafrost coupled system of northern boreal Siberia is considered important to global carbon storage and regional climate (Post et al., 2009; N. Zhang, Yasunari, & Ohta, 2011).

1.3.3. TTE Vegetation of Northern Siberia: Biophysical Relevance and Recent Changes

The land surface in the TTE of northern Siberia has experienced rapid warming at least twice that of the average for global land areas (Groisman & Soja, 2009), about 2-3 degrees C (ACIA, 2005). Modeling studies on vegetation feedbacks to permafrost extent and active layer depth, timing of carbon feedback, fire activity, temperature, carbon storage, growing season length and climate help explain the relevance of potential changes in vegetation distribution and structure to ecosystem dynamics in the HNL.

Model projections of the strength and timing of a permafrost feedback to climate, accounting for vegetation characteristics, suggest a central role for high latitude vegetation structure in determining the magnitude of changes to the global carbon cycle (Schaefer, Zhang, Bruhwiler, & Barrett, 2011). In this region, the extent of continuous permafrost influences the distribution of vegetation (Lloyd, Bunn, & Berner, 2011; Schulze et al., 2012; Sugimoto, Yanagisawa, Naito, Fujita, & Maximov, 2002; Tchebakova, Parfenova, & Soja, 2009; N. Zhang et al., 2011). The strength and timing of a climate

feedback from permafrost-bound carbon is a function of vegetation structure (Epstein et al., 2004; Jorgenson et al., 2010; Lawrence & Swenson, 2011; Schaefer et al., 2011). A study on the potential impact of large-scale vegetation structure changes in the Arctic on boreal climate revealed that the strength and timing of land-atmosphere feedbacks were sensitive to shrub height, and that taller shrubs had larger effects on soil temperature and permafrost conditions (Bonfils et al., 2012). Liess et al. explored the ways in which the climate responds to boreal forest expansion, finding that modest forest expansion along the northern boreal edge resulted in summertime warming, enhancing the Arctic frontal zone (Liess, Snyder, & Harding, 2011). Forest expansion imposed on the modeling simulations was subtle and spatially variable, yet led to an increase in AGB, leaf area, and lower surface albedo, among other changes. A modeled increase in growing season length showed greatest losses of soil carbon in areas with more vegetation (Euskirchen et al., 2006). Modeled expansion of forests yielded a positive feedback with climate, from decreased albedo and increased transpiration, that amplified warming when operating in unison with sea-ice processes (Swann et al., 2010). However, forest expansion will be regionally variable because of spatial variability in soil and climate (G. M. MacDonald et al., 2008). Finally, multiple studies explain the need for understanding vegetation height and cover, which may play an important role in determining the strength of the amplifying effect on climate warming (Blok et al., 2010; 2011; Lawrence & Swenson, 2011; Loranty & Goetz, 2012; Myers-Smith et al., 2011).

The modeling results that demonstrate the potential strengths and consequences of changes in vegetation structure for ecosystem dynamics in the HNL are underscored by multiple lines of evidence from plot and satellite studies directly observing change. This evidence highlights recent vegetation changes in the TTE in general and in northern Siberia in particular. Plot-scale vegetation changes in the HNL have been studied with field experiments while multi-scale studies of changes in vegetation productivity and structure have been carried out with satellite data analyses.

Ground studies show that in central Siberia, dark-needle conifers are expanding into *Larix*-dominated forests, and canopy-closure and expansion of *Larix* in tundra has been observed (V. I. Kharuk, Dvinskaya, Ranson, & Im, 2005; V. I. Kharuk, Ranson, Im, & Naurzbaev, 2006). In the polar Urals of

northwestern Siberia, a recent study reports marked increase in woody growth as well as increases in areas supporting sparse *Larix* trees following increases in open and closed canopy *Larix* woodlands in those areas through the twentieth century (Devi et al., 2008; Shiyatov & Mazepa, 2012). These changes in sparse *Larix* forest structure were observed over long-term studies that examined changes in vegetation throughout the first and second halves of the 20th century. Mazepa and Devi (2007) discussed the changes in arboreal growth form, from shrub-like to prostrate, of *Larix* in the treeline ecotone in the polar Urals (Mazepa & Devi, 2007). Other dendrologic studies linked observed tree ring growth of *Larix* associated with permafrost in the TTE of northern Siberia to be coincident with increased summer temperatures (Vaganov & Kirilyanov, 2009).

Satellite observations support ground studies of vegetation change. Recent findings suggest warming-induced productivity increases are likely in northern Siberian taiga (Lloyd et al., 2011). In western Siberia increased shrub growth has been associated with increased summer temperatures in the second half of the 20th century and has been linked to increased photosynthetic greening as documented by satellites (Forbes, Fauria, & Zetterberg, 2010). This growth is related to the position of specific summer air masses and may create new vegetation structure regimes (Macias-Fauria, Forbes, Zetterberg, & Kumpula, 2012). Berner et al. demonstrated with dendrochronology and satellite data that plant growth increased with temperature in northeastern Siberia (Berner, Beck, Bunn, & Goetz, 2013). In north-central Siberia Landsat and high-resolution satellite time-series have been used to document the expansion of tall shrubs and trees in the TTE of northern Siberia in recent decades (Frost & Epstein, 2014; G. Sun, Ranson, Kharuk, & Kovacs, 2004; M. Urban et al., 2014).

1.3.4. Uncertainty in Spaceborne Observation of TTE Vegetation Structure

Biogeographic studies in the HNL stress that fine-scale, site-based monitoring is critical for understanding the nature of variation in TTE vegetation characteristics and dynamics (Epstein et al., 2004; Harper et al., 2011; Hofgaard, Harper, & Golubeva, 2012). The authors also note the utility of spaceborne sensing for monitoring changes in structure while explaining that coarse-scale data (i.e.

Ranson et al. 2011) may not resolve the critical site-level detail needed to fully understand TTE vegetation characteristics, variability, dynamics and vulnerability to structural changes. Fine-scale spaceborne sensing of TTE vegetation structure across the circumpolar domain of the TTE is a challenge because the magnitude and uncertainty of measurement error may mask measured differences in structure. It is necessary to reduce this uncertainty because the deviation of current coarse-scale observations and model predictions from ground data can be larger than the expected changes in vegetation structure (Hofgaard et al., 2012; Hofgaard, Tømmervik, Rees, & Hanssen, 2013).

The recommendations from biogeographers for standardized techniques that improve estimates of TTE characteristics echo the common call for the use of remote sensing data across the circumpolar domain for collecting vegetation observations (Callaghan, Werkman, & Crawford, 2002b; Danby, 2011; Hofgaard et al., 2012; Hofgaard & Harper, 2011; F.-K. Holtmeier & Broll, 2005; Hufkens, Scheunders, & Ceulemans, 2009). These improved spaceborne sensing techniques for estimating TTE vegetation should include the magnitude and uncertainty associated with measurement error at scales at which spatial patterns of vegetation change. By quantifying spaceborne uncertainty of TTE vegetation structure, we can work to identify where reductions in uncertainty of structure will have the greatest potential for understanding variations in spatial patterns of structure that are linked to variations in responses of TTE vegetation to climatic drivers. A careful examination of the spaceborne uncertainty of TTE vegetation structure is warranted to appropriately answer the call for quantifying its current state and vulnerability that are modified by domain-wide temperature increases and site-specific environmental factors.

1.4. Dissertation Organization

The three research questions described in Section 1.2 are addressed in the following four chapters. These chapters present original research aimed at examining the uncertainty of spaceborne measurements of vegetation structure across sparse forest gradients, and the implications of this uncertainty for evaluating forest structure patterns in the taiga-tundra ecotone.

Chapter 2 addresses the first research question. Here, I aggregated ground reference AGB across sites in central Maine, Aurskog, Norway and northern Siberia. This ground reference data were linked to current airborne and spaceborne LiDAR and SAR data to examine the uncertainty of these remote sensing measurements across a statistical gradient of AGB consistent with a gradient of AGB found across the TTE in northern Siberia. The work is published in the journal *Remote Sensing of Environment*.

Chapter 3 also addresses the first research question. However, in this chapter I used a radiative transfer model to examine simulated measurements consistent with that of a planned near-term spaceborne LiDAR (ICESat-2). The uncertainty of these simulated measurements was examined across the same statistical gradient of AGB as that of Chapter 1. The AGB gradient used to initialize model simulations was derived from field data acquired in northern Siberian *Larix* forests. This chapter is also published in *Remote Sensing of Environment*.

The uncertainty in spaceborne measurements of sparse vegetation structure in Chapters 2 & 3 led to the methodology presented in Chapter 4. In this chapter I present an approach to estimate spaceborne canopy height with complementary spaceborne measurements. This work addressed the second research question by integrating spaceborne LiDAR and high resolution spaceborne imagery to estimate canopy height at the scale of a field plot. The canopy heights examined were those coincident with field plots in the sparse *Larix* forests of northern Siberia along the Kotuykan River. This chapter is published in a special issue of the journal *Remote Sensing*, entitled “*Remote Sensing of Changing Northern High Latitude Ecosystems*.”

Chapter 5 is the final research chapter of the dissertation. This chapter draws from the uncertainty findings and methodological approaches discussed in the previous three chapters. Here, I addressed both the second and third questions. I integrated spaceborne measurements of vegetation structure and scaled them to forest patches mapped across sites in the TTE north of the Kheta River in northern Siberia. I examined the estimates of uncertainty in forest patch height using a conceptual model of ecotone form. I explain how this conceptual model provides focus for TTE mapping, in that maps of TTE spatial patterns may yield the spatial extent of TTE vulnerability. There is specific potential for a

spaceborne mapping approach to map these spatial patterns by reducing the uncertainty of forest patch height estimates so as to distinguish clear gradients of forest patch heights associated with diffuse TTE form.

The final two portions of this dissertation include the concluding chapter and the appendix. The concluding chapter summarizes the finding of the previous four research chapters, provides a synthesis of these findings, summarizes the importance of resolving current TTE structure, and highlights the emerging potential for understanding the vulnerability of forest structure in the TTE. The appendix offers background on individual tree measurements gathered during the various field campaigns that provided ground reference for all studies in this dissertation.

Chapter 2: The Uncertainty of Biomass Estimates from LiDAR and SAR

Across a Boreal Forest Structure Gradient

2.1. Abstract

In this study, we examined the uncertainty of aboveground live biomass (AGB) estimates based on light detection and ranging (LiDAR) and synthetic aperture radar (SAR) measurements distributed across a low-biomass vegetation structure gradient from forest to non-forest in boreal-like ecosystems. The conifer-dominant structure gradient was compiled from ground data amassed from multiple field expeditions in central Maine (USA), Aurskog (Norway), and across central Siberia (Russia). Single variable empirical models were built to model AGB from remote sensing metrics. Using these models, we calculated a root mean square error (RMSE) and a 95% confidence interval (CI) of the RMSE from the difference between the remote sensing AGB predictions and the ground reference AGB estimates within AGB intervals across a 0-100 Mg·ha⁻¹ boreal forest structure gradient. The results show that the error in AGB predictions (RMSE) and the error uncertainty (the CI) from LiDAR and SAR change across a forest gradient. The errors of airborne LiDAR and SAR metrics and spaceborne LiDAR platforms show a general trend of reduced relative errors as AGB magnitudes increase, particularly from 0 – 60 Mg·ha⁻¹. Empirical models relating spaceborne metrics to AGB and estimates of spaceborne LiDAR error uncertainty demonstrate the difficulty of characterizing differences in AGB at the site-level with current spaceborne sensors, particularly below 80 Mg·ha⁻¹ with less than 50-100% error.

2.2. Introduction & Background

Characterizing differences in vegetation structure, such as biomass, across a vegetation gradient can reveal spatial patterns in forests and their changes over time. Vegetation structure, which influences biodiversity and climate, varies over space and time (Bonan, Chapin, & Thompson, 1995; Callaghan, Werkman, & Crawford, 2002b; Epstein et al., 2004; Hofgaard et al., 2010; F. K. Holtmeier, 2009; F.-K.

Holtmeier & Broll, 2005; Risser, 1995). This variation is manifested as gradients in vegetation structure. Temporally, gradients can occur as vegetation recovers following a disturbance event or as vegetation structure shifts in response to temporal changes in environmental conditions. Spatially, vegetation structure gradients coincide with geographic variation in environmental factors, which can influence vegetation performance such as growth, regeneration and mortality (Bonan et al., 1992; Lorant & Goetz, 2012; Sveinbjörnsson, Hofgaard, & Lloyd, 2002). The differences in vegetation structure at various time periods and geographic positions, and its effects on biodiversity and climate, can reveal the degree to which vegetation structure contributes to ecosystem dynamics (Callaghan, Werkman, & Crawford, 2002b; Dobson et al., 1992; Dubayah & Drake, 2000; M. Lefsky, Cohen, Parker, & Harding, 2002; K. C. McDonald, Dobson, & Ulaby, 1990).

Vegetation structure across the sparse forests of the circumpolar taiga-tundra ecotone (TTE), at the convergence of the boreal forest and un-forested tundra, is linked to climate (Bonan et al., 1992). Recent changes in climate have brought about changes in arctic ecosystems associated with the TTE (ACIA, 2004; S. Goetz & Dubayah, 2011). These recent changes in TTE vegetation throughout the circumpolar high latitudes have been widely documented (Beck, Juday, et al., 2011b; Elmendorf et al., 2012; Forbes et al., 2010; Hofgaard et al., 2013; V. I. Kharuk et al., 2006; Macias-Fauria et al., 2012; D. A. Walker et al., 2012). While climate is important for determining the extent and pattern of the TTE and the distribution and structure of its vegetation, other factors such as local-scale spatial structure, species dispersal mechanisms, regenerative potential and non-climatic abiotic factors are also key drivers of its current state and capacity for, and velocity of, change (Callaghan, Crawford, Eronen, Hofgaard, et al., 2002a; Frey, Penman, Hanle, Monni, & Ogle, 2006; Gamache & Payette, 2005; F.-K. Holtmeier & Broll, 2005). This range of drivers makes for diverse conditions of vegetation structure, however, conditions that are evident at local scales can be masked at broad scales (Hofgaard et al., 2012; Woodcock, 2006). As multi-scale shifts in vegetation continue to serve as the expression of changes in environmental conditions brought about by changing climate, there is a need to better quantify their spatial characteristics. These vegetation shifts occur at the local-scale because they are often site-specific, yet

collections of such shifts in vegetation may be evident across the broad scales at which the disturbance is taking place (Callaghan, Werkman, & Crawford, 2002b; Hofgaard et al., 2010). Furthermore, the vegetation shifts that are occurring in the TTE may not coincide with model predictions (Hofgaard et al., 2013). Finally, there is a need to characterize differences in vegetation structure that are biophysically and ecologically relevant in order to understand the feedbacks of vegetation to climate (Bonan et al., 1992; Loranty & Goetz, 2012).

Remote observations of vegetation from active sensors can characterize vegetation structure across a landscape. These characterizations differ depending on the type of active sensing system. Light detection and ranging (LiDAR) and synthetic aperture radar (SAR) provide two general means of assessing vegetation structure remotely. LiDAR provides a direct measure of vegetation canopy and sub-canopy height and density while polarimetric SAR backscatter provides information that mixes signals from the ground surface and the size, shape and orientation of vegetation (Dobson et al., 1992; Dubayah & Drake, 2000; M. Lefsky et al., 2002; K. C. McDonald et al., 1990).

Spaceborne LiDAR and SAR have been used to map and inventory boreal forest structure (R. Nelson et al., 2009; Santoro et al., 2009; Selkowitz, Green, Peterson, & Wylie, 2012; Whitcomb, Moghaddam, McDonald, Kelldorfer, & Podest, 2009). These systems provide a means for broad-scale, synoptic mapping of entire biomes. Consistent, broad scale mapping of the current state of vegetation is the first step in capturing a time series of vegetation structure that facilitates the study of the spatial variation of vegetation structure, its change, and sources and sinks of aboveground carbon (S. Goetz & Dubayah, 2011). In order to capture salient and ecologically relevant changes in vegetation structure, the uncertainty of these remote measurements need to be placed into context with such changes. The measurements can only provide new insight if their errors are small enough to be sufficiently certain that a measured difference in vegetation structure across space or time translates to actual structural differences on the ground. An examination of the remote vegetation structure measurement errors across a gradient would demonstrate the sensitivity of current remote sensing to a range of structural regimes.

A spatial gradient of vegetation structure may occur in AGB as boreal forest transitions to non-forest. Samples of AGB at transect intervals crossing such a transition could provide AGB measurements that span a continuous set of AGB intervals. Similarly, a statistical gradient can be amassed by collecting many measurements at disparate sites representing a variety of AGB conditions similar to those that would be found along a transect crossing a transition of boreal forest to non-forest. Such a statistical gradient of AGB measurements would have similar structure as sites across an actual spatial forest transition.

Uncertainty is a key component of remote sensing studies and applications, and can be defined as ‘the probability of error’ that can be attributed to different sources (Dungan, 2006). This definition highlights two components of a remote sensing measurement; the error of the measurement as well as its probability. The error is represented as a mean value while the probability of this error can be represented as a probability density function (PDF), and helps describe the lack of understanding of the error’s true value (Frey et al., 2006). The focus on the uncertainty of remote measurements of vegetation draws attention to the limits of what these measurements can add to the current understanding of vegetation characteristics, such as structure and extent (Woodcock, 2006). There have been a number of studies quantifying a number of uncertainties, in a variety of ways, from LiDAR and SAR measurements (Ahmed, Siqueira, & Hensley, 2013; Frazer, Magnussen, Wulder, & Niemann, 2011; Gobakken & Næsset, 2009; Hensley et al., 2014; Hodgson & Bresnahan, 2004; Lu et al., 2012; Mascaro, Detto, Asner, & Muller-Landau, 2011; Tinkham et al., 2012). In this study we used spatially coincident ground reference and remote sensing data acquired across a range of boreal forest biomass to evaluate the uncertainty of remote measurements of vegetation structure from LiDAR and SAR across a boreal forest to non-forest structure gradient.

2.3. Methods

2.3.1. Remote Sensing Data

LiDAR and SAR data from both airborne and spaceborne platforms were used in this study to measure vegetation structure across a forest gradient. Table 2-1 provides a summary of each dataset used. Airborne data came from the synthetic aperture radar UAVSAR, the medium footprint waveform Laser Vegetation Imaging Sensor (LVIS) and the small footprint discrete return scanner of Goddard's LiDAR, Hyperspectral, and Thermal Imager (GLiHT) (Blair, Rabine, & Hofton, 1999; Cook et al., 2013; Rosen et al., 2006). Spaceborne data came from ICESat GLAS (Abshire et al., 2005; Zwally et al., 2002) and ALOS PALSAR (Rosenqvist, Shimada, Ito, & Watanabe, 2013). For each study area, there exists both LiDAR and SAR, with the exception of a few ground reference plots in Eurasia for which one of the two remote sensing measurements, from either GLAS or PALSAR, was not available.

Spaceborne data (GLAS and PALSAR) are available from the National Snow and Ice Data Center and the Alaska Satellite Facility, respectively, for the study sites in Eurasia while airborne data (LVIS, UAVSAR and GLiHT) are available from NASA instrument websites (<http://lvis.gsfc.nasa.gov>; <http://uavsar.jpl.nasa.gov>; <http://gliht.gsfc.nasa.gov>). Airborne LiDAR and SAR were spatially coincident in Maine as were spaceborne LiDAR and SAR in Eurasia, however these datasets were generally acquired independent of each other, with the exception of the temporally coincident UAVSAR and LVIS campaigns in Maine in 2009. The UAVSAR data was radiometrically calibrated for viewing geometry and topography (Montesano et al., 2013; Small, 2011).

Table 2-1. Summary of the airborne and spaceborne systems that provided remote sensing data for this study, including the metrics used for this analysis.

Type	Sensor	Study Region	Acquisition Year	Description, metrics
airborne LiDAR	LVIS	Maine	2009	~20m footprint waveform @ 1064nm, (rh90, rh75, rh50)
airborne LiDAR	GLiHT	Maine	2012	small footprint discrete return @ 1550nm, (rh90, rh70, rh50)
spaceborne LiDAR	ICESat GLAS	Eurasia	2003-2006	~60m footprint waveform @ 1064nm, (rh90, rh75, rh50)
airborne SAR	UAVSAR	Maine	2009	~5m full-polarimetric L-band (HH, HV, VV)
spaceborne SAR	ALOS PALSAR	Eurasia	2007-2010	~20m dual-polarimetric L-band (HH, HV)

2.3.2. Ground Reference Inventories

We compiled ground based forest structure measurements from sites across Eurasia and central Maine (Figure 2-1). These measurements of tree diameter at breast height (DBH) and tree height were spatially coincident with remote sensing data, and were acquired for a gradient of boreal forest structure ranging from forested to non-forested, representative of vegetation structure regimes within the TTE. These inventories took place across multiple years at a number of locations to sample trees within a portion of a LiDAR footprint, and infer ground reference forest AGB for each footprint, which was used as a surrogate for vegetation structure.

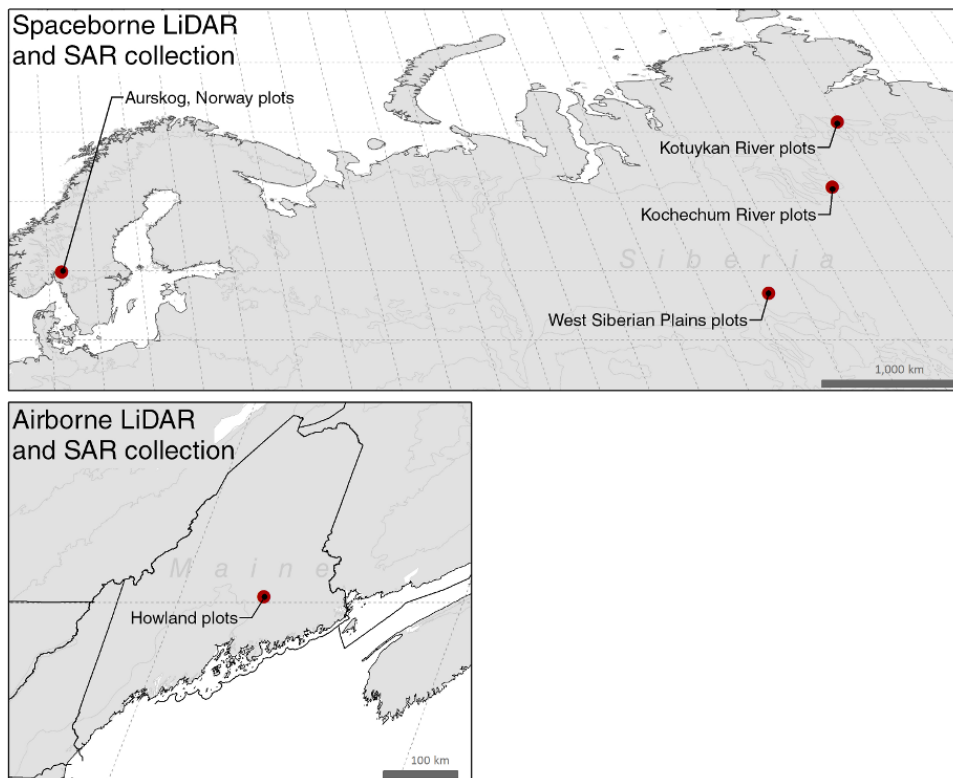


Figure 2-1. Locations in Eurasia and central Maine of ground reference inventories of vegetation structure at LiDAR footprints.

Plots corresponded to either spaceborne or airborne data. Those plots associated with spaceborne data were centered on GLAS footprints and collected from the Kochechum River, Kotuykan River and Western Siberian Plains sites in the summers of 2007, 2008, and 2010, respectively. GLAS footprints in

Aurskog, Norway were surveyed using wall-to-wall airborne laser scanner (ALS) data (Næsset et al., 2011). Plots associated with airborne measurements were collected in the Howland Experimental Forest in central Maine, where plots that were centered on LVIS footprints were surveyed in 2009 and 2011.

Field-derived AGB measurements were collected in circular ground plots within airborne (LVIS) or spaceborne (GLAS) LiDAR sample footprints. These field plots were geo-located to within ~1–3m (airborne LiDAR plots) and ~1-10m (satellite LiDAR plots) of the LiDAR footprint's centroid using a hand-held global positioning system unit. Each LiDAR footprint was assumed to be a circle with a consistent radius for each sensor. The accuracy of the plot geo-location depended on the site and the global positioning system used. Plots located at LVIS footprints were 10m in radius while those associated with GLAS were either 10m or 15m in radius. While the plots associated with GLAS shots represented less than half of the ground area of the LiDAR measurement, they were selected in part because the field sampling area was representative of the larger area sampled by GLAS. Only those plots with $<10^\circ$ slopes were used in the analysis.

Field workers recorded DBH measurements of individual trees $>3\text{cm}$ in Siberia and $>10\text{cm}$ in Maine within the circular ground plots. The individual tree measurements were converted to AGB using regionally specific allometry linking tree height or tree DBH with AGB (Alexeyev & Birdsey, 1998; Jenkins, Chojnacky, Heath, & Birdsey, 2003); A. Bondarev, unpublished data). From each field inventory, a ground- or an airborne laser scanner-based estimate of AGB for a corresponding LiDAR footprint was calculated where AGB is either a function of DBH, height or both (Neigh, Nelson, Ranson, Margolis, et al., 2013b). In Aurskog, Norway, allometrically derived AGB was calculated for each GLAS footprint based on within-footprint tree heights derived from coincident ALS returns. These ALS measurements had previously been related to ground-inferred AGB from 201 circular field plots using allometric models with DBH and tree height as predictor variables (Næsset et al., 2011). Table 2-2 summarizes information on the plots collected for comparison with either airborne or spaceborne data, and includes their associated study regions and the subset that were $< 100 \text{ Mg}\cdot\text{ha}^{-1}$. Those plots < 100

Mg·ha⁻¹ formed the statistical vegetation structure gradient from conifer-dominant boreal forest to non-forest used to examine the error and error uncertainty of AGB across a TTE-like forest gradient.

Table 2-2. Ground plots for which field-derived AGB was collected. Each plot is located within the footprint of either an airborne (LVIS) or a spaceborne (GLAS) LiDAR sample. This table summarizes the inventory year, regional location and as well as the number of plots used for the empirical models and the subset used for the analysis across the statistical forest structure gradient from 0-100 Mg·ha⁻¹.

<u>LiDAR footprint sensor</u>	<u>Study region</u>	<u>Years of field inventory</u>	<u>Field plot radius (m)</u>	<u># of LiDAR footprints</u>			
				<u>Full AGB range</u>	<u>0 - 100 Mg·ha⁻¹</u>	<u>Full AGB range</u>	<u>0 - 100 Mg·ha⁻¹</u>
GLAS	<i>Aurskog</i>	<i>2006</i>	<i>8-11</i>	306	221	468	351
	<i>Siberia</i>	<i>2007-2010</i>	<i>10-15</i>	162	130		
LVIS	<i>Maine</i>	<i>2009-2011</i>	<i>10</i>	113	60	113	60

2.3.3. LiDAR Waveform Processing

LiDAR waveform returns for forested areas show the vertical distribution of vegetation within the footprint of the return as well as the elevation of the ground surface. Both GLAS and LVIS record vertical canopy information as a continuous waveform representing the heights of canopy elements and the elevation of the ground surface. As tree canopy cover decreases, a greater proportion of the LiDAR return is from vegetation low to the ground, and the ground surface itself. These LiDAR returns from short vegetation can be mixed with the portion of the waveform representing the ground surface. To offset this influence of the ground peak on the portion of the waveform representing vegetation, the LiDAR return waveform was adjusted to more clearly discern sparse and short stature forests from the ground surface. This work was similar to that of performed on airborne waveform data of forests (M. A. Lefsky, Harding, Cohen, Parker, & Shugart, 1999).

With this adjustment, the ground peak portion of the waveform was identified and a Gaussian curve was fit to the portion of the waveform centered on the ground return peak. This was a way to approximate the amount of transmitted energy that was returned to the sensor from the ground surface.

Once centered on the ground peak, the portion of the curve above the ground peak was subtracted from the actual waveform return. The remaining portion represented the signal return from vegetation with less interaction with that of the ground surface. Height metrics were then calculated from these Gaussian-reduced (GR) waveforms. An example showing an original GLAS waveform and the adjusted GLAS waveform are shown in Figure 2-2.

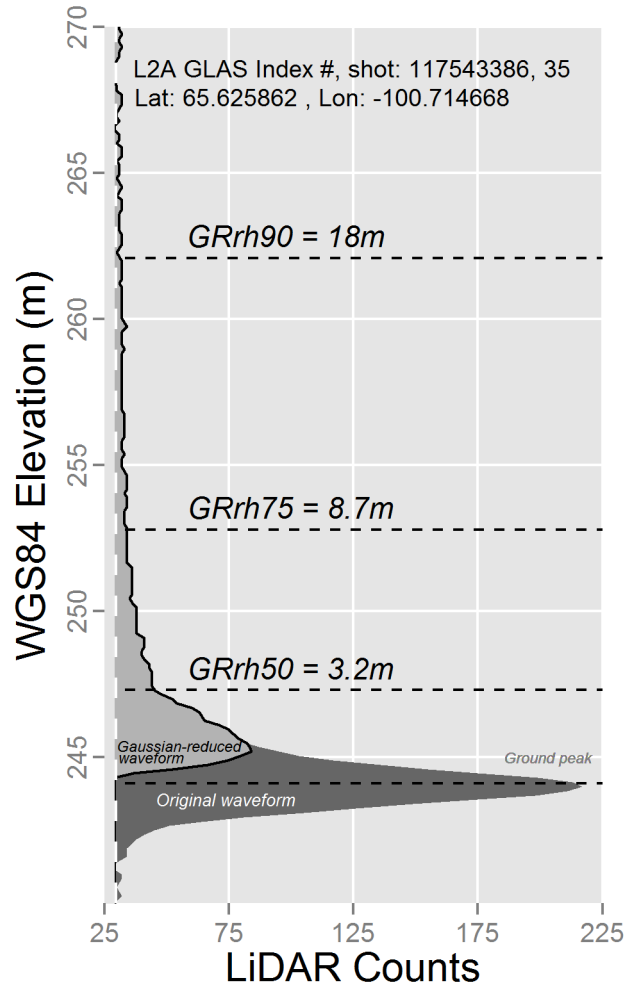


Figure 2-2. Example of an original GLAS waveform and the adjusted “Gaussian-reduced” (GR) waveform that resulted from subtracting the portion of the Gaussian peak above ground elevation from the original GLAS waveform.

2.3.4. Empirical Modeling: Linking Remote Sensing and Ground Reference Measurements

The ground measurements of vegetation structure at LiDAR footprints were linked to LiDAR and SAR data. LiDAR data was already spatially coincident with ground reference data since the ground data was acquired at each LiDAR footprint or via ground-to-ALS relationships with full ALS coverage within the LiDAR footprints. Some of the LiDAR data had undergone a visual screening of each waveform before field measurements were made to ensure ground measurements were collected for LiDAR data representative of vegetation. Some additional screening was necessary to remove GLAS shots whose data, based on visual inspection, showed apparent cloud obscuration or saturation, were on slopes of at least 10 degrees, or whose ground measurements were suspect (ground reference AGB was recorded as 0 but whose percentage of forest within a plot was recorded as > 1). Furthermore, 20 GLAS plots with >50% of AGB derived from hardwood trees were excluded from the analysis to maintain focus on conifer-dominant plots. Second, SAR data was gathered for each LiDAR footprint. SAR pixels whose center points were within LiDAR footprint boundaries were used to derive the mean backscatter for each footprint. For ALOS PALSAR, all pixels whose center points were within 60 m of a GLAS footprint's center point were used to derive mean backscatter for each footprint. This buffer around the GLAS footprint's center location helped account for geo-registration errors between the datasets. More ground plots were available for comparison with spaceborne SAR because than with spaceborne LiDAR because the LiDAR screening process removed potential candidate plots from the regression with LiDAR metrics.

This study used multiple metrics from each sensor. For each LiDAR dataset, three relative height metrics were used. The relative height metric from a LiDAR return depicts the height at which a certain proportion of total received energy (or number of discrete interactions) has been returned to the sensor (Drake et al., 2002). This was done to demonstrate consistency in the way errors from each metric from a given sensor varied in relation to AGB. The remote sensing metrics from each sensor are included in Table 2-1.

Single variable ordinary least squares (OLS) regression was used to model the relationship of sensor metrics to AGB. This was done to demonstrate the fundamental association of a single metric with

vegetation structure. These models were built across the entire range of AGB represented in the ground reference (up to ~400 Mg·ha⁻¹ for plots at GLAS footprints and up to ~340 Mg·ha⁻¹ for plots at LVIS footprints) for the total number of ground plots shown in Table 2-2.

The OLS regressions were applied to log-transformed values of the remote sensing metrics and ground reference AGB. The log-transformed values were back-transformed algebraically, resulting in power function models of the form:

$$AGB = \alpha * metric^\beta, \text{ where } \alpha \text{ and } \beta \text{ are coefficients of the regression. (1)}$$

Models of this form are commonly used to infer biomass from tree structural characteristics (Ter-Mikaelian & Korzukhin, 1997). With these models, the remote sensing data served as the independent variables to model forest AGB. Using ground reference AGB, field plots were grouped into several AGB intervals (bins) representing a statistical gradient of vegetation structure across which remote sensing measurements were evaluated.

2.3.5. Uncertainty Analysis

An uncertainty analysis was performed to evaluate the error and the uncertainty of the error of predicted AGB within AGB intervals across a statistical gradient of AGB from 0 – 100 Mg·ha⁻¹. For each sensor metric, we applied its empirical model relating it to AGB, and then compared the model's predicted (from the remote sensing metric) AGB value to the ground reference (observed) value. Each plot's remote sensing model prediction error was calculated as the difference between the predicted and observed AGB value. Due to the fact that there were many more plots established on satellite footprints, the values were grouped into bins of 10 Mg·ha⁻¹ for spaceborne data and 20 Mg·ha⁻¹ for airborne data, forming a unique sample set for each AGB bin and providing the basis for a per bin analysis.

For each AGB bin, the bin's error was calculated as the RMSE of the set of plots (datapoints) within each bin. The uncertainty of the error value per bin was reported as a 95% confidence interval (CI). This CI characterizes a PDF about the mean error value.

The CI was calculated using two different methods. The first method used a bootstrapping sampling approach to gather n-1 observations for each of 1000 samples, from which 1000 estimates of the RMSE were computed. These 1000 bootstrapped RMSE estimates formed a PDF representing the mean and variance of the RMSE for each AGB bin. The second method used the chi-square probability distribution with df = n-1 to characterize the 95% CI. The CI is calculated as follows (Ott & Longnecker, 2010):

$$CI_{upper} = \sqrt{\frac{(n-1) * RMSE^2}{\chi_{upper}^2}} \quad (2a)$$

$$CI_{lower} = \sqrt{\frac{(n-1) * RMSE^2}{\chi_{lower}^2}} \quad (2b)$$

These methods produce an inference about a population variance, where the variability of the RMSE within a population of many RMSEs for a given AGB bin is expressed with a CI.

2.4. Results

2.4.1. Empirical Models of AGB vs. Metrics

As illustrated in Figure 2-3, the airborne LiDAR and SAR models explained a much greater proportion of AGB variability relative to the spaceborne models. LVIS, GLiHT and UAVSAR models explained 60-89% of AGB variation while GLAS and PALSAR explained 13-46%. The models derived from airborne data performed better than those from spaceborne data, effectively creating an upper bound for model performance and AGB bin errors that can be expected from spaceborne data. For airborne LiDAR regression R^2 ranged from 0.74-0.89, for airborne SAR 0.6-0.8, for spaceborne LiDAR 0.26-0.46, and for spaceborne SAR 0.13 and 0.32. This is consistent with a number of studies examined in a recent meta-analysis of that examined the use of LiDAR for estimating forest biomass (Zolkos, Goetz, & Dubayah, 2010). In particular, the airborne models were built on relationships that show significant heteroscedasticity across the range of ground reference AGB, where low AGB regions show lower scatter about the model line than do high AGB regions.

The spaceborne models were built on relationships showing significant scatter across the entire range of AGB. In particular, the spaceborne SAR models explain a relatively low proportion of overall variance (0.16 and 0.32 for HH and HV, respectively), and poorly fit the data. The broad range of backscatter associated with very low AGB values is a prominent component of the overall scatter for both spaceborne SAR polarizations.

Models from adjusted waveform metrics generally explained more of the variation between height metrics and ground reference than did those from the un-adjusted metrics. This was more evident in the spaceborne GLAS data than in the airborne LVIS data, and more evident in the height metric most representative of the middle of the canopy (rh50) than that of the upper canopy (rh90).

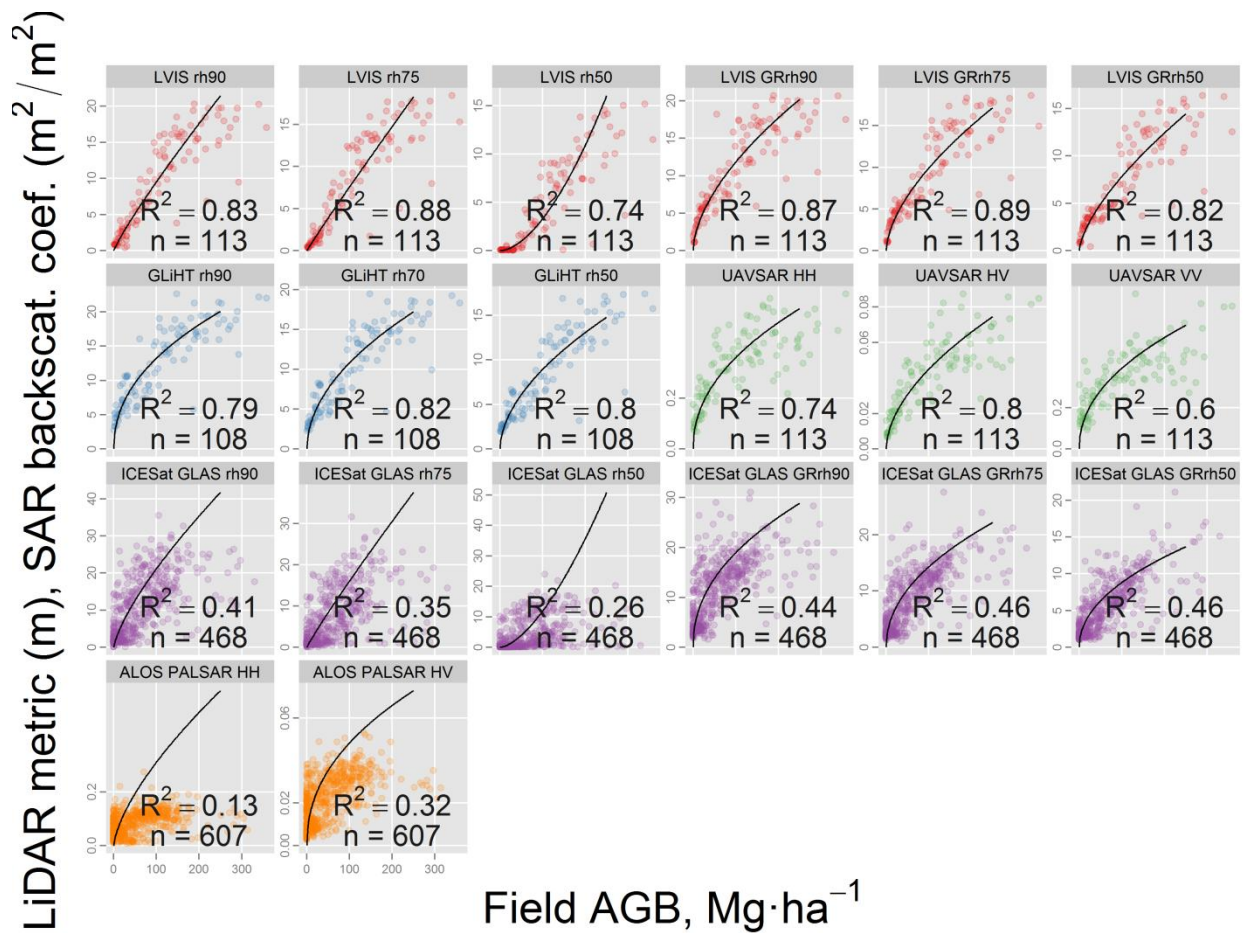


Figure 2-3. Plot matrix showing the empirical models used to predict AGB from airborne and spaceborne remote sensing metrics.

2.4.2. Error and Error Uncertainty within AGB Bins

The error (RMSE) and error uncertainty (95% confidence interval of the RMSE) of AGB predictions from airborne LiDAR and SAR and spaceborne LiDAR metrics are reported by bin as part of the plot matrix in Figure 2-4 for the set of metrics reported above. In this portion of the analysis, results are not reported for spaceborne SAR. The errors calculated would be derived from poorly fit models and are fundamentally misleading because the empirical models for each polarization fail to explain an overwhelming majority of the variation.

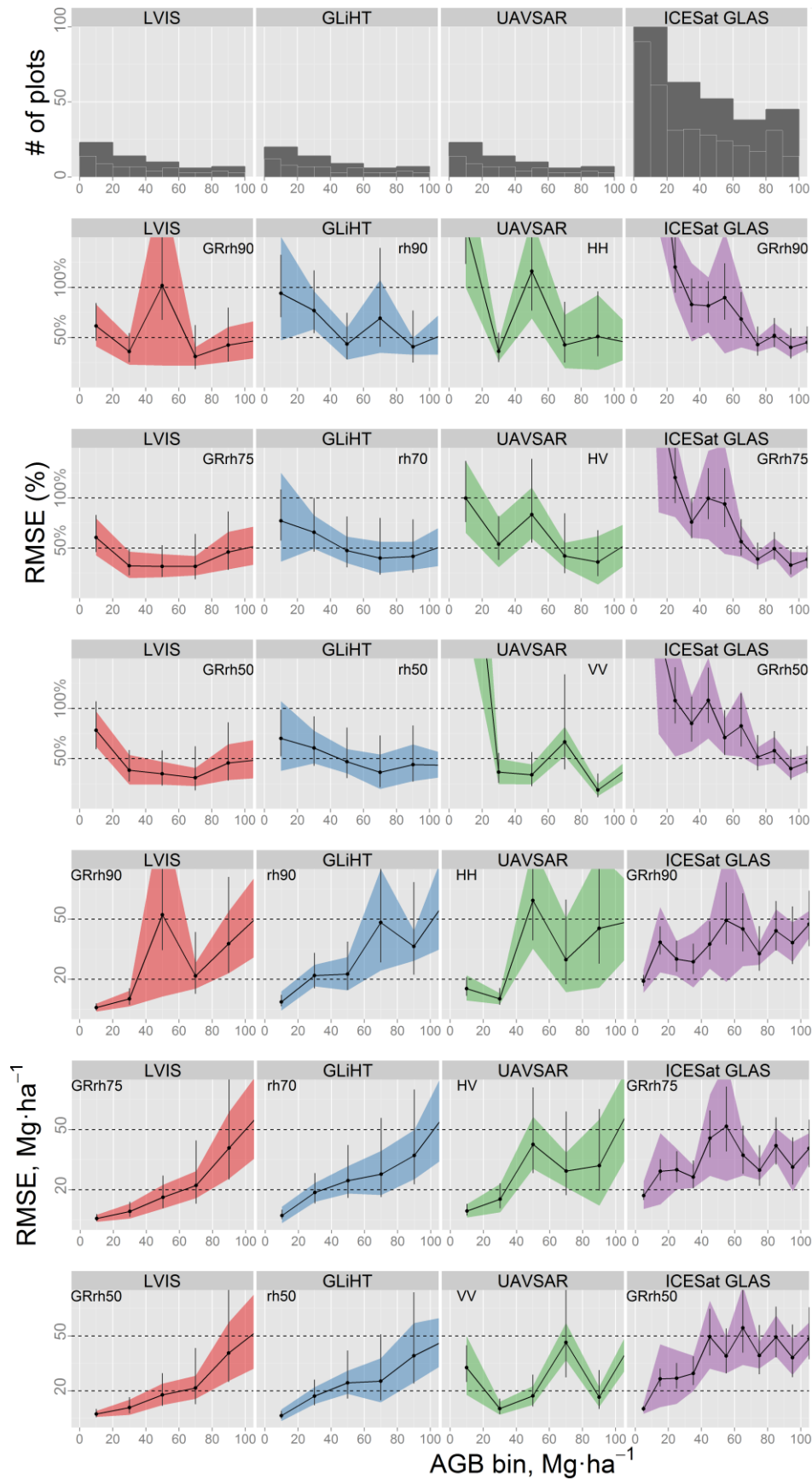


Figure 2-4. Each sensor's results are reported by column. The first row shows the histograms of ground reference plots used in comparison with each sensor's metrics across a 0-100 Mg·ha⁻¹ structure gradient. The gray bars of the histograms span 20 Mg·ha⁻¹ bins used to report airborne results, and are overlaid with white-outlined bars used to report spaceborne results. Rows 2-4 show error plots in relative terms (RMSE %). Rows 5-7 show error plots in absolute terms (RMSE). Each column's plot is set up so that each AGB bin aligns vertically with the plot below.

The larger number of ground reference plots associated with the spaceborne datasets permitted consideration of smaller bin sizes relative to those used for the airborne datasets. Each error value is an estimate of the true mean error value associated with each bin's AGB prediction. The measure of error, the relative RMSE (RMSE %), is also shown in absolute terms (RMSE) in the bottom portion of Figure 2-4. The datapoints in the plot matrices are shown with black dots, connected by the black lines, for each AGB bin. These errors are based on the empirical models derived from each the relationship of ground-reference AGB with each sensor metric. AGB prediction models based on adjusted waveform metrics (for LVIS and GLAS metrics) explained a greater proportion of overall variation and were used to evaluate error and error uncertainty trends in place of their unadjusted counterparts. The relative errors were calculated by dividing the RMSE by the mean AGB value of the datapoints in the corresponding AGB bin while the absolute errors involved the standard RMSE calculation per bin. For both sets of plots, data values align on the x-axis with the midpoint value for each bin.

The errors of airborne LiDAR and SAR and spaceborne LiDAR metrics show a general trend of reduced relative errors as AGB magnitudes increase, particularly from 0 – 60 Mg·ha⁻¹. Interruptions in this general trend occurred for airborne data (LVIS rh90, GLiHT rh90, UAVSAR HH, HV, VV) in bins for which there were fewer than 10 datapoints. The plots for the airborne data (first 3 columns) report results in 20 Mg·ha⁻¹ bins. The number of ground reference observations for each airborne bin ranged from 6 – 23. In airborne LiDAR (LVIS and GLiHT) bin 0-20 Mg·ha⁻¹, all the error datapoints are above 50% (for all 3 metrics of both sensors). In bin 20-40 Mg·ha⁻¹ half of the error datapoints are below 50% (the GLiHT are all above this mark). Bin 40-60 Mg·ha⁻¹ shows all but one error datapoint to be below 50%. The exception occurs where there is a spike in the trend of the adjusted rh90 metric for LVIS. Bins 60-80 and 80-100 Mg·ha⁻¹ show all but one error datapoint below 50%, the exception being a spike along

the GLiHT rh90 trend. In airborne SAR (UAVSAR) bin 0-20 Mg·ha⁻¹ each polarization had errors greater than or approximately equal to 100%. Bins 20-40 through 80-100 show errors varying from <50% to > 100%. The polarization with the best relationship with ground reference AGB (HV, R² = 0.8), reveals a clear trend whereby relative errors decrease from ~100% for Bin 0-20 down to <50% for bins 60-80 and 80-100 and is similar to that of the VV polarization but for which the empirical model of AGB explains less variance (R² = 0.6). Spikes in these error trends occur within bins where there are fewer than 10 datapoints.

The error trends for the spaceborne LiDAR were derived from 10 Mg·ha⁻¹ bins. Across the intervals of the AGB gradient, 8 of the 10 bins had greater than 20 datapoints and thus show somewhat smoother error trends across the gradient. For this error trend, bins 0-10 through 30-40 Mg·ha⁻¹ show errors above and near 100% while bins 40-50 through 60-70 Mg·ha⁻¹ show errors between 50-100%. Only above 70 Mg·ha⁻¹ do errors begin to approach 50% of ground reference AGB.

The error plots in Figure 2-4 also show two estimates of the error uncertainty (95% confidence interval of the RMSE) for each AGB bin. The first error uncertainty estimate, depicted with the colored ribbons around the horizontal black lines, is the result of the bootstrapping method used to derive a 95% confidence interval around each bin AGB RMSE value. The second error uncertainty estimate, depicted with the vertical black bars position through each datapoint, shows the result of a method using the chi-squared distribution to calculate a 95% confidence interval. These uncertainty calculations for each bin form error bounds around the mean values of AGB error across a forest AGB gradient of 0-100 Mg·ha⁻¹.

The pairs of error uncertainty estimates (the ribbons and vertical bars in Figure 2-4) bounding the error estimates are generally consistent for all metrics of all datasets. Airborne error uncertainty estimates differ notably for a few spikes along the error curves, particularly for LVIS rh90 bin 40-60 and UAVSAR HV bin 40-60 and VV bin 60-80. Aside from these spikes, where error uncertainty broadens conspicuously, error bounds general range from ~25%-50% of a given AGB bin's mean value. The uncertainty bounds for the error trends of the spaceborne LiDAR metrics are consistently broad across the majority of the 0-100 Mg·ha⁻¹ range. Below 30 Mg·ha⁻¹ the uncertainty bounds never fall

below 50% and extend to well above 100%. From 30-80 Mg·ha⁻¹ the uncertainty bounds occupy most of the range from 50-100% error. These estimates of spaceborne LiDAR error uncertainty describe the difficulty of characterizing differences in AGB with current spaceborne sensors below 80 Mg·ha⁻¹ with less than 50-100% error.

2.5. Discussion

The goal of this study was to evaluate the uncertainty of biomass inferred from LiDAR and SAR across a forest structure gradient. This study reports both the relative error and the absolute error of AGB, and their uncertainties, across a boreal forest to non-forest structure gradient from 0-100 Mg·ha⁻¹ which is characteristic of sparse forests in the TTE of northern Siberia (Kajimoto et al., 2009). The analysis of both airborne and spaceborne measurements help evaluate the relative lack of sensitivity of these AGB measurements from spaceborne measurement compared to those from airborne sensors designed primarily to measure fine details (plot scale) vegetation structure. Remote sensing provides a means to assess terrestrial details across a variety of scales, however the results of this study suggest a limited ability to discern potentially important vegetation structure differences in sparsely forested regions with short stature vegetation. This insensitivity has been noted across a latitudinal gradient in Quebec (R. Nelson, 2010). There are important implications of this lack of sensitivity for understanding change in vegetation structure, particularly at biome boundaries. However, the methodology has limitations associated with characterizing AGB error that warrant discussion.

2.5.1. Limited Ability to Discern Sparse Forests at Plot Scale

Spaceborne data could provide the best means to synoptically measure vegetation across broad scales. However, the results suggest that currently a single type of measurement, independently, may not reliably capture plot level differences in AGB. In this study the scale of the plot level is equivalent to the site-level scale discussed elsewhere in the literature (Hofgaard et al., 2012; Hofgaard & Harper, 2011; F.-K. Holtmeier & Broll, 2005). At the site-level scale, characteristics of groups of trees can be described and help to explain the biogeographic drivers and dynamics of vegetation structure (Bonan et al., 1995;

Hofgaard et al., 2012; F. K. Holtmeier, 2009; F.-K. Holtmeier & Broll, 2005; Risser, 1995). According to the results reported above, spaceborne LiDAR measurements of a forest patch of $\sim 60 \text{ Mg}\cdot\text{ha}^{-1}$ are likely indistinguishable from those measurements of a forest patch of $\sim 20 \text{ Mg}\cdot\text{ha}^{-1}$. This is because the uncertainty of the measurements' AGB error for each patch overlaps statistically with the other. For spaceborne SAR, the empirical models were so weak that an assessment of AGB bin error was unrealistic. It is likely that inferred AGB derived from circular plots 10 - $\sim 30\text{m}$ in radius are insufficient for establishing relationships with backscatter from ALOS PALSAR. Larger plots, oriented perpendicular to the sensor's view angle may produce better relationships with SAR backscatter. However, such a requirement for SAR-specific field plot design precludes the use of the wealth of ground data available. Significant scatter is also evident in the relationship of spaceborne LiDAR with field-derived AGB, which may be due partially to plots size, and may increase the final uncertainty of predicted AGB. However, the issue of plot size was likely not as problematic as it was with SAR data, because the technique of sampling a small portion of the overall LiDAR footprint was facilitated by the selection of plots that were representative of the larger GLAS footprint. The extent to which plot size affected regression scatter was not explored.

2.5.2. Implications for Understanding TTE Vegetation Structure Change

Subtle changes in vegetation structure in and around the TTE, across broad scales, can have varying local and regional effects (Loranty & Goetz, 2012; Pearson et al., 2013; Sveinbjörnsson et al., 2002). Changes in vegetation structure, such as AGB, along the northern edge of the boreal forest can alter the way the land surface amplifies or dampens ongoing changes to climate (Bonan et al., 1995; Callaghan, Werkman, & Crawford, 2002b). With the lack of sensitivity of spaceborne LiDAR and SAR to subtle changes in biomass reported above, it is difficult to obtain a synoptic perspective of such changes, with these instruments alone, across a biome boundary such as the TTE that has begun showing spatially variable changes in vegetation structure (Bonan et al., 1992; Elmendorf et al., 2012; M. Harsch et al., 2009; Hofgaard & Harper, 2011). However, the extent to which this measurement error limits the

ability to provide a synoptic perspective for discerning differences in ecologically significant vegetation patterns, or forms, along a biome boundary in flux such as the TTE remains in question.

To better understand spatial difference in TTE vegetation structure, the error and error uncertainty of vegetation structure measurements, specifically AGB, across low biomass boreal forest gradients need to be reduced significantly. If this is accomplished by increasing plot size and averaging an increasing number of remote sensing measurements, then the ability to discern site level characteristics from space is not likely. Sensors designed primarily to measure vegetation structure at the plot scale would likely reduce the uncertainty of AGB measurements in general, and may improve our understanding of subtle changes in vegetation in the high northern latitudes whose cumulative effect on ecosystem dynamics may have resounding broad scale effects.

2.5.3. Limitations of AGB Uncertainty Estimates

These error and uncertainty figures need to be put into context in terms of their limitations and their use for evaluating the efficacy of spaceborne measurements of subtle differences in vegetation structure in a region where such differences can have varying and dramatic local and regional effects on climate. These limitations arise from the use of RMSE as a measure of overall error and error uncertainty, the empirical models relating ground reference to sensor data, and the statistical approaches for assessing error uncertainty.

It is necessary to acknowledge that the RMSE does not completely characterize the error of empirically modeled AGB because it doesn't account for plot size, positional accuracy, and allometric error (Zolkos et al., 2010). First, the size of the plots used to gather ground reference data can have significant influence on reference AGB values, whereby larger ground plots will decrease both the relative error of remote sensing predictions of AGB as well as the effect of co-registration errors between the plot and the remote sensing data (Frazer et al., 2011; Mascaro et al., 2011). The plots used in this study were co-incident with LiDAR shots, however the plots used to sample the spaceborne GLAS LiDAR represented only a subset (10-15m radius from the GPS-located footprint center) of the entire

GLAS footprint (~32m radius). In Aurskog, Norway, the field measurements were not coincident with GLAS measurements, but instead we related to ALS data, which was also acquired over GLAS footprints. For these sites, there were two models involved, one relating ground measurements to ALS, and another relating ALS to GLAS. Furthermore, the size of the plots affected the extraction of coincident spaceborne SAR data. Pixels providing the SAR measurement for a plot were extracted within a 60m buffer of the footprint centroid to acquire sufficient pixels to compute a mean SAR metric value in and around the location of the plot.

This leads into a second limitation of the RMSE metric, which is its inability to account for poor geo-location. Errors can arise when pixels are poorly geo-referenced and do not represent, for example, the SAR backscatter from within the plot. A study examining SAR data exclusively would use plots that are more easily linked to the SAR backscatter measurements (Ahmed et al., 2013). The poor empirical models of both the spaceborne SAR metrics lend credence to the problematic relationship of plot AGB measurements and SAR backscatter, and decrease the reliability of the AGB error assessments made for ALOS PALSAR.

There are three issues with the empirical models relating to the uncertainty estimates that warrant mention. The first pertains to the single variable models used for each sensor. These models were used as a way of examining a fundamental relationship between remote sensing metrics and ground reference. This study intentionally avoided evaluations and comparisons of a variety of empirical models for a given sensor. If this were the case, a multiple variable regression tree approach such as that from the Random Forest method would likely have produced better models, particularly if data from multiple sensors were combined (Hyde et al., 2006; Kellndorfer et al., 2010; Montesano et al., 2013; G. Sun et al., 2011). Rather, single variable models were used to simplify the analysis, which comes at the expense of model optimization, but allows for error to be directed attributed to a specific metric and allows these errors to be compared between metrics. As such, the uncertainty we report may represent the upper bound of AGB error and error uncertainty across the gradient, which may be reduced with other prediction methods and additional variables. Second, empirical models built from lognormal relationships require a correction

factor to account for the error associated with the back-transformation of the regression coefficients. A correction should be applied to the model-predicted AGB that has been back-transformed from natural log units (Baskerville, 1972; Flewelling & Pienaar, 1981). However, this correction resulted in model RMSEs much larger than those derived from the uncorrected model-predicted AGB, essentially more severely and unrealistically penalizing the spaceborne models with the larger RMSEs. Therefore, back-transformation corrections were not applied. Third, the form of the empirical model relating AGB to remote sensing metrics may not be the most appropriate for these data. This may be particularly true for the spaceborne SAR models.

Finally, uncertainty of the RMSE within certain AGB intervals was assessed based on a very low number of samples within each bin. This was a problem particularly for the airborne data, and was mitigated slightly by using AGB bins of $20 \text{ Mg}\cdot\text{ha}^{-1}$ as opposed to bins half that size. Nevertheless, samples still remained small ($n < 15$). In these cases the RMSE, which has a biased influence on those datapoints further from the regression line, can become large because outliers within a small sample will tend to have undue influence on estimates of overall error. This inflates error estimates and was likely responsible for both the spikes in error estimates and the broad uncertainty estimates about the error trends for airborne metrics. Furthermore, bootstrapping doesn't provide a reliable estimate of uncertainty with very small sample sizes.

2.6. Conclusions

We examined the uncertainty of LiDAR and SAR measurements across a gradient in conifer-dominant boreal-like forest structure based on empirical models of LiDAR and SAR metrics with inferred AGB from ground measurements. The empirical models from airborne data showed strong relationships, explaining 60-89% of overall variation. Models for spaceborne LiDAR were weaker because of significant scatter across the modeled range while models for spaceborne SAR explained less than 33% of overall variation. The error and error uncertainty measurements of AGB across a statistical AGB gradient from $0\text{-}100 \text{ Mg}\cdot\text{ha}^{-1}$ show that the uncertainty of both airborne and spaceborne data changes across a

boreal-like forest gradient. The errors of airborne and spaceborne LiDAR and airborne SAR metrics show a general trend of reduced relative errors as AGB magnitudes increase, particularly from 0 – 60 Mg·ha⁻¹. Empirical models relating spaceborne metrics to AGB and estimates of spaceborne LiDAR error uncertainty reinforce the difficulty of characterizing differences in AGB with current spaceborne sensors, particularly below 80 Mg·ha⁻¹ with less than 50-100% error.

Chapter 3: The Uncertainty of Biomass Estimates from Modeled ICESat-2 Returns Across a Boreal Forest Gradient

3.1. Abstract

The Forest Light (FLIGHT) radiative transfer model was used to examine the uncertainty of vegetation structure measurements from NASA's planned ICESat-2 photon counting light detection and ranging (LiDAR) instrument across a synthetic Larix forest gradient in the taiga-tundra ecotone. The simulations demonstrate how measurements from the planned spaceborne mission, which differ from those of previous LiDAR systems, may perform across a boreal forest to non-forest structure gradient in globally important ecological region of northern Siberia. We used a modified version of FLIGHT to simulate the acquisition parameters of ICESat-2. Modeled returns were analyzed from collections of sequential footprints along LiDAR tracks (link-scales) of lengths ranging from 20m – 90m. These link-scales traversed synthetic forest stands that were initialized with parameters drawn from field surveys in Siberian Larix forests. LiDAR returns from vegetation were compiled for 100 simulated LiDAR collections for each 10 Mg·ha⁻¹ interval in the 0 - 100 Mg·ha⁻¹ above-ground biomass density (AGB) forest gradient. Canopy height metrics were computed and AGB was inferred from empirical models. The root mean square error (RMSE) and RMSE uncertainty associated with the distribution of inferred AGB within each AGB interval across the gradient was examined.

Simulation results of the bright daylight and low vegetation reflectivity conditions for collecting photon counting LiDAR with no topographic relief show that 1-2 photons are returned for 79% - 88% of LiDAR shots. Signal photons account for ~67% of all LiDAR returns, while ~50% of shots result in 1 signal photon returned. The proportion of these signal photon returns do not differ significantly ($p > 0.05$) for AGB intervals $> 20 \text{ Mg}\cdot\text{ha}^{-1}$. The 50m link-scale approximates the finest horizontal resolution (length) at which photon counting LiDAR collection provides strong model fits and minimizes forest

structure uncertainty in the synthetic *Larix* stands. At this link-scale AGB > 20 Mg·ha⁻¹ has AGB error from 20 - 50% at the 95% confidence level. These results suggest that the theoretical sensitivity of ICESat-2 photon counting LiDAR measurements alone lack the ability to consistently discern differences in inferred AGB at 10 Mg·ha⁻¹ intervals in sparse forests characteristic of the taiga-tundra ecotone.

3.2. Introduction

3.2.1. Global Relevance of the Taiga-Tundra Ecotone

At the northern edge of the boreal forest in the taiga-tundra ecotone (TTE), vegetation cover and structure is changing (Elmendorf et al., 2012; Epstein, Myers-Smith, & Walker, 2013; V. Kharuk et al., 2013b; Myers-Smith et al., 2011; Ropars & Boudreau, 2012). These changes can be subtle yet occur across broad scales, and can alter the magnitude and direction of biome-level and continental scale feedbacks to climate (Bonan, 2008; Bonfils et al., 2012; Chapin, 2000; 2005; Lawrence & Swenson, 2011; Loranty et al., 2011; Loranty & Goetz, 2012; Loranty, Berner, Goetz, Jin, & Randerson, 2013; Myers-Smith et al., 2011; Pearson et al., 2013; Swann et al., 2010).

Broad-scale, but spatially discontinuous and heterogeneous, changes in forest structure are expected in northern Siberia, where the TTE reaches its northern-most limit extending above 72°N (Bondarev, 1997). At specific sites in the TTE canopy closure and expansion of *Larix* in tundra have been observed (V. I. Kharuk et al., 2006). Evidence shows that dark-needle conifers have begun moving into *Larix* forests and woodlands (V. I. Kharuk et al., 2005). Observed at broad-scales, the patterns formed by the smaller plot-scale changes (Devi et al., 2008; Elmendorf et al., 2012; Forbes et al., 2010; M. Harsch et al., 2009; Mazepa & Devi, 2007; Myers-Smith et al., 2011) demonstrate their overall magnitude, uniformity, spatial characteristics and links with other landscape characteristics across a biome. Such characteristics include the extent of continuous permafrost, which across northern Siberia influences the distribution of vegetation (Lloyd et al., 2011; Schulze et al., 2012; Sugimoto et al., 2002; Tchebakova et al., 2009; N. Zhang et al., 2011). The strength and timing of a climate feedback from permafrost-bound carbon is a function of vegetation structure (Epstein et al., 2004; Jorgenson et al., 2010;

Lawrence & Swenson, 2011; Schaefer et al., 2011). Model projections of this feedback to climate, accounting for vegetation characteristics, suggest a central role for high northern latitude vegetation structure in determining the magnitude of changes to the global carbon cycle (Schaefer et al., 2011).

These subtle changes in vegetation structure and patterns in the high northern latitudes across broad scales and acute climate changes in northern Siberia highlight the need for both synoptic and spatially detailed remote monitoring of vegetation. Furthermore, the possibility that subtle changes in vegetation structure may significantly alter climate feedbacks warrants improved characterization of how uncertainty in vegetation measurements varies with extent and structure, particularly in the sparse *Larix* forest gradients of the TTE where non-uniform vegetation changes may be converging.

3.2.2. Forest Structure in Northern Siberia

Forest stands within the TTE of northern Siberia have an over-story that is often exclusively *Larix*, are sparse and short in stature, and form the northern limit of forest vegetation (Abaimov, 2009). Stand structure in this region is heavily influenced by the presence of permafrost. *Larix* stands sampled along the Kotuykan River in 2008 at flat or gently sloping north and south facing slopes show that >90% of trees are < 10m in height ((V. Kharuk et al., 2013b); unpublished data). Mean tree heights of *Larix gmelinii* generally do not exceed ~12m for stands underlain with continuous permafrost and varying active layer depths (Osawa & Kajimoto, 2009; Usoltsev, Koltunova, Kajimoto, Osawa, & KOIKE, 2002). For these stands, the maximum above-ground biomass density (AGB) is approximately 100 Mg·ha⁻¹. This depends on stand age, tree density and local site conditions, and AGB potential generally decreases from south to north, following a latitudinal gradient (Osawa & Kajimoto, 2009).

3.2.3. LiDAR Remote Sensing of Vegetation

Light detection and ranging (LiDAR) has become widely used for measuring and monitoring vegetation characteristics because of its potential sensitivity to subtle vegetation structural differences (Wasser, Day, Chasmer, & Taylor, 2013a; Whitehurst, Swatantran, Blair, Hofton, & Dubayah, 2013)),

and its availability on platforms that have sampled across a range of scales (R. Nelson et al., 2009; Næsset & Nelson, 2007). LiDAR sensors are often deployed as airborne systems (LVIS; (Blair et al., 1999), G-LiHT; (Cook et al., 2013)) but have also collected data globally from space (ICESat-GLAS; (Abshire et al., 2005)). Satellite-based LiDAR collections offer consistent, synoptic sample measurements of surface characteristics across broad scales. While the only free-flying satellite-based LiDAR instrument, to date, was designed primarily to measure ice, ICESat-GLAS has been used in concert with passive optical satellite data to provide regional-global scale estimates of timber volume, vegetation carbon density, above-ground biomass density, and vegetation height (Baccini, Laporte, & Goetz, 2008; M. A. Lefsky, 2010; Los et al., 2012; Neigh, Nelson, Ranson, Margolis, et al., 2013b; R. Nelson et al., 2009; Simard, Pinto, & Fisher, 2011). These measurements have been made despite GLAS footprints being ~50-60m in diameter, spaced ~170m along track (extending to 86° north and south), and covering only a small fraction of the vegetated land surface. The accuracy of vegetation height measurements from ICESat-GLAS vary depending on a number of factors including vegetation type, slope and measurement scale, and can range from ~3m – 12m .

LiDAR sensors vary in how they measure vegetation. Waveform (i.e., pulse-limited) LiDAR sensors digitize the vertical distribution of vegetation structure within a footprint by recording the total energy returned from a single transmitted pulse for fixed vertical bins. Discrete return LiDAR provides ~3-5 returns for each LiDAR pulse based upon the intensity of returned energy (Evans, Hudak, Faux, & Smith, 2009). Recently, micropulse (photon counting) LiDAR technology has emerged as a means for remote sensing of vegetation structure. For vegetation, this technology yields point clouds that represent vegetation height measurements that are derived from individual photon returns collected from many low-energy LiDAR pulses in rapid succession (Herzfeld et al., 2012). These photon returns can be spatially aggregated to create histograms of the vertical distribution of returns for a given area, similar to data provided by a LiDAR waveform. Each sensor's ability to measure and map vegetation structure depends on multiple factors including sensor design, data collection schemes (timing and spatial characteristics of the measurement), and vegetation characteristics (type, density, health).

The spaceborne LiDAR on the ICESat-2 satellite, scheduled to launch no earlier than 2017, will feature a multiple-beam (a combination of stronger and weaker beams) photon counting LiDAR instrument (ATLAS). The initial data collection scheme for a given beam on the ATLAS sensor noted that photons will be collected for a 10m diameter footprint at 70cm along-track spacing (Abdalati et al., 2010), however updated schemes have increased the footprint size. The exact position of each photon from within the footprint will not be known. For sparse forest stands in the TTE, a single footprint's measurement will be insufficient for characterizing vertical vegetation structure within that footprint and for inferring vertical vegetation characteristics outside the footprint, particularly as vegetation heterogeneity increases. LiDAR collection schemes for characterizing various types of forest stands (e.g., the way in which photon returns are aggregated spatially) may help improve vegetation structure measurements as well as improve understanding of how these measurements change with vegetation characteristics.

Given the sparse density of trees in TTE forests, the photon returns within a single footprint are unlikely to come from a tree, particularly the highest portion of the canopy. This issue of under-sampling the top portion of forest canopies is common for LiDAR measurement of forest structure (Kaartinen et al., 2012; R. Nelson, Krabill, & Tonelli, 1988; Næsset, 2011). Collections of sequential footprints along a LiDAR track (i.e, a link-scale) will provide the best opportunity for measuring forest vegetation canopy and forest understory heights, inferring AGB, and assessing how these characteristics vary spatially across a heterogeneous landscape such as the TTE. Understanding these characteristics can help assess the spatial details and regional differences in tree recruitment in the TTE, which can have affects on climate and biodiversity (Bonan, 2008; Hofgaard et al., 2012) that vary according to scale (Bonfils et al., 2012; Lawrence & Swenson, 2011).

LiDAR has been shown to vary in the uncertainty of its measurements across forest gradients (Montesano, Nelson, Dubayah, Sun, Cook, et al., 2014a). These varying factors may lead to differing measurement errors among LiDAR sensors and across vegetation structure gradients. It is important to quantify the measurement errors (uncertainty) of current sensors, as well to provide advance

notice of potential errors from those sensors planned for the near-term, in order to evaluate the limits in the ability to synoptically characterize biophysically relevant changes in vegetation in the near future.

3.2.4. The FLIGHT Model

Radiative transfer models are used in terrestrial remote sensing as tools for examining the physical interaction of electromagnetic radiation with earth surface features. Such models have been used to demonstrate how LiDAR signals vary with the vertical structure of vegetation (Koetz et al., 2006; Ni-Meister, Jupp, & Dubayah, 2001; G. Sun & Ranson, 2000). In the context of this study, these models help explore the theoretical sensitivity of photon counting LiDAR from the planned ICESat-2 ATLAS instrument to sparse forests in the TTE.

The Forest Light radiative transfer model (FLIGHT) uses Monte Carlo simulation of light transport for the optical domain (North, 1996) to model the interaction of LiDAR with forested surfaces. Evaluation of solar bidirectional reflectance and LiDAR backscatter retro-reflectance is achieved by simulation of the photon path within a canopy representation, and simulation of the chain of scattering events incurred by a photon in its path from the source to the receiver or to its absorption, including multiple scattering between canopy elements and the ground surface.

The model describes tree crowns as conical or elliptical shells using specified dimensions. The model takes as input the proportional composition of foliage, branch and shoot/senescent material within crowns, leaf angle distribution, and leaf area. The spectral reflectance and transmittance properties of the canopy components and background surface are also specified. Forest surfaces are generated statistically using mean conditions related to tree cover, tree type, position and size, or can be initialized with a tree stem map detailing these attributes for each tree. The effect of slope is incorporated into the model using a planar surface with defined slope angle.

This model has been adapted to simulate satellite waveform LiDAR collections (North, Rosette, Suárez, & Los, 2010) and has been used to examine the uncertainty of these data for vegetation structure and topography (Rosette, North, Suarez, & Los, 2010). It has also been used to examine the sensitivity of

LiDAR to site-specific conditions such as topography, canopy and ground reflectance (Rosette et al., 2013). For LiDAR simulation, the model calculates the probability distribution of return of a photon emitted from the laser as a function of time, and has been validated by comparing model simulations with field and satellite observations (Morton et al., 2014; North et al., 2010) and through comparisons with other radiative transfer models (Widlowski et al., 2007). For the simulation of individual photon returns for photon counting LiDAR, the expected energy distribution is quantized, and stochastic Poisson sampling is used to calculate the expected number of returned photons at each time interval. Solar ‘noise’ due to photons originating from solar scattering from land and atmosphere is calculated, and included implicitly within the simulation by increasing energy within each bin. The LiDAR sensor is characterized using wavelength(s), pulse duration, emitted energy per pulse, instantaneous field of view, and sensor ‘dead’ time. Footprint dimensions are determined using sensor altitude, beam divergence and viewing geometry. Atmospheric effects of signal delay or pulse broadening are not represented, however atmospheric transmittance is accounted for, giving attenuation of the signal by fixed gases and aerosols using coefficients derived from the 6S radiative transfer model (Vermote, Tanré, Deuze, Herman, & Morcette, 1997).

The goal of this study was to examine the error and error uncertainty of AGB derived from modeled ICESat-2 forest height returns from synthetic *Larix* stands in the TTE across multiple link-scales. For this work, a recent version of the FLIGHT model has been adapted to stochastically simulate photon counting LiDAR ranging measurements representative of those that will be acquired by the ATLAS instrument on the ICESat-2 satellite. FLIGHT is used to evaluate the number of simulated height measurements from photon counting LiDAR shots that are available for sparse boreal-like forests, the uncertainty of derived AGB from simulated ICESat-2 data across a low biomass boreal forest gradient, and the difference in the AGB uncertainty between AGB intervals across this gradient. Finally, this study examines the link-scales at which AGB uncertainty is minimized for sparse forests in the TTE.

3.3. Methods

3.3.1. Overview

The first portion of this work involved using the radiative transfer model to simulate photon counting LiDAR returns for *Larix* stands, and to derive stand heights across various link-scales. To simulate ICESat-2 LiDAR returns for northern Siberia *Larix* forest stands within AGB intervals across a forest to non-forest gradient, FLIGHT was initialized with forest parameters and ICESat-2 ATLAS instrument parameters (as of November 2012). The first part of the study, in which these returns were simulated, involved three central steps. The first step focused on preparing the model to run with ATLAS parameters and for stochastic simulation of photon transport. The second step involved providing FLIGHT with average *Larix* stand parameters. The third step required deriving an algorithm to determine canopy height.

The second part of the study required empirical modeling and an uncertainty analysis. The means from the simulated return heights were calculated for each AGB interval and an empirical model was fit relating each interval's mean return heights to its corresponding mean AGB value. Finally, simulated heights were converted to AGB and the error (RMSE) and error uncertainty (RMSE 95% confidence interval) of this derived AGB, across all link-scales, was computed.

3.3.2. ICESat-2 ATLAS Parameters for FLIGHT

FLIGHT was prepared with ICESat-2 ATLAS instrument parameters. Table 3-1 summarizes the parameters used by FLIGHT to simulate photon transport from the planned ATLAS instrument and Table 3-2 reports the solar and atmospheric parameters (including the scattering mode) used for model simulations with the sensor at nadir. The ATLAS parameters were proposed as of August 2012 and, though subject to change, provided the basis for model assumptions regarding instrument design. Key parameters include the laser wavelength (532nm), the laser footprint diameter (10m), laser pulse energy (164 μ J) and the laser footprint spacing (0.7m, or 1.42857 footprint centerpoints m^{-1}).

FLIGHT was operated in ‘photon-counting mode’ for stochastic simulation of photon transport. This mode of the model provides a different set of simulated returns for each link-scale across a forest stand of given set of parameters. For each simulated LiDAR shot (i.e., an $\{X,Y\}$ location), returned photon heights are recorded from features within the synthetic forest stand. A distribution of simulated heights recorded by combining returns for a series of footprints located at 0.7m intervals was compiled by running the model 100 times for each AGB interval for a given link-scale. This procedure was replicated at 10m intervals for link-scales ranging from 20m – 100m. This stochastic process was intended to demonstrate the variability of forest structure measurements from photon counting LiDAR across an AGB gradient divided into 10 Mg·ha⁻¹ intervals collected across a range of link-scales.

Table 3-1. Summary of the parameters used by FLIGHT to simulate photon transport from the planned ATLAS instrument.

Parameter	Value
Operational altitude (m)	496000
Wavelength (nm)	532
Telescope diameter (m)	0.8
Laser pulse energy (μJ)	164
Laser footprint diameter (m) (1/e ²)	10
Telescope field of view (μrad)	83.3 (40m)
Detector efficiency @ 532nm	15%
Swath width (km)	± 3
Beam divergence (rad)	5.04032E-06
Pulse duration (ns)	0.375
Samples · m ⁻¹	1.42857

Table 3-2. Solar and atmosphere parameters for model simulations with sensor at nadir.

Parameter	Value
Irradiance (top of atmosphere) @ 532nm (W·m ⁻²)	1.6
Scattering mode	total
Atmospheric transmittance (1-way, nadir)	0.7

3.3.3. Forest Stand Parameters for FLIGHT

Forest parameters were input into FLIGHT to simulate returns from *Larix* stands with no topographic relief in northern Siberia. FLIGHT requires information on a number of forest stand variables in order to simulate photon transport from and through a particular type of vegetation. Forests of northern Siberia are almost exclusively *Larix*, so forest variables input to FLIGHT were either specific to this forest type, or general to conifer trees where specific parameters were not available. The simulations were run for parameters from theoretical stands within specified AGB intervals. Because of this, the stand parameters (described below) that provided FLIGHT with a set of average forest structure conditions were compiled to statistically represent such AGB intervals.

We collected *Larix* forest stand parameters for theoretical stands where AGB ranged from 0-10 Mg·ha⁻¹ to 90-100 Mg·ha⁻¹. The *Larix* stand parameters were derived from data reported in recent literature and directly from field measurements in *Larix* forests in central and northern Siberia in the summers of 2007, 2008 and 2012 (Alexeyev & Birdsey, 1998; Bjarnadottir, Inghammar, Brinker, & Sigurdsson, 2007; Iida et al., 2009; H. Kobayashi, Delbart, Suzuki, & Kushida, 2010; Montesano, Nelson, Dubayah, Sun, Cook, et al., 2014a; Neigh, Nelson, Ranson, Margolis, et al., 2013b; Osawa & Kajimoto, 2009; Ueyama et al., 2010; Xue et al., 2011). The AGB of these stands was calculated using a *Larix*-specific allometric model (A. Bondarev, unpublished data; Montesano et al. 2014):

$$AGB = 0.00001 * ht * (3.24 * dbh^2 + 6.601 * dbh + 3.361) * z * S \quad (1)$$

where, *AGB* = above-ground biomass density (Mg·ha⁻¹)

S = stem density (number·ha⁻¹)

ht = mean tree height (m)

dbh = mean tree diameter (cm) at breast height (1.3m)

z = timber volume to phytomass scale factor (0.795 for mature, northern Taiga *Larix sp.*)

Stand parameters that were input to FLIGHT were also input to the AGB model, which allowed FLIGHT output to be linked to specific AGB intervals. Table 3-3 summarizes the forest parameters used. Figure 3-1 shows how the FLIGHT input was collected from the coupling of direct field measurements, allometrically-derived metrics, and values gleaned from literature on *Larix* stands. The plots in Figure 3-2 show how forest input forest stand parameters for FLIGHT varied according to AGB bin.

Table 3-3. Summary of the forest stand parameters used for model simulations. Parameters are derived from unpublished field data and previous studies in *Larix* forests (Bjarnadottir et al., 2007; Iida et al., 2009; H. Kobayashi, Suzuki, & Kobayashi, 2007; Wolf et al., 2011; Xue et al., 2011).

Parameter	Value
# of photon trajectories	20000
Plant Area Index (%)	<i>determined by AGB bin, LAI=1.6</i>
Proportion of vegetation (leaf, shoot, bark)	0.2, 0, 0.8
Leaf angle distribution	generalized for conifer
Soil roughness	0 (smooth surface)
Leaf size/clumping	0.05 (clumping within conifers)
Fractional cover of crowns (%)	<i>determined by AGB bin, LAI=1.6</i>
Slope (degrees)	0
Crown shape	conical
Crown dimensions (m) (crown radius, height of crown)	<i>determined by AGB bin</i>
Height to first branch (m)	2.875
DBH mean for scene (cm)	<i>determined by AGB bin</i>
Leaf reflectance, transmittance @ 532nm	10%, 6.5%
Bark reflectance @ 532nm	8%
Soil reflectance @ 532nm	8%

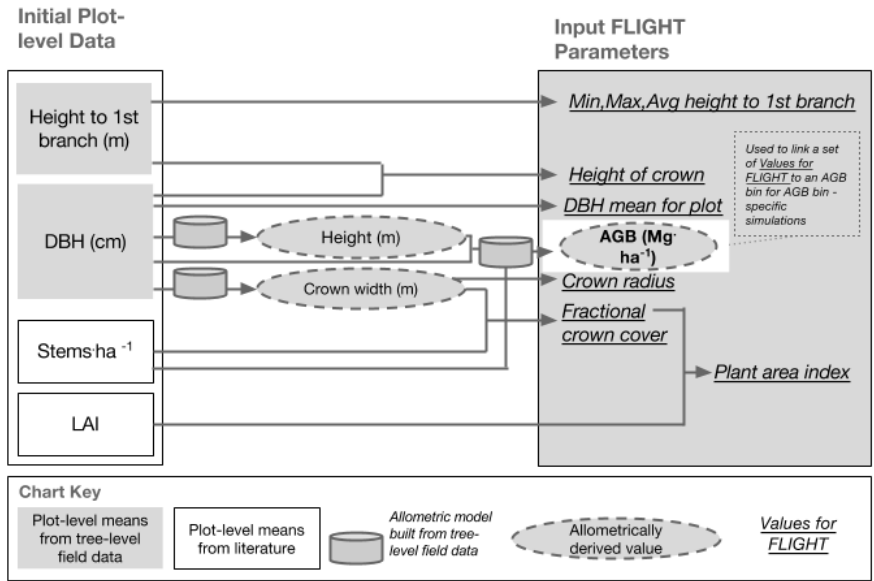


Figure 3-1. Diagram showing the relationship between initial plot-level data and the input FLIGHT parameters used to simulate forest stands for AGB intervals from 10-100 $\text{Mg} \cdot \text{ha}^{-1}$.

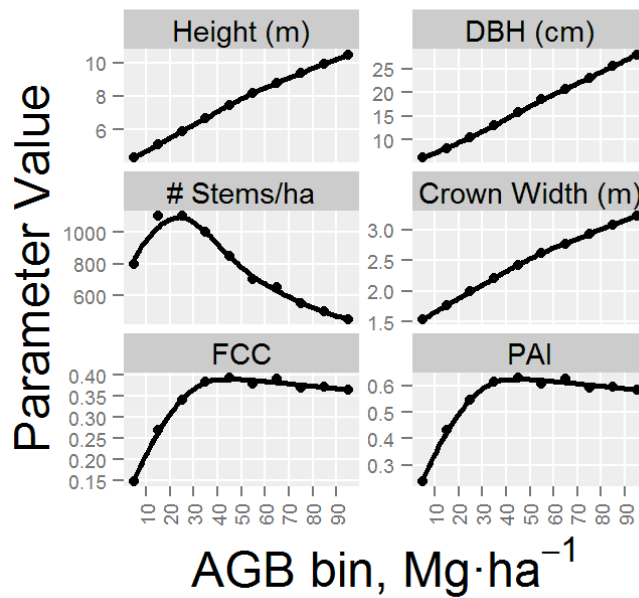


Figure 3-2. Plots showing how FLIGHT input forest stand parameters varied for each AGB bin. DBH = diameter at breast height (1.3m); FCC = fractional crown cover; PAI = plant area index.

3.3.4. Canopy Height Algorithm

Canopy height is the difference between the canopy surface and ground surface elevation measurements of the simulated return photons. Given the instrument parameters described above and shown in Tables 1-3, FLIGHT outputs approximately 1-3 elevation measurements for every footprint location along a specified link-scale. To get an estimate of vegetation canopy height and structure from these data, all elevation measurements along a given link-scale were grouped to form a histogram of binned (0.25m) photon return heights. These histograms include a representation of the structure of the synthetic forest integrated across each link-scale within each AGB interval. However, in addition to a vegetation structure signal, the histograms also include noise returns at elevations above, below and within the vegetation signal. These noise returns are the result of FLIGHT's accounting of the solar background noise derived from the reflection off surface features of solar transmitted radiation. Figure 3-3 provides (a) an example of simulated returns along a link-scale and (b) the corresponding histogram of the vertical distribution of these returns aggregated for the link-scale.

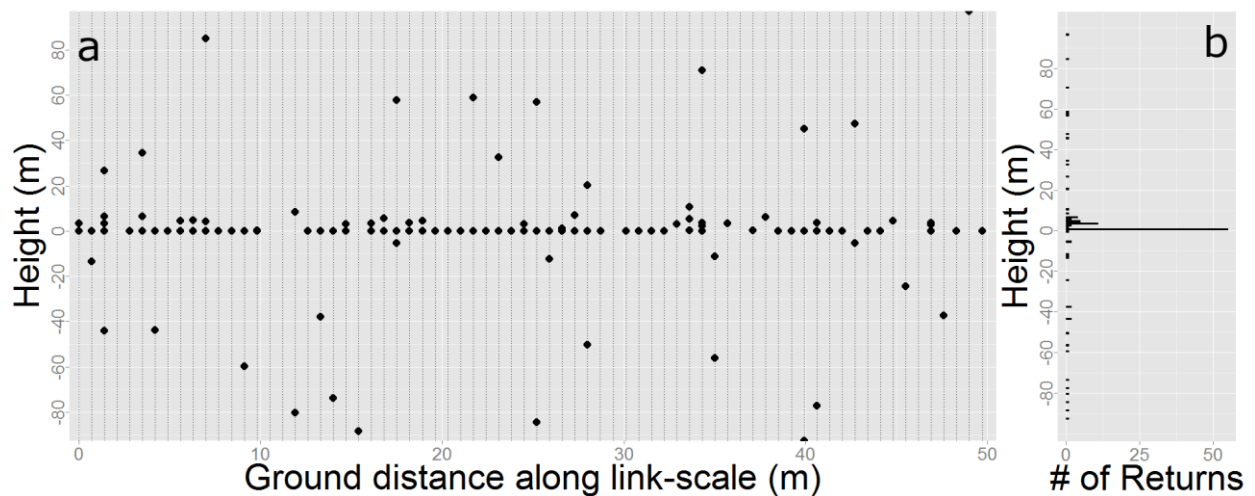


Figure 3-3. (a) An example of simulated returns from FLIGHT along a link-scale (50m). (b) The corresponding histogram of the vertical distribution (0.25m bins) of these returns aggregated for the link-scale. The height on each plot's Y-axis refers to the height above the bin identified as representing the ground surface.

To calculate the vegetation canopy height, both the vegetation canopy elevation and ground elevation must be separated from this noise. In the case of sparse forests examined in this study, the ground return bin is obvious in the histograms because it forms a peak approximately 20 – 50 times larger than the bins with returns from synthetic forest vegetation. However, forest canopy height is not clearly represented because of both the interrupted nature of the sparse canopies and the noise associated with solar background reflectance. The extraction of the vegetation signal requires an algorithm to identify a height from ground above which simulated returns will be ignored.

A canopy height algorithm was developed which uses a 3m long moving vector window applied to the histogram vector (200m). The moving window passes along the histogram vector, summing the corresponding counts (number of photon returns for a bin) of the histogram vector. The photon returns within the 3m moving window are considered noise (not part of a vegetation signal) if the sum is less than a photon return count threshold of 9. When the threshold photon count total is met within the moving window, the highest bin with a count > 0 within this window is identified as the top of the vegetation canopy. With the top of the canopy identified, the photon returns from synthetic forest stands were summed and the relative height (*rh*) metrics were computed. These relative height metrics help characterize the vertical structure of the synthetic forest within a given link-scale. Henceforth, *ht* refers to the canopy height and *rh90*, *rh75*, *rh50* refer to the simulated heights above ground at which 90, 75, and 50% of the received photons from vegetation have been returned to the sensor.

3.3.5. Empirical Modeling

Single variable empirical models, relating each simulated height metric to AGB, were built to predict AGB and examine regression error and error uncertainty within each 10 Mg·ha⁻¹AGB interval. These models were power functions of the form:

$$AGB = \alpha * metric^{\beta}, \text{ where } \alpha \text{ and } \beta \text{ are coefficients of the regression. (2)}$$

Three versions of modeled AGB from a given metric were built to examine the coefficients of determination of each version for each metric at each link-scale. The first version of the empirical models

(R^2_{means}) was built from the means of the per-bin set of simulated height metrics. The second version (R^2_{all}) of the model was fit to all 100 simulated heights within each bin. The final version (R^2_{MC}) performed a Monte Carlo operation to randomly select 1 simulated height from each bin for each height metric at each link-scale, and build a model from those 10 random selections. This approach used bootstrapping with replacement to build 1000 models for each metric at each link-scale. From these models, the distribution of R^2 values was compiled and the mean R^2_{MC} value was compared to R^2_{means} and R^2_{all} .

A multiple variable model relating the simulated height metrics to AGB was built to compare its AGB predictions with those derived from the single variable models. An ensemble decision tree method of 1,000 trees (Random Forests) used all 4 simulated height metrics as predictor variables to model AGB. Three of these predictor variables were selected at random as candidates for determining a tree's node split (the *mtry* parameter). This method, implemented in the R software package (R Development Core Team, 2012), was intended to provide the lower bounds for AGB error and error uncertainty.

3.3.6. Uncertainty Analysis

An uncertainty analysis was performed to evaluate the error (RMSE) and error uncertainty (95% confidence interval for the RMSE) of AGB derived from modeled ICESat-2 return heights from synthetic *Larix* stands. For each simulated height metric, the empirical model linking simulated height to AGB was applied to derive AGB. For each AGB bin, the bin's error was calculated as the RMSE of the set of 100 derived AGB values within each bin. The uncertainty of the error value per bin was reported as a 95% confidence interval (CI). This CI was calculated using two methods (after Montesano et al. 2014).

3.4. Results

3.4.1. Simulated Photon Returns

One hundred FLIGHT simulations of photon counting LiDAR returns across average *Larix* stands in northern Siberia were compiled for each 10 $\text{Mg}\cdot\text{ha}^{-1}$ AGB interval from 0-100 $\text{Mg}\cdot\text{ha}^{-1}$ across link-

scales of 20-90m, at 10m intervals, for a total of 8,000 simulations of photon counting LiDAR measurements. For ~82% of all the simulated LiDAR shots, 1-2 photons were recorded by the sensor (Figure 3-4a). This percentage ranged from 79% - 88% depending on AGB bin and link-scale. However, this distribution changes when it's broken down to photons representing vegetation (signal photons) and those with either negative or above canopy heights (noise photons) (Figure 3-4b). Returned signal photons represent ~67% of all photons returned. Nearly 50% of shots result in 1 signal photon returned (~25% of shots result in 1 noise photon return), while ~17% of shots result in at least 2 signal photons returned (~6% of shots result in at least 2 noise photons returned). It is important to note that some LiDAR shots return a mix of signal and noise photons. Shots for which zero photons were returned were “no data” cases and were given no further consideration.

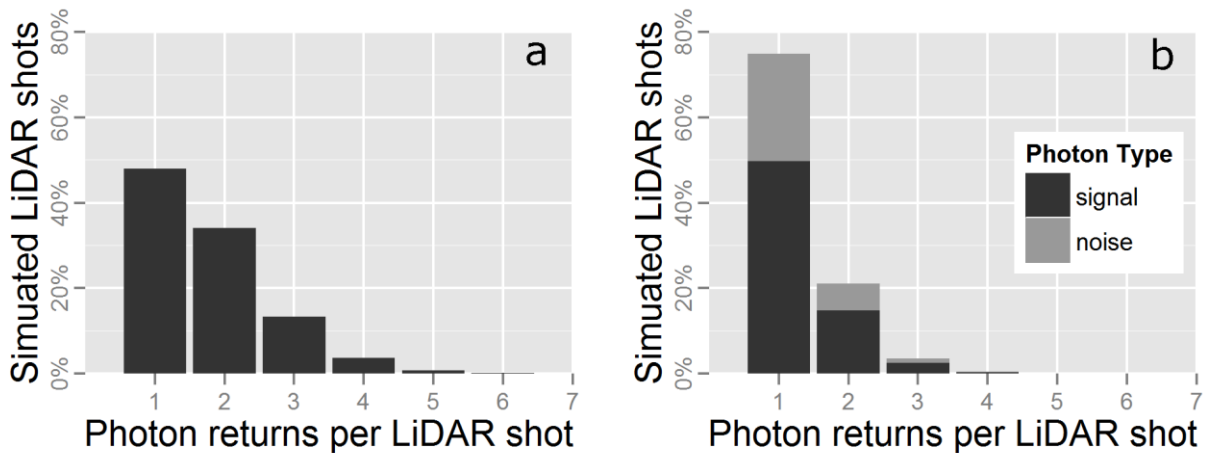


Figure 3-4. (a) Bar plot of the proportion of simulated LiDAR shots for which there were single or multiple photons returned per shot. (b) Stacked bar plot of the proportion of simulated LiDAR shots for which single or multiple signal and noise photons were returned per shot. Each plot shows proportions across all AGB bins and link scales.

Figure 3-5 shows a plot matrix of the distributions of signal photon frequency (signal photons returned per LiDAR shot) across all AGB bins at each link-scale. It provides a means to examine the differences, between all combinations of AGB bins at each link-scale, in the distributions of the signal photon return frequency. These distributions highlight 2 visual and statistical ($p < 0.05$) differences. First, regardless of link-scale, the distribution from the 10 and 20 $\text{Mg}\cdot\text{ha}^{-1}$ bins are different from all other

AGB bins. Second, the distributions across the 20m link-scale are different from those across the other link-scales. Within the other link-scales, the distributions are generally similar (no significant difference from Kolmogorov-Smirnov tests; $p > 0.05$). These results suggest that the signal photon return frequency is consistent across most of the AGB range ($AGB > 20 \text{ Mg}\cdot\text{ha}^{-1}$) for all but the smallest amount of LiDAR data collected (20m link-scale).

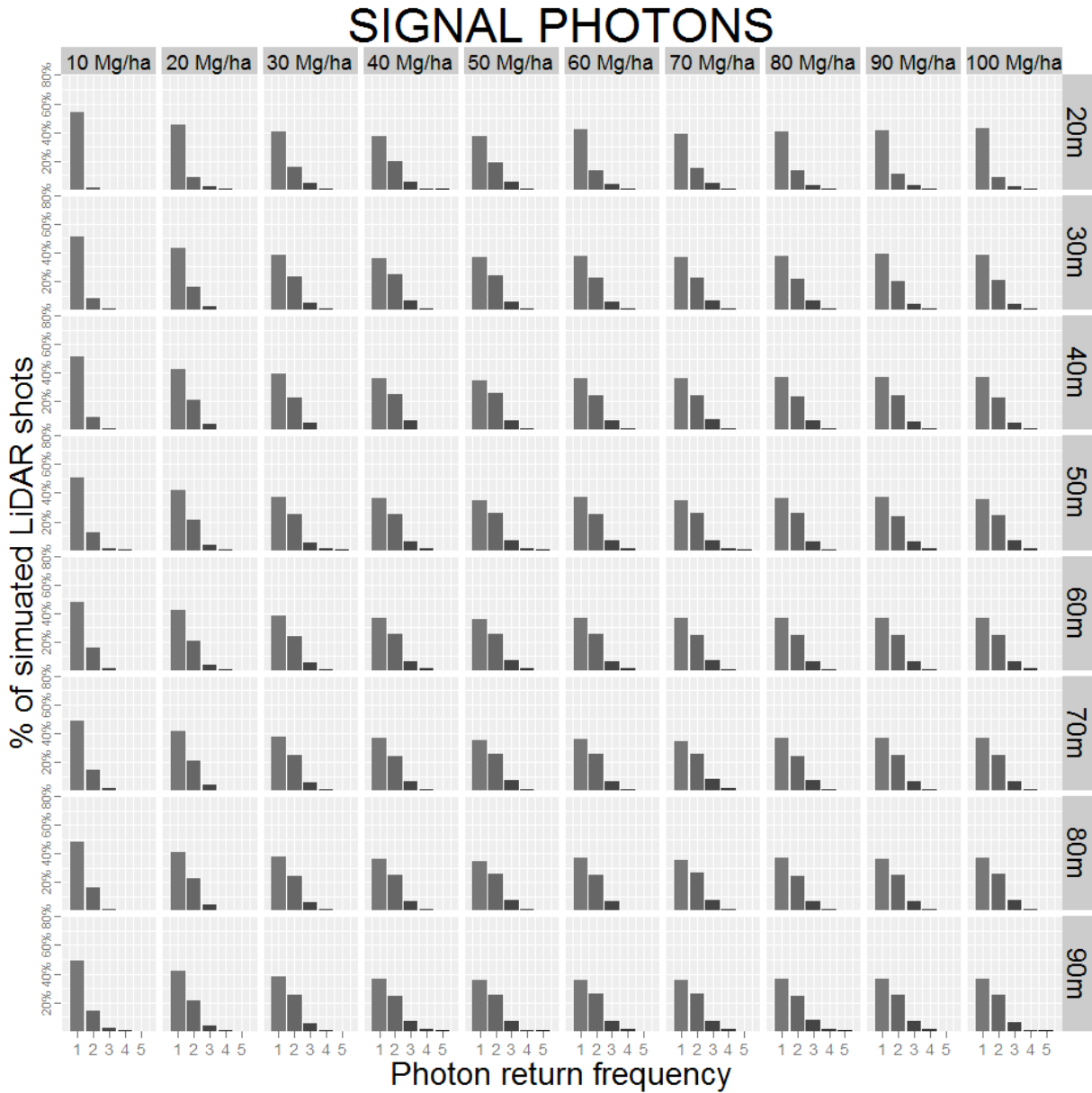


Figure 3-5. A plot matrix showing the distributions of signal photons across all AGB bins at each link-scale.

3.4.2. Simulated Height Metrics

Figure 3-6 shows the distributions of 4 simulated height metrics for each AGB bin of each link-scale. These distributions were computed from 100 simulations run for each of the 10 AGB bins at each of the 8 link-scales. The distributions are depicted with ‘violin plots’ overlaid with conventional box and whisker plots (Hintze & Nelson, 1998). The model line, built from the means of each AGB bin (black dots) is shown for each plot, along with the R^2_{means} value. The R^2_{all} value, derived from a model built from all simulations in each bin, is shown as a means to compare two techniques for assessing the relationship of simulated heights and AGB.

The distributions of simulated heights within each AGB bin show variability that generally decreases from link-scales of 20m to 90m. This variability is greatest for all bins at the 20m link-scale and for the smallest AGB bin through the 40m link-scale. For these bins, the distributions of simulated heights extend to the ground, indicating that some vegetation heights were not identified with the canopy height algorithm. Outliers for which simulated heights are not separate from ground returns exist through the 70m link-scale. Furthermore, the means of the simulated heights for the AGB bins become increasingly linear. Both R^2_{means} and R^2_{all} increase as more simulated height measurements are available across the longer link-scales, and central tendency becomes clearer.

Across all link-scales, the range of simulated heights per bin decreases with the *rh* metric. The corresponding bin-mean values also decrease, resulting in an increasingly more gradual model curve from *ht* to *rh50*. R^2_{mean} values for these models range from 0.6 - >0.99 while R^2_{all} values range from 0.04 – 0.86. The distributions for *ht* show consistently more variability across all link-scales. At smaller link-scales, height metrics have a much broader distribution within AGB bins. This is particularly evident at the 20m and 30m link-scales. At 20m, second quartile portions of the box plots extend to the ground level for all AGB bins. At 30m, outliers for each AGB bin fall at or near (within 1m) of the ground level. Height metrics of 0 meters are shown to occur more often in the simulations at the smaller link-scales.

There is overlap between height metric distributions from adjacent AGB bins. This overlap is greatest for the lowest link-scales and for the largest AGB bins. At 20m and 30m link scales, the overlap

among distributions from adjacent AGB bins is mostly due to the difficulty in discerning the synthetic forest signal from the top of the canopy from noise.

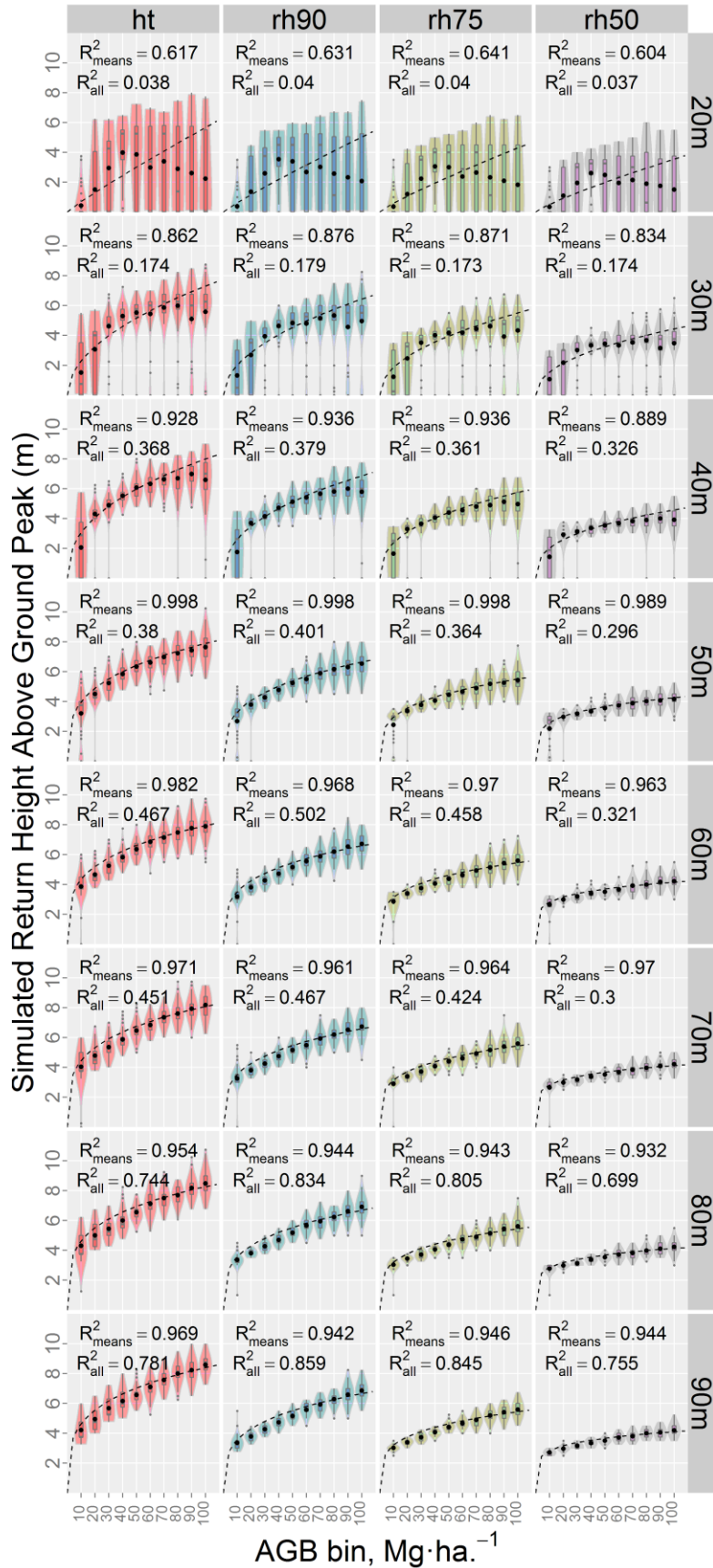


Figure 3-6. Violin plots showing the distribution of height metrics from simulated returns within each 10 Mg·ha⁻¹ AGB bin for each link-scale. The black dots represent the mean metric value for a given AGB bin and the dashed line depicts the model fit to those mean values.

3.4.3. Distribution of Bootstrapped R² of Predictive Models

The R² values resulting from bootstrapping the predictive models relating simulated heights with AGB bin values show the likely proportion of explained variances. Figure 3-7 shows the distribution of R²_{MC} for each height metric at each link-scale. The corresponding R²_{means} (inverted triangle) and R²_{all} (triangle) are plotted for reference. The mean R²_{MC} value is plotted for each metric along with error bars representing the 95% confidence interval. As link scale increases the distributions of R²_{MC} values increase. At the 50m link-scale the difference between the mean R²_{MC} value and R²_{means} becomes less than the difference between mean R²_{MC} value and R²_{all}.

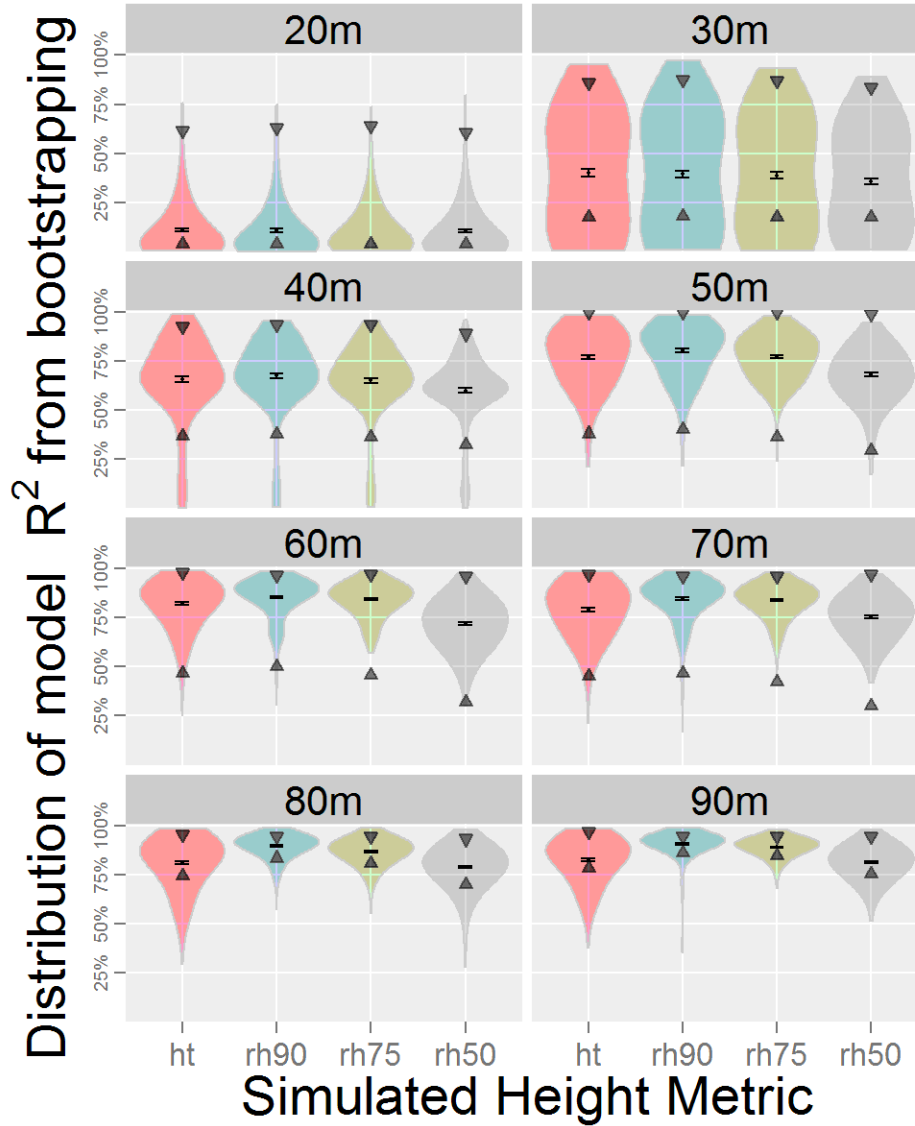


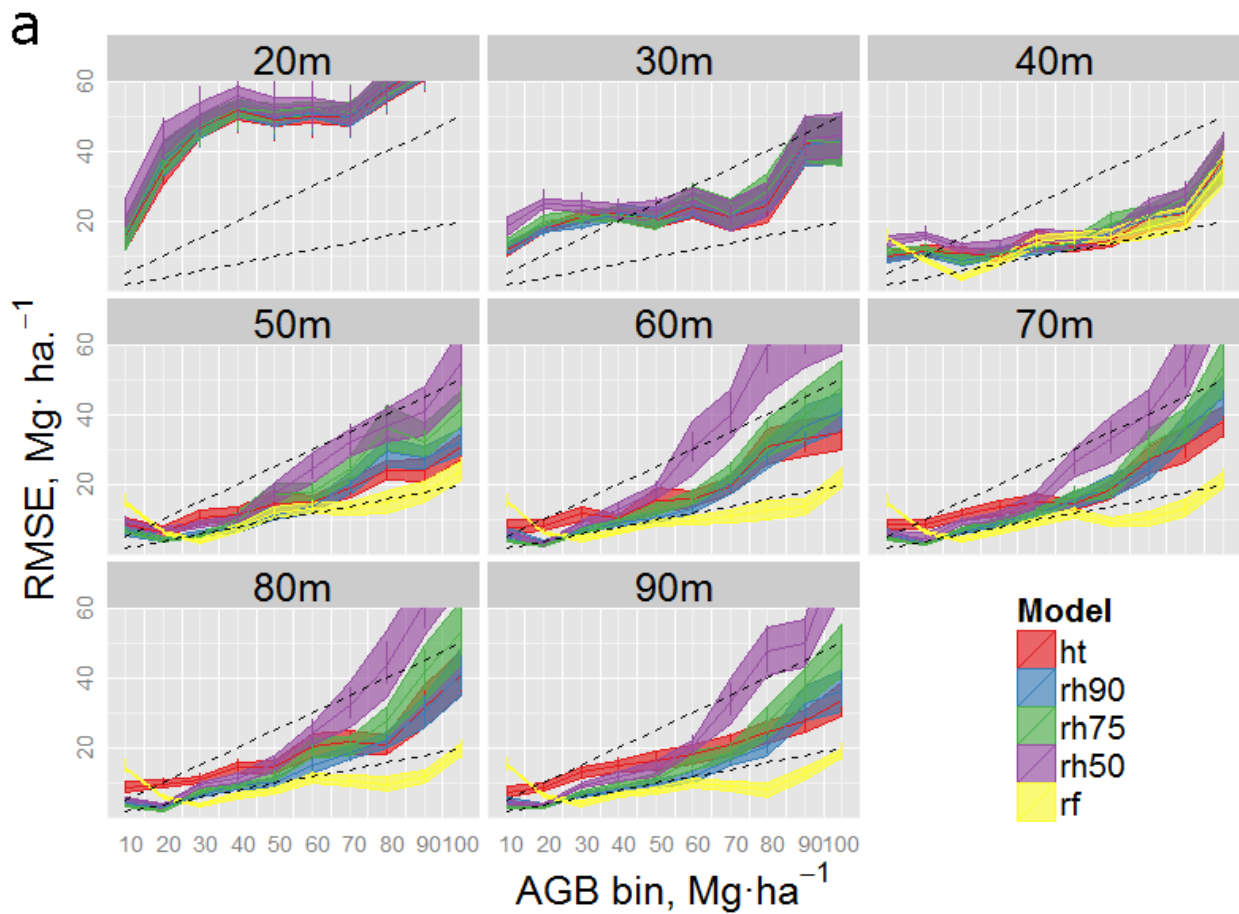
Figure 3-7. Violin plots showing the distribution of 1000 R^2_{MC} values from fitting 1000 empirical models to a randomized transect across a gradient of AGB values. Each random transect was composed of 10 points, where each point was derived from a random selection of a single simulated height within each of the 10 AGB bins.

3.4.4. Error and Error Uncertainty of Derived AGB

The error and error uncertainty of AGB derived from simulated height metrics were examined across all AGB bins and link-scales. Figures 3-8a and 3-8b show curves of the relative regression error and absolute regression error (RMSE), respectively, from single variable models using each of the 4 height metrics. Additionally, these plots show curves derived from multiple variable models using Random Forest (rf). The rf curves are not shown for the 20 and 30 link-scales because the proportion of

overall variance explained was very low (< 0.2). The ribbons (bootstrapping) and vertical bars (chi-square) about each line depict error uncertainty from 2 methods. In both plots, the 20-50% error range is shown in dark grey for reference.

The AGB error and error uncertainty curves across the AGB gradient at each link-scale show three notable findings. First, the trends of each height metric are similar across all link-scales. Second, the error and error uncertainty of the smallest link scales (20 – 30m) fall below 50% error in only 20% of AGB bins. And finally, the 50m link-scale is the smallest at which the error and error uncertainty across the TTE AGB gradient are most frequently below 50%. At this link-scale, AGB error ranges from 20 – 50% (95% CI).



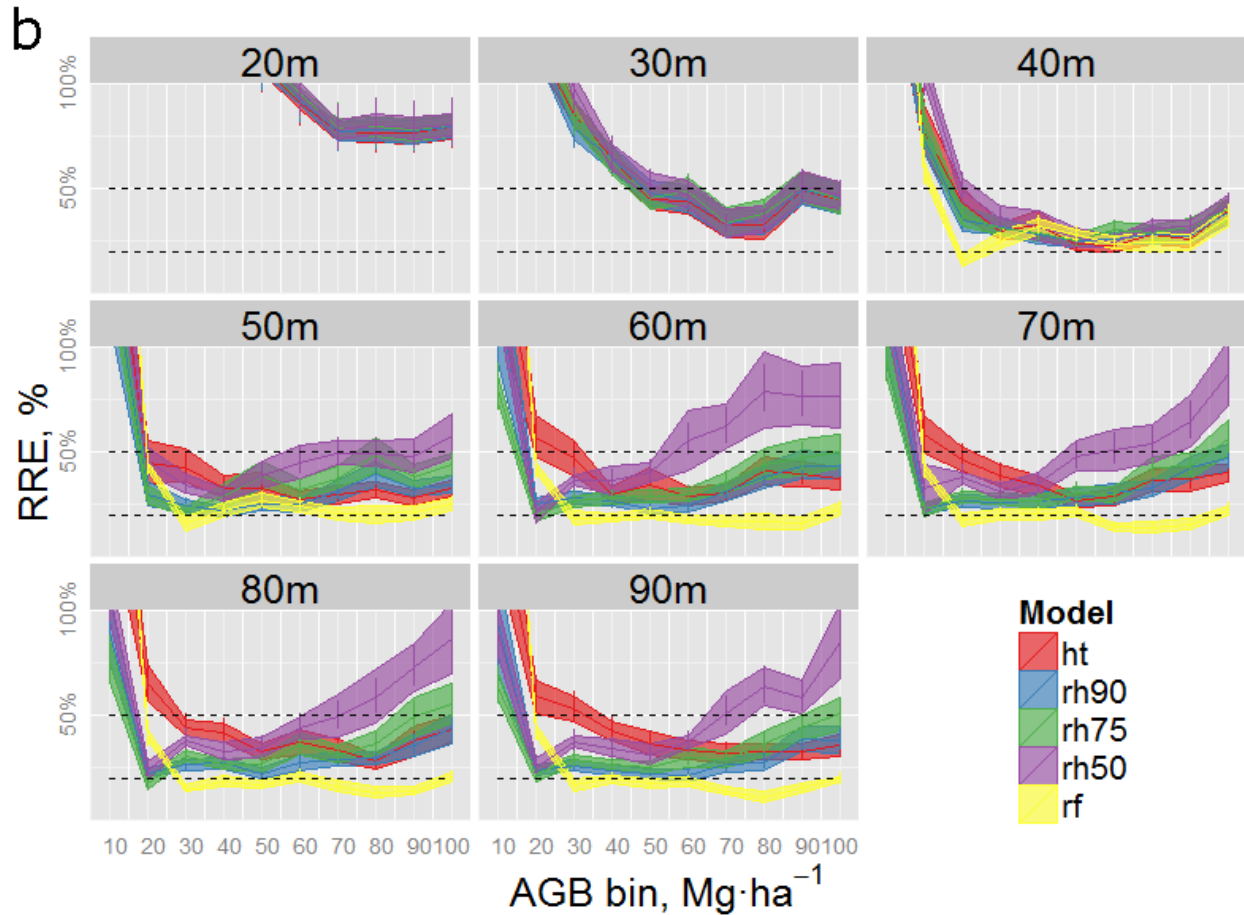


Figure 3-8. Ribbon plots showing the error (RMSE) and error uncertainty in (a) absolute and (b) relative terms of AGB derived from height metrics for each AGB bin. Note (1) that the *rf* ribbons for the 20m and 30m link-scales are not shown because the models on which they were based explained < 20% of overall variation, and (2) the dotted lines, which represent 50% (upper line) and 20% (lower line) error, are shown for reference.

3.5. Discussion

This study provides the vegetation structure science community with one of the first analyses of the capabilities and limitations that may be expected from the ICESat-2 mission. We demonstrate this by examining the uncertainty of inferred AGB from simulated ICESat-2 LiDAR height estimates where short stature ($\sim < 10\text{m}$ in height) *Larix* forests range from 0-100 $\text{Mg}\cdot\text{ha}^{-1}$. Such sparse forests occur across broad extents, exhibit a strong influence on regional and global climate, and are likely to change. This was done by simulating planned ICESat-2 photon counting LiDAR measurements of vegetation height

across a forest gradient typical of the TTE of northern Siberia, building AGB prediction models from common vegetation height metrics, and analyzing the errors and the uncertainty of the error estimates from the difference in the predicted and observed AGB for AGB intervals across a forest gradient.

3.5.1. Photon Returns & Link-scales

One issue underlying the uncertainty of vegetation structure measurements from spaceborne photon counting LiDAR relates to the quantity of LiDAR vegetation height measurements available from which estimates of structure can be made (Dubayah et al., 2010; Hall et al., 2011; Montesano et al., 2013). For photon counting LiDAR data, both the number of vegetation returns (signal photons) per shot and how these shots are combined will affect the uncertainty of inferred AGB. A persisting question concerns the number of LiDAR shots that should be aggregated to adequately characterize the vertical details of vegetation and the cost in terms of horizontal resolution. Even before footprints are aggregated, the geo-location of an individual photon returned from somewhere within the footprint is assigned as coming from the footprint center. By aggregating multiple photon returns, the geo-location detail of the footprints, from which the individual photons returns are derived, is lost in favor of the ability to derive vertical structure information from the distribution of photon return heights collected from many sequential footprints along a LiDAR track. The distribution of photon return heights along a LiDAR collection track provides information on the vertical arrangement of vegetation within the canopy, including canopy height. In doing this, the spatial resolution of vertical vegetation structure moves from the scale of a LiDAR footprint ($\sim 78\text{m}^2$, the approximate area of the simulated ICESat-2 LiDAR footprint) to the scale of a forest patch ($\sim 500\text{m}^2$ for a 50m ICESat-2 link-scale). For estimating forest structure in sparsely forested regions such as the TTE, this issue is of particular interest, because the less dense the trees, the less likely a LiDAR measurement is to come from the top of a tree.

This study analyzed multiple link-scales to examine the accumulation of photon returns across a range of lengths with no topographic relief. These lengths ranged from 20m, which is the approximate diameter of medium footprint airborne waveform LiDAR footprints (LVIS), to 90m, which is $\sim 1.5\text{x}$ the

diameter of a satellite waveform LiDAR footprint (ICESat-GLAS). This range of lengths is interesting to examine in light of the uncertainty of derived AGB estimates reported across forest gradients from other airborne and spaceborne sensors (Montesano et al. 2014) discussed in Section 3.5.2.

The overwhelming majority of LiDAR shots for which returns were recorded had either 1 or 2 height measurements. These returns were derived from the input solar background conditions, including top-of-atmosphere solar irradiance and atmospheric transmittance for the 532nm LiDAR channel with both single and multiple scattering. These conditions were held constant across all simulations and represent difficult data collection condition for photon counting LiDAR (i.e., bright daylight and low vegetation reflectivity). The number of height measurements from each LiDAR shot doesn't show a large change with AGB bin, which suggests that the horizontal resolution of measurements does not need to change with AGB. For AGB inference, the fact that the frequency of signal returns is generally stable across AGB bins $> 20 \text{ Mg/ha}$ for link-scales $> 30\text{m}$ suggests that there is not necessarily a fundamental inability to measure small/sparse vegetation, rather it may be a function of the fractional cover of the vegetation.

3.5.2. Simulated Height Metrics & AGB Uncertainty

Repeated simulations at AGB intervals across a forest gradient provide for a thorough analysis of the central tendency of sparse forest structure measurements and the likely ranges of these measurements. The 8,000 total simulations came from 100 simulations per $10 \text{ Mg}\cdot\text{ha}^{-1}$ AGB bin across 10 bins for 8 different link-scales. Each simulation provided 4 height metrics. The violin plots present the shapes of these distributions from the total set of simulations.

These distributions further highlight the trade-off between the horizontal and vertical resolution of vegetation structure measurements. Broad height distributions across shorter link-scales make for poor model fits and very high AGB bin errors. This leads to overlapping distributions among adjacent AGB bins. Below the 50m link-scale it is particularly difficult to distinguish a height measurement in one AGB

bin from that of an adjacent bin. This overlap highlights the difficulty of resolving AGB at 10 Mg·ha⁻¹ intervals.

The distributions of the bootstrapped R² values (R²_{MC}) demonstrate the variability in the strength of the empirical models. While the mean bin values were used to build the single variable models used to predict AGB and derive per-bin uncertainty estimates, the R²_{MC} value reflects the most likely proportion of variation explained by a model built from a single LiDAR transect across a forest gradient. The shortest link-scale at which $|R^2_{MC} - R^2_{mean}| < |R^2_{MC} - R^2_{all}|$ and $R^2_{MC} > 0.75$ for 3 of the 4 height metrics occurs at 50m, evidence that this length approximates the length at which photon counting LiDAR collection optimizes the trade-off between horizontal resolution and vertical vegetation structure detail for these forest structure conditions.

These simulation results provide advance indication of potential ICESat-2 capabilities for TTE forest gradients. There does not exist for sparse boreal-like forests both ground data and photon counting LiDAR data from airborne instruments (e.g., Sigma Space's 3D Mapper (Rosette, Field, Nelson, DeCola, & Cook, 2011) and the Multiple Altimeter Beam Experimental LiDAR (McGill, Markus, Scott, & Neumann, 2013)). As such, these simulations could not be compared with results from similar photon counting LiDAR estimates of sparse boreal-like forest structure. However, Montesano et al. (2014) report uncertainty for current airborne and spaceborne LiDAR (waveform and discrete) and SAR across such a gradient. While these reported uncertainty figures for other airborne and spaceborne estimates are based on much smaller samples for each AGB bin, the magnitude of errors and trends are similar to those reported from the FLIGHT simulations of ICESat-2 LiDAR data in this study. Of particular interest is the comparison with the results from the spaceborne waveform LiDAR from ICESat-GLAS reported in Montesano et al. (2014), because vegetation structure data from ICESat-2 may update vegetation structure measurements from those of its predecessor. At the 50m link-scale, the ICESat-2 simulation results from the single variable models have lower error and error uncertainty of inferred AGB across the gradient compared to those of ICESat-GLAS reported in Montesano et al. (2014). This includes errors between 25-50% down to the 20 Mg·ha⁻¹ interval. It is important to note that the ICESat-2 uncertainty results may

have been reduced relative to those from ICESat-GLAS due to a greater number of per bin samples ($n = 100$ simulations per bin), which were generally 2-5 times the number available for the ICESat-GLAS analysis. The uncertainty results may have been further reduced because the atmospheric, solar, and forest conditions were kept constant when repeating simulations within an AGB bin. The real-world field samples used to derive the ICESat-GLAS results could not have been controlled for in such a way.

3.5.3. Implications of AGB Uncertainty

The simulation results suggest that at the 50m link-scale in the TTE, ICESat-2 data can infer $AGB > 20 \text{ Mg}\cdot\text{ha}^{-1}$ with AGB error $< 50\%$ at the 95% confidence level. Any forested areas with apparently differing inferred AGB but overlapping AGB error confidence intervals will not show a statistical difference in AGB. This makes identifying AGB differences across the TTE with the upcoming spaceborne LiDAR problematic, because of the apparent inability to resolve much of the AGB gradient below $100 \text{ Mg}\cdot\text{ha}^{-1}$. Furthermore, it is unlikely that spaceborne LiDAR alone will be able to detect vegetation structure changes that may be coincident with biome boundary shifts. However, it is important to continue to explore the combined use of multiple spaceborne datasets and derived products, at a range of scales, and highlight the advantages and drawbacks from particular combinations (data fusion applications) for specific vegetation forms.

3.5.4. Limitations of AGB Uncertainty Estimates

The overall error and error uncertainty estimates for inferred AGB involve a complex interaction of factors (McMahon, Dietze, Hersh, Moran, & Clark, 2009). We discuss three central sources of error that may influence the AGB error and error uncertainty results of this modeling work, and note that the three issues with the empirical models relating to the uncertainty estimates discussed in Montesano et al. (2014) also apply.

First, errors are associated with the initialization of FLIGHT. These errors stem from the use of static *Larix* parameters instead of a distribution, and the use of randomized forest stands instead of a consistent one. These decisions, which decrease and increase uncertainty, respectively, affect the overall

uncertainty of AGB error. These parameters were derived either from field data collected from, or literature reporting on, stands of exclusively or predominantly *Larix*. However, the data used to set-up FLIGHT runs for each AGB bin were done so for average stand conditions for the given interval. Each input stand parameter was constrained to ensure that the resulting AGB calculation from those values fell within the coincident AGB bin. Certainly, an individual parameter has a distribution of potential values even within each bin, yet, simulations were not performed to explore the uncertainty that would result from such distributions. The randomized stands generated by FLIGHT for each simulation differ from simulations based on standardized input such as a stem map. Because of this added randomization, it is expected that the reported uncertainty is higher than it otherwise would be from standardized stem map input. The net effect of how these errors affect the final AGB error and error uncertainty is unexplored. However, the differing forest stands that result from the randomization help make the results applicable to broad extents of *Larix*-dominant TTE.

Second, the modeling of AGB from vegetation height introduces uncertainty into the final inference of AGB and the derived error of those inferences. The empirical model for inferring AGB was built specifically for *Larix* trees. However, this study does not account for model parameter uncertainty that may be derived in part from site-specific variation in tree characteristics and allometries. In this sense, this study uses a universal *Larix* model and does not account for how this universal model may change for different ecotone forms (Dietze, Wolosin, & Clark, 2008; M. A. Harsch & Bader, 2011). The RMSE values derived from these models and used as a measure of overall error and error uncertainty do not comprehensively reflect allometric uncertainty. However, the use of the RMSE in this simulation study is not limited by plot size and sensor geo-location errors as are empirical studies that relate ground plot data to remote sensing measurements (Montesano, Nelson, Dubayah, Sun, Cook, et al., 2014a; Zolkos et al., 2010).

Third, solar background noise can disguise and attenuate the LiDAR return signals from vegetation. When modeling LiDAR returns, this type of noise is included in the model in order to produce simulations that more realistically reflect the effects of solar conditions on model results. In

these simulations, it was accounted for by including the solar transmitted light from bright daylight conditions that is reflected off surface features. These solar conditions, along with the low vegetation reflectivity values input to FLIGHT, likely attenuated the simulated signals from vegetation. Another, perhaps more accurate, methodology for accounting for solar background noise would be to use a surface bidirectional reflectance distribution function within the LiDAR footprint.

3.6. Conclusions

The goal of this study was to examine the error and error uncertainty of AGB derived from modeled forest height returns from synthetic *Larix* stands in the TTE across multiple link-scales. Under bright daylight and low vegetation reflectivity, the results show that 1-2 photons are returned for 79% - 88% of LiDAR shots. The returned signal photons represent ~67% of all photons returned, and nearly 50% of shots result in 1 signal photon returned. The distributions of the number of these returns don't change significantly across the AGB gradient above 20 Mg·ha⁻¹. The link-scale of 50m approximates the optimal balance between horizontal and vertical resolution of vegetation structure in these sparse boreal forests because it is the link-scale at which the greatest proportion of model variation is explained. At this link-scale AGB > 20 Mg·ha⁻¹ has AGB error from 20 - 50% at the 95% confidence level. These results suggest that the theoretical sensitivity of ICESat-2 LiDAR measurements alone lack the ability to discern differences in inferred AGB at 10 Mg·ha⁻¹ intervals in sparse forests characteristic of the taiga-tundra ecotone.

Chapter 4: The Uncertainty of Plot-Scale Forest Height Estimates from Complementary Spaceborne Observations in the Taiga-Tundra Ecotone

4.1. Abstract

Satellite-based estimates of vegetation structure capture broad-scale vegetation characteristics as well as differences in vegetation structure at plot-scales. Active remote sensing from laser altimetry and radar systems is regularly used to measure vegetation height and infer vegetation structural attributes, however, the current uncertainty of their spaceborne measurements is likely to mask actual plot-scale differences in vertical structures in sparse forests. In the taiga (boreal forest)—tundra ecotone (TTE)—the accumulated effect of subtle plot-scale differences in vegetation height across broad-scales may be significant. This paper examines the uncertainty of plot-scale forest canopy height measurements in northern Siberia *Larix* stands by combining complementary canopy surface elevations derived from satellite photogrammetry and ground elevations derived from the Geosciences Laser Altimeter System (GLAS) from the ICESat-1 satellite. With a linear model, spaceborne-derived canopy height measurements at the plot-scale predicted TTE stand height ~5 m—~10 m tall ($R^2 = 0.55$, bootstrapped 95% confidence interval of $R^2 = 0.36-0.74$) with an uncertainty ranging from ± 0.86 m—1.37 m. A larger sample may mitigate the broad uncertainty of the model fit, however, the methodology provides a means for capturing plot-scale canopy height and its uncertainty from spaceborne data at GLAS footprints in sparse TTE forests and may serve as a basis for scaling up plot-level TTE vegetation height measurements to forest patches.

4.2. Introduction

Boreal vegetation structure is an important factor in the arctic climate system (Bonan et al., 1992; Chapin, 2005). Satellite-based estimates of vegetation structure capture broad-scale (e.g., across ecoregions) vegetation characteristics and as well as differences in vegetation structure at plot- or site-

scales (e.g., $\sim 100 \text{ m}^2$ –1 ha), which have a direct effect on ecosystem processes. The taiga-tundra ecotone (TTE) at the convergence of the boreal forest and un-forested tundra has heterogeneous tree cover, and has seen recent widespread, yet variable, changes in vegetation structure (Elmendorf et al., 2012; Epstein et al., 2013; M. Harsch et al., 2009; V. I. Kharuk et al., 2006; Ranson et al., 2011). Vegetation structural attributes, such as height, may influence ground temperatures, active-layer depth, albedo, and atmospheric warming (Blok et al., 2010; Bonfils et al., 2012; Lawrence & Swenson, 2011; Loranty et al., 2013; Loranty & Goetz, 2012; Myers-Smith et al., 2011; Pearson et al., 2013). The TTE is also variable in its response to environmental change, likely a result of interacting environmental factors including substrate, disturbance history, and geographic position (Epstein et al., 2004; G. M. MacDonald et al., 2008; Ropars & Boudreau, 2012).

TTE vegetation height is neither spatially uniform in its current state nor in the manner in which it is changing (Lloyd et al., 2011). Spaceborne remote sensing that provides a synoptic perspective of certain plot-level details may help improve understanding of the net effect of these feedbacks on the climate system and the relative control from site factors (Bonfils et al., 2012; Loranty et al., 2011). The synoptic yet detailed perspective of plot-level vegetation characteristics and spatial arrangement derived from high-resolution ($< 5 \text{ m}$) spaceborne remote sensing (e.g., Worldview-1, -2, -3, GeoEye-1, and IKONOS) may help resolve observed disagreement between coarse-scale remote sensing results and plot-level characteristics in a systematic manner (Epstein et al., 2013; Hofgaard et al., 2012).

Vegetation structure, including forest height, has been estimated from a variety of spaceborne sensors at a range of scales (Baccini et al., 2008; Cartus, Kellndorfer, Rombach, & Walker, 2012; Duncanson, Niemann, & Wulder, 2010; Hansen et al., 2013; Heiskanen, 2006; M. A. Lefsky, 2010; M. A. Lefsky et al., 2005; Los et al., 2012; Neigh, Nelson, Ranson, Margolis, et al., 2013b; Ranson & Sun, 1997; Ranson, Sun, Kharuk, & Kovacs, 2004; Santoro et al., 2013; Simard et al., 2011; G. Sun, Ranson, Masek, Guo, Pang, Fu, et al., 2008a). The direct measurements of structure from active remote sensing from light detection and ranging (LiDAR) and synthetic aperture radar (SAR) continue to be regularly used to estimate vegetation height and infer structural attributes across a range of vegetation types. Often,

spaceborne data has been coupled with airborne LiDAR surveys to link ground inventories with satellite measurements (Neigh, Nelson, Ranson, Margolis, et al., 2013b; R. Nelson et al., 2010; Wulder & Seemann, 2003; Wulder, Han, White, Sweda, & Tsuzuki, 2007). However, large portions of the TTE are difficult to access because they are remote and often require an airborne inventory involving multi-national cooperation. As such, the availability of the airborne component of remote vegetation structure measurements in the TTE is highly irregular. At this point, the systematic sampling available across the entire TTE offered by spaceborne instruments will likely yield the only comprehensive remote vegetation estimates.

Spaceborne estimates from SAR and LiDAR at the plot-scale in the TTE, however, have errors of inferred structure (above-ground biomass density) that are uncertain and relatively large (~50%) (Montesano, Nelson, Dubayah, Sun, Cook, et al., 2014a). Spaceborne SAR sensors estimate plot-level vegetation structure with high uncertainty due to the need to average many contiguous radar pixels, which causes conflicts of scale with ground data (Hensley et al., 2014). Spaceborne LiDAR from the Geoscience Laser Altimeter System (GLAS) on the ICESat-1 satellite has difficulty capturing canopy surface in sparse and short stature forests (R. Nelson, 2010). In the TTE, the uncertainty of these measurements alone may mask subtle yet significant plot-level vegetation height differences (e.g., 0.5 m–4 m) that may play a central role in the prediction of climate feedbacks in the high northern latitudes (Bonfils et al., 2012; Esper & Schweingruber, 2004).

High resolution spaceborne imagery (HRSI) is increasingly being used for understanding detailed vegetation structural characteristics (Berner et al., 2012; Montesano et al., 2009; M. Urban et al., 2014), particularly vegetation height (Hirschmugl, Ofner, Raggam, & Schardt, 2007; Hobi & Ginzler, 2012; Neigh et al., 2014; Petrou et al., 2014; Praks, Hallikainen, Antropov, & Molina, 2012). More work into the use of HRSI for deriving vegetation heights in the TTE is warranted given their ability to resolve individual trees and tree shadows, their stereo viewing capabilities, and the importance of vegetation height on biophysical processes in the Arctic. With mounting HRSI data volumes, there is an increased

opportunity to exploit the most useful characteristics of these data to refine spaceborne measurements of vegetation structure (Neigh, Masek, & Nickeson, 2013a).

The availability of a variety of vegetation observations provides an opportunity to explore how these data complement each other to reduce uncertainty in measurements of vegetation characteristics. Complementary datasets may be those whose best observations depict different characteristics and, when combined, can provide a single measurement that would otherwise be unavailable with one dataset alone. Observations of current vegetation may be improved with archival or legacy data from different sensors acquired at different times, to derive vegetation structure characteristics. These applications and measurements could be useful for a broad spectrum of spatial scientists (Boyle et al., 2014) if the uncertainty associated with the measurements is well-documented.

An example of complementary satellite measurements of TTE vegetation structure may come from GLAS LiDAR and Worldview-1. Each make a direct and unique measurement of surface features that can provide information on vegetation structure (Chopping, 2011; Zwally et al., 2002). The spatial resolution of these measurements (50–60 m major axis for the elliptical GLAS footprint; ~0.5 m pixel size for HRSI from Worldview-1) are at scales well suited for comparison with field plot measurements that typically range from ~100 m²–~1 ha.

These two sensors, however, are quite different. GLAS was a laser altimeter that derived feature elevation by measuring the vertical distribution of laser energy returned to the sensor (waveform) within a laser footprint. GLAS operated from a ~600 km orbit at 40 Hz, and thus had a footprint sampling frequency of ~170 m along-track (T. J. Urban, Schutz, & Neuenschwander, 2008). For forest structure studies, GLAS waveform data have been used to measure both ground and canopy surface elevations, providing canopy height information. However, GLAS has difficulty measuring ground surface elevation beneath dense forests, resulting in a relatively high uncertainty of vegetation height estimates in these forests (Simard et al., 2011). Furthermore, GLAS estimates of vegetation height in sparse forests are highly uncertain because of its inability to resolve the vegetation canopy, yet produce a stronger ground surface signal (Carabajal & Harding, 2006; Popescu, Zhao, Neuenschwander, & Lin, 2011; Yi, Zwally, &

Sun, 2005). GLAS vegetation height estimates may become less relevant with time as vegetation changes, however its estimates of ground surface elevations may continue to serve as robust ground elevation reference globally for areas with little to no ground elevation changes (e.g., from land subsidence due to groundwater extraction or permafrost melting). They may be particularly useful where ground and airborne survey is difficult, expensive or otherwise unlikely.

Direct spaceborne observation of surface elevations from HRSI are made with stereo photogrammetric measurements of surface features (Jacobsen, 2003). The HRSI Worldview-1 sensor (HRSI_{WV1}) is an imaging spectrometer that records, in a panchromatic channel (397 nm–905 nm, centered on 651 nm), the spectral characteristics of surface features in the visible and near-infrared wavelengths. It derives feature elevations from the difference in apparent position of image features from geographically overlapping portions of multiple images (image parallax). Digital surface models (DSMs) from these data over densely forested areas measure elevation at the canopy surface, but the ground beneath is not visible and thus cannot be measured. Measurements of sparsely forested areas have the potential to provide ground surface and canopy surface elevations. However, it should be noted that the canopy surface represented may not represent the tallest tree. The vertical and horizontal accuracies of these models are related primarily to the convergence angle formed from the sensor-target geometry of the acquisition of the stereo image pairs (M. A. Aguilar, del Mar Saldana, & Aguilar, 2014; R. Li, Niu, Liu, Wu, & Deshpande, 2009; R. Li, Zhou, Niu, & Di, 2007). The utility of the convergence angles in determining the accuracy of short feature height measurements (such as small trees) is an on-going line of inquiry. Both GLAS and HRSI_{WV1} can be processed to provide samples of ground surface and canopy surface elevations, from which canopy height is derived.

The objective of this paper is to evaluate the uncertainty of canopy height estimates from complementary spaceborne measurements in the TTE. This uncertainty will be derived from the modeled relationship of plot-scale *Larix* forest stand height from coincident ground sampled tree heights and canopy height estimates from a combination of GLAS and HRSI DSM elevation measurements. The uncertainty is comprised of the model error and the bootstrapped distribution of that error. It demonstrates

the fundamental range of derived errors of TTE forest stands from direct spaceborne height measurements at the field plot scale and provides insight for a model used to extend plot measurements of canopy height to GLAS footprints with coincident HRSI DSMs.

4.3. Methods

We analyzed ground measurements of individual tree heights, GLAS- and HRSI_{WV1} DSM - derived measurements of ground surface elevation, and spaceborne estimates (*i.e.*, a combination of GLAS and HRSI_{WV1} DSM measurements) of maximum forest canopy heights in sparse *Larix* forests in northern Siberia (Figure 4-1). The ground-derived heights were collected in field surveys described in Section 4.3.1. The acquisition and processing of HRSI_{WV1} and GLAS data are described in Sections 4.3.2 and 4.3.3, respectively. The GLAS- and HRSI_{WV1}-derived measurements of ground surface elevation were examined for non-forest and forest sites across northern Siberia. Finally, spaceborne forest canopy height estimates were calculated as the difference of ground surface elevations measurements (from either GLAS or HRSI_{WV1} DSMs) and canopy surface elevation measurements (from HRSI_{W1} DSMs) at field plots centered on GLAS footprints in forest stands. This analysis is detailed in Section 4.3.4.

4.3.1. Field Data

We examined a set of field data collected in *Larix* forest stands, part of a multi-year field NASA-lead campaign to collect forest structure measurements in the Central Siberian Plateau in 2007, 2008, and 2012. The set of cloud-free image data (described in Section 4.3.3) corresponding to field plots limited the geographic scope of the canopy height analysis described in Section 4.3.4 to plots along the Kotuykan River in the Anabar Plateau in northern Siberia, sampled in July–August 2008. Trees surveyed were located in primarily mature forest stands that exhibited no visible signs of recent disturbance from fire. Field plots were circular with a radius of 10 m or 15 m. The field plots were geo-located with hand-held global positioning system units to within ± 5 m and centered on the elliptical GLAS footprints (50–60 m major axis) along elevational transects with little within-footprint slope ($\sim < 10^\circ$). Plot boundaries were established from this center point using tape measurement of the plot's radius to mark the plot's edges

along its circumference. The footprints selected for field sampling were those for which (1) footprint-centered field plots were representative of larger footprint sampled by GLAS and (2) the vegetation signal was not influenced by clouds or slope (Montesano, Nelson, Dubayah, Sun, Cook, et al., 2014a; Neigh, Nelson, Ranson, Margolis, et al., 2013b). This field sampling protocol, used in a number of other studies, was designed for comparison with GLAS measurements of forest structure whereby each plot coincides with a unique GLAS footprint (Montesano, Nelson, Dubayah, Sun, Cook, et al., 2014a; Neigh, Nelson, Ranson, Margolis, et al., 2013b; R. Nelson et al., 2009). Thus, forest structure data was collected for a ground surface area that was most likely to coincide with the strongest portion of the transmitted GLAS LiDAR pulse. Additionally, ground plots were sized to provide sufficient sampling to characterize forest structure within a GLAS footprint while also allowing for sampling of a range of GLAS footprints across the study area.

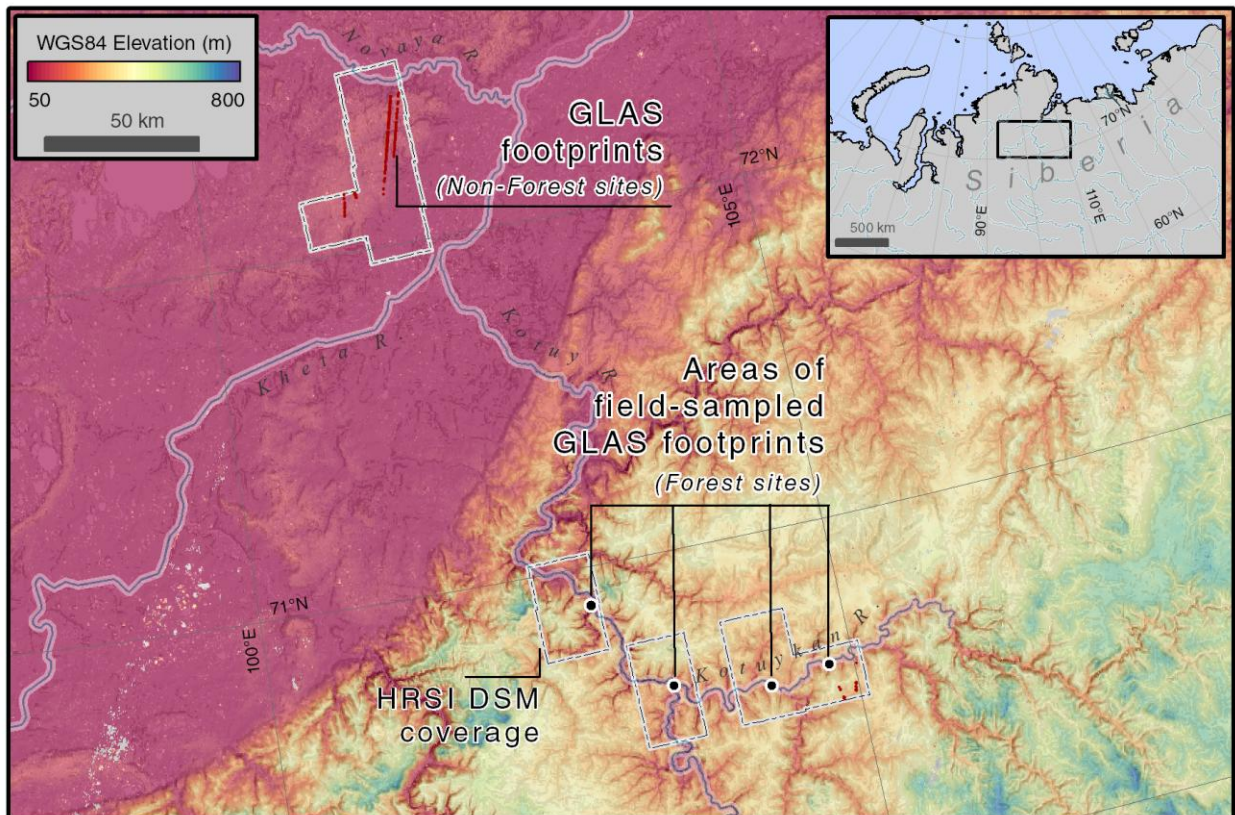


Figure 4-1. The northern Siberia study area showing the spatial coverage of Worldview-1 digital surface models, the spaceborne LiDAR footprints at non-forest sites, and the forested areas where spaceborne LiDAR footprint field sampling was carried out.

4.3.2. HRSI Data Acquisition and Processing

The HRSI data was acquired from the National Geospatial Intelligence Agency through an agreement with the US Government [50]. Cloud-free HRSI stereo pairs, *i.e.*, two images of overlapping geographic extent acquired at different sensor view angles, were collected over northern Siberia in winter and summer 2012 by the Worldview-1 satellite. Each HRSI_{WV1} stereo pair was acquired along track using the near simultaneous fore and aft images. These panchromatic images have a spatial resolution of ~0.5 m. Cloud-free image pairs for *Larix* forests reveal individual and groups of *Larix* trees, regardless of season. Each image pair has a portion of geographic overlap used to derive surface elevations with the suite of stereo photogrammetric routines available from the open source NASA Ames Stereo Pipeline (ASP) 2.4 software available (along with the User's Guide) at <http://ti.arc.nasa.gov/tech/asr/intelligent-robotics/ngt/stereo/> (Moratto, Broxton, Beyer, Lundy, & Husmann, 2010).

The routines in ASP provide automatic stereo photogrammetric mapping of surface features. An image correlation sub-routine matches the corresponding pixels of image pairs, establishes epipolar geometry, and calculates the distance from the image focal plane to the earth surface features. A discussion of this process is presented in Ni *et al.*, (2014) (Wenjian Ni, Ranson, Zhang, & Sun, 2014). The advantage of the stereo pairs derived from along-track collection is that it provides images that are better suited for image matching algorithms. These image matching algorithms rely on radiometric and textural similarities among corresponding image pixel blocks. During the image matching portion of the routine, the linear camera model and the affine adaptive window mode option (subpixel mode = 2 in ASP) was used to provide the most accurate surface elevation results (Ames Stereo Pipeline User's Guide, 2014). The horizontal accuracy of HRSI_{WV1} DSMs are expected to be <3.5 m (Capaldo, 2012), without the use of ground control. The use of ground control was not implemented in order to produce results from stereo pair processing that were fully automated.

For each stereo pair, a gridded HRSI_{WV1} DSM was generated at $\sim 0.4\text{--}0.7$ m spatial resolution. This output HRSI_{WV1} DSM spatial resolution range was dictated by the native resolution of each stereo pair image, itself a function of sensor viewing geometry, which varied from image to image. The units of the pixel values were in meters above the WGS84 ellipsoid and represent the elevation of visible surface features. For forested areas, these DSMs provide a canopy surface elevation.

4.3.3. GLAS Data Acquisition and Processing

The GLAS level-2 global land surface laser altimetry was acquired from the National Snow and Ice Data Center (<http://nsidc.org/data/gla14>). GLAS metrics (GLA14) were acquired for GLAS footprints from campaigns L3a, L3c, L3d, L3f, and L3g (October–November 2004, May–June and October–November in 2005 and 2006) across a broad extent of northern Siberia ($60\text{N--}75\text{N}$, $90\text{E--}110\text{E}$). The 50–60 m GLAS footprints used were collected with a 1064 nm laser and have a horizontal geo-location accuracy of ~ 4.5 m (Hieu Duong, Lindenbergh, Pfeifer, & Vosselman, 2009; T. J. Urban et al., 2008). This dataset included those GLAS footprints sampled during field surveys. The cloud-free image extents for available HRSI_{W1} DSMs corresponded to non-forested and field-sampled forested GLAS footprints along the Kotuykan River and non-forested GLAS footprints north of the Kheta River.

The GLA14 data provided the ground surface elevation used in the analysis. Two GLA14 metrics were used to provide estimates of ground surface elevation. These metrics were (1) the elevation above the WGS84 ellipsoid of the GLAS waveform centroid ($elev_1$) and (2) the GLAS waveform centroid height above the waveform's lowest gaussian peak ($centroid$), which was assumed to represent the average ground surface elevation within a footprint. The original GLA14 elevation values in the TOPEX/Poseidon ellipsoid were converted to WGS84 ellipsoid values to account for the 71 cm vertical shift in our study area. These GLA14 metrics were used to derive a single ground surface elevation at field plot centers in two ways. The first was to subtract the height of the centroid from the elevation of the centroid ($elev_2$). The second was to simply use the elevation of the centroid ($elev_1$). Finally, the length of the waveform from signal beginning to signal end ($wflen$) was used for filtering out data whose waveforms may have

been elongated due to terrain slope or cloud contamination. These metrics have been used previously as part of algorithms to derive canopy heights for GLAS footprints (M. A. Lefsky et al., 2005; G. Sun, Ranson, Masek, Guo, Pang, Fu, et al., 2008a).

4.3.4. Analysis

A two-step process was used to examine the uncertainty of forest canopy height estimates using a combination of GLAS ground elevation and HRSI_{WV1} DSM-derived surface elevation. First, we examined the correlation and uncertainty (the bootstrapped root mean square difference; RMSD) between flat ground surface elevation measurements from coincident locations measured by both GLAS and HRSI_{WV1} DSMs at unforested (*i.e.*, tundra) and forested sites in northern Siberia. This was done to quantify the relative difference between ground surface elevation measurements from each sensor for land covers in which (1) the ground surface elevation measurements are not obscured by trees (*Non-Forest*); and (2) the ground surface is partially obscured by trees (*Forest*). The *Non-Forest* sites were 10 m radius circles centered on GLAS footprints that were classified as free of tree or high shrub vegetation. This classification was done in a geographic information system by overlaying GLAS footprints on HRSI_{WV1} , manually interpreting the HRSI_{WV1} for shrub and tree cover, and then manually selecting only those GLAS footprints that were free of such vegetation. The *Forest* sites were 10 m radius circles centered on those GLAS footprints for which *in-situ* field data was collected in forest plots. The ground surface elevation from HRSI_{WV1} DSMs was calculated as the minimum value of all DSM pixels within a plot (dsm_{\min}).

Second, we examined the relationship of spatially coincident measurements of maximum canopy height from field plots to those derived from spaceborne estimates (a combination of HRSI_{WV1} DSM and GLAS data). To do this we (1) computed spaceborne estimates of maximum canopy height at the plot scale and paired them with the height of the tallest tree (maximum tree height) of the coincident field plot; (2) filtered this set of paired field and spaceborne data to exclude those spaceborne estimates that did not meet thresholds for spaceborne data quality for short stature forest stands; and (3) computed a linear

model of the relationship and performed statistical bootstrapping of the R^2 and root mean square error (RMSE).

To compute spaceborne estimates of maximum canopy height at the plot scale, spatially coincident DSM pixel values and GLAS metrics were examined for each field plot. Field plots were represented by 10 m radius circles, centered on GLAS footprints, which corresponded to the size of the majority of plots established in the field. Based on the size of each circle and the spatial resolution of the DSMs, there were ~2000 DSM pixels that were entirely within the boundary of a corresponding GLAS footprint-centered, 10 m radius circle representing the field plot. Summary statistics were compiled from the set of pixels corresponding to each circle to provide an estimate of maximum canopy surface elevation (dsm_{max} : the maximum value of the plot's pixels) as well as potential ground surface elevation (dsm_{min} : the minimum value of the plot's pixels). The final ground elevation ($elev_{ground}$) was determined from the minimum of the GLAS metrics $elev_1$, $elev_2$, along with the DSM-derived dsm_{min} . Spaceborne maximum canopy height for each plot was then calculated by subtracting $elev_{ground}$ from dsm_{max} . These spaceborne estimates were linked to the corresponding maximum tree height values of all trees of a given field plot.

The set of field plots used were filtered according to two conditions. The final set of field plots were those for which; (1) the coincident $HRSI_{wv1}$ data had stereo pair convergence angles >35 degrees; and (2) the coincident GLAS waveform offset distance from signal beginning to end ($wflen$) <16 m (G. Sun, Ranson, Kimes, Blair, & Kovacs, 2008b). These conditions were used to reduce the effect of feature height errors associated with low convergence angles (M. A. Aguilar et al., 2014; R. Li et al., 2007; 2009), slope and cloud contamination on the comparison of field- and spaceborne-derived heights. The remaining plots featured a set of trees 97% of which were less than 10 m in height.

Linear regression was used to model the relationship of the field plot and spaceborne maximum canopy height measurements. With this model, field-derived canopy height was the dependent variable to conform to the approach of using spaceborne measurements to predict those that are ground-based. The fit and uncertainty of this model was quantified using model bootstrapping. This produced a distribution for the model's R^2 and root moon square error (RMSE) by repeated sampling (with replacement) of the data.

4.4. Results

The histogram in Figure 4-2 shows stem density for trees in the 33 forested field plots that remained available for analysis after data filtering. It explains the range of trees (>3 cm DBH) per hectare for these forested plots centered on GLAS footprints that remained after HRSI_{wv1} DSM convergence angle and GLAS *wflen* thresholds were applied. At these 33 plots, 410 trees (*Larix sp.*) were surveyed for DBH and height. The heights of 400 trees were measured with clinometers and those of the remaining 10 directly with standard tape measurements.

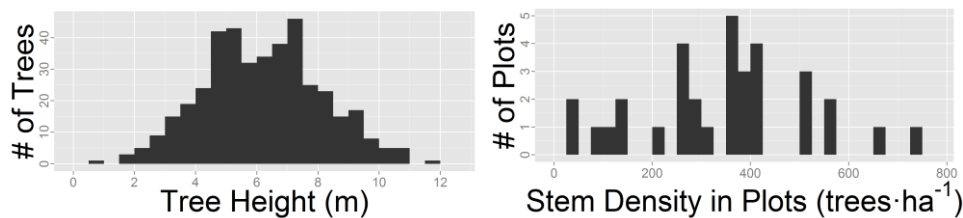


Figure 4-2. Histograms showing the distribution of field measured tree heights (Left) and the stem density of trees (Right) for trees >3 cm DBH in the 33 forested field plots centered on GLAS footprints.

The relative difference between GLAS and HRSI_{wv1} DSM ground elevation measurements was examined using 355 GLAS footprints in *Non-Forest* (tundra) sites and 73 in *Forest* sites in northern Siberia (Figure 4-3). The model comparing the two ground elevation measurements in both *Non-Forest* and *Forest* shows a close 1-to-1 fit across the ~350 and ~300 m elevation ranges (slope = 1, $p < 0.001$). The DSM and GLAS measurements have a difference in bias between *Non-Forest* (y-intercept = -1.3 m, $p < 0.001$) and *Forest* locations (y-intercept = -4.1 m, $p < 0.01$) of 2.8 m. The bootstrapped root mean square difference (RMSD) of ground elevations from the *Non-Forest* model had a 95% confidence interval (CI) of ±0.90 m–1.06 m while that of the *Forest* model was ±2.26 m–3.40 m. These GLAS ground elevation results for *Non-Forest* are similar to those of recent studies that examined ground elevation retrieval from GLAS (Popescu et al., 2011; G. Sun, Ranson, Kimes, Blair, & Kovacs, 2008b).

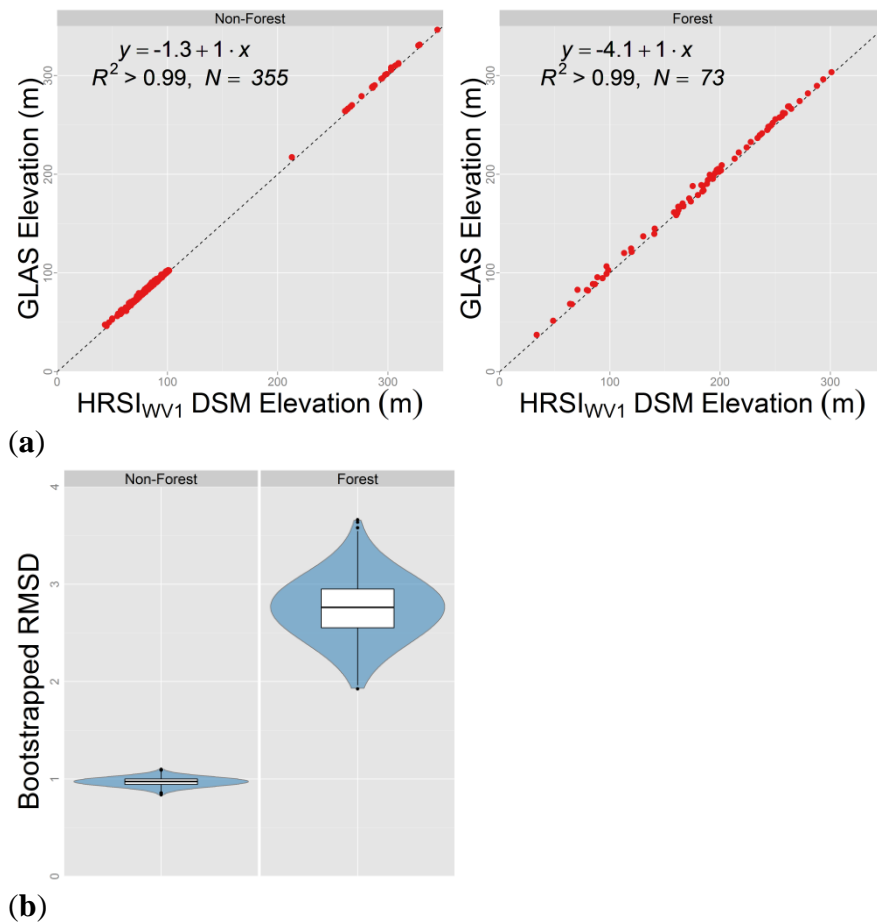


Figure 4-3. (a) The relationship of ground surface elevation measurements from GLAS and HRSI_{WV1} DSMs in *Non-Forest* and *Forest* cover types. The 1-to-1 line (dotted) is shown for reference; (b) The distributions of the bootstrapped model RMSD in ground elevation measurements from GLAS and HRSI_{WV1} DSMs in *Non-Forest* (0.90 m–1.06 m, 95% CI) and *Forest* (2.26 m–3.40 m, 95% CI) cover types.

The linear model for predicting plot maximum canopy height is reported in Figure 4-4a (model coefficients' $p < 0.001$). Figure 4-4b depicts the bootstrapped R^2 and RMSE distributions of the model in 4a. This model corrects for the spaceborne measurements underestimating heights less than 10 m, particularly heights < 5 m. The bootstrapped RMSE ranged from 0.86 m to 1.37 m at the 95% confidence level. This error was based on a mean bootstrapped R^2 of 0.55, which ranged from 0.36 to 0.74 at the 95% confidence level. The histograms in Figure 4-5 show the distributions of maximum heights from both the

field and the spaceborne measurements. Maximum plot heights measured in the field range from ~5 m to ~12 m. Those derived from spaceborne measurements ranged from ~1 m to ~12 m.

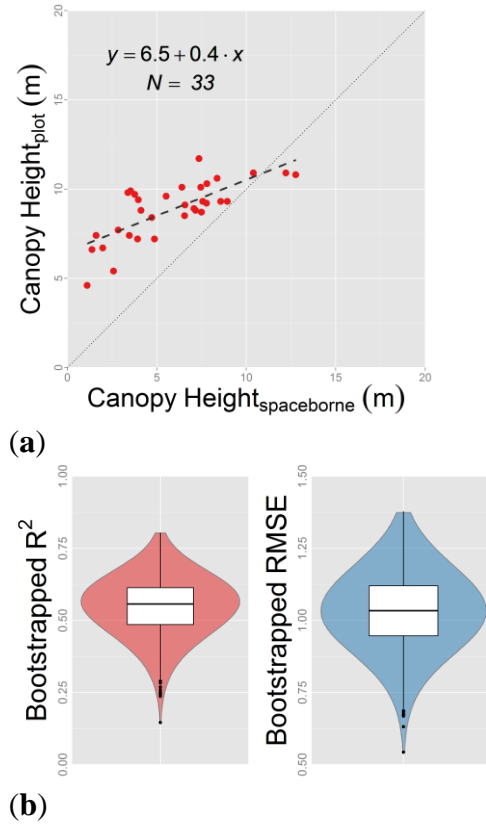


Figure 4-4. (a) The plot showing the linear model for predicting plot-scale maximum canopy height from spaceborne canopy height. The 1-to-1 line (dotted) is shown for reference; (b) the distributions of the bootstrapped R^2 and RMSE for the canopy height linear model in (a).

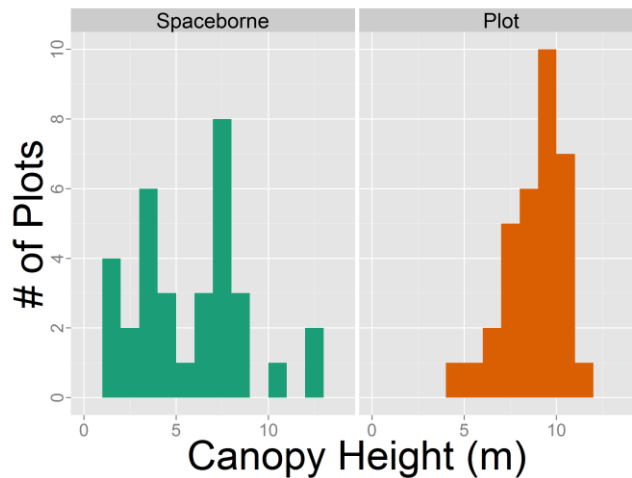


Figure 4-5. Histograms of the distributions of spaceborne- and plot-derived maximum canopy height at the scale of an individual field plot.

4.5. Discussion

4.5.1. Spaceborne Canopy Height and Its Sources of Uncertainty

This analysis coupled a comparison of measurements of ground surface elevations from two satellites with a comparison of field- and spaceborne-derived canopy height estimates. The analysis of ground surface elevation shows that GLAS data provides consistently lower elevation measurements than those of coincident HRSI_{WV1} DSMs for *Non-Forest*, and in particular *Forest*, sites. This supports the technique of combining coincident GLAS ground surface elevations with HRSI_{WV1} DSM canopy surface elevations to derive spaceborne estimates of canopy height. The DSMs provide an estimate of canopy surface elevation in this study, where GLAS is mostly insensitive to the subtle structural signals of sparse forest cover. The DSMs are less reliable for providing the lowest ground surface elevation, so for this measurement, the ground surface elevation is best determined as the minimum value of both GLAS and DSM elevations. This combined use of spaceborne data was used to compute spaceborne canopy height estimates in sparse forest cover. The canopy height analysis indicates that GLAS and HRSI_{W1} DSMs predict field plot estimates of maximum canopy height in the sparsely forested stands of the taiga-tundra ecotone with an uncertainty range of ± 0.86 – 1.37 m at the plot-scale (~ 314 – 707 m²). However, these estimates are based on only a moderate model fit.

The canopy height model is noisy and the relationship suggests a bias from spaceborne maximum canopy heights. This bias arises from the apparent tendency of this combination of satellite data to underestimate plot-derived maximum plot heights < 10 m. This underestimation could be due to either or both of the following, (1) an overestimation of ground surface elevation or (2) an underestimation of canopy surface elevation. We believe it is the latter for two reasons. The first reason is that the use of GLAS ground elevation provides a lower elevation relative to the DSM (Figure 4-3), decreasing the likelihood of ground elevation overestimation, particularly in sparse forests. Second, this underestimation of maximum height is similar to the bias seen in both waveform and small footprint LiDAR, and may occur

because the tops of trees are either not resolved or detected, and the remote measurement is likely coming from lower in the canopy (Peterson, Nelson, & Wylie, 2013; Wasser, Day, Chasmer, & Taylor, 2013b). For sparse *Larix* forest stands, the difficulty in resolving the top of trees is not surprising, given the relatively small canopy area of the mature growth forms found in northern Siberia. Thus, model uncertainty may also be related to maximum tree heights in plots not sufficiently representing that which the spaceborne data reflects. Finally, while efforts were made to align field plots with HRSI_{WV1} DSM data, compounded horizontal geo-location errors among field plots and DSM pixels can influence model fit and uncertainty. Thus, the magnitude of error from plot-scale spaceborne canopy height is particularly sensitive to data at finer scales (Frazer et al., 2011). This increases the difficulty of reducing uncertainty at the plot-scale across broad regions, as trade-offs between the size of plots and the number of plots surveyed are usually made during expensive and time consuming field expeditions. Gaps between field and HRSI_{WV1} data (~4 years) are not expected to be significant sources of error given the age and relatively slow growth of trees in this area (Kajimoto et al., 2009; V. Kharuk et al., 2013b; Osawa & Kajimoto, 2009).

The lower RMSD between ground elevation from GLAS and HRSI_{WV1} DSMs at *Non-Forest* sites relative to *Forest* sites suggests the contribution of GLAS ground elevation to canopy height estimates is an improvement on those from stereo photogrammetry alone. However, an analysis solely focused on this difference was not performed. Stereo photogrammetric estimates of ground elevation estimates within forested areas are highly uncertain (H. Raggam, Franke, Ofner, & Gutjahr, 2005; Vepakomma, St-Onge, & Kneeshaw, 2011). The use of GLAS as a means of achieving reliable ground surface elevation measurements, particularly in sparse forests, is a novel technique which can potentially decrease the uncertainty of millions of TTE vegetation height estimates at the plot-scale when complemented with HRSI DSMs, without the use of airborne data. The trade-off, however, is that canopy height from this method is available as samples coincident with GLAS footprints rather than as a continuous map variable across the extent of the HRSI field of view.

The model can be applied to all GLAS footprints with coincident DSMs in *Larix* stands to estimate stand height. However, the model was built from 33 field plots and the limited sample size is in part responsible for the broad uncertainty of the model fit (the distribution of the bootstrapped R^2 at the 95% confidence level). The inherent drawback for modeling *Larix* stand height is that uncertainty estimates are less robust with lower R^2 . The model error is similar to other reported canopy height model errors from high-resolution spaceborne imagery (Huaguo & Biao, 2011), although the model in this study was built from sparse and short stature *Larix*, primarily between 5 and 10 m in height. Most of the available field plot data collected in Siberian *Larix* stands were not used because coincident DSMs were not available at the time of the analysis. However, as more DSMs become available, the model can be updated to provide a more robust estimate of the stand height uncertainty from spaceborne remote sensing at the plot-scale.

4.5.2. Future Work

There is a unique need for high resolution spaceborne estimates of vegetation structure across the taiga-tundra ecotone, and in Siberia, in particular. This need is driven by the importance of TTE vegetation on regional and global climate, its propensity for change, the subtle yet relevant signal of its vegetation, and the difficulty of collecting field and airborne data. Existing global level estimates of vegetation height, suited for depicting average landscape-scale attributes, are likely to be too coarse and uncertain for monitoring site-specific and spatially variable changes in the sparse forests of the TTE that have been expected and documented (Hofgaard et al., 2012; F.-K. Holtmeier & Broll, 2005; V. I. Kharuk et al., 2006; Naurzbaev, Hughes, & Vaganov, 2004).

This study's technique provides an opportunity to examine detailed vegetation structure in sparse forests across broad extents in regions difficult to assess through field and airborne survey. Applying this model across thousands of forested GLAS footprints with coincident DSMs in northern Siberia is a potential next step for examining uncertainty in spaceborne-derived forest structure across a TTE landscape. These empirically derived sample heights can be averaged according to forest patches,

attributing the two-dimensional patches with statistical estimates of vertical forest structure and its uncertainty. This scaling-up to forest patch-level estimates of canopy height and its uncertainty can then be empirically related to coarser remote sensing data (ASTER, Landsat, ALOS PALSAR) to extend patch-level estimates of canopy height and its uncertainty across regions. This potential for extending estimates across remote regions is enabled through the automated processing of DSMs (without the use of ground control points). While height estimates from DSMs can be improved with ground control, these data are typically not available in remote areas and not practical to apply when processing large volumes of data across broad extents.

The way in which satellite estimates of sparse and short stature forest canopy height may change with DSMs derived from other image pairs was not tested. Such an endeavor would involve analyzing repeated stereo pair DSM measurements at each plot. With this approach, a study could examine the effects of a number of variables on the uncertainty of canopy height estimates for a continuum of forest stand structural arrangements (sparse and short, sparse and tall, dense and short, dense and tall). These variables would include seasonality, satellite geometry, snow cover/depth, and slope/aspect. Furthermore, repeated DSM measurements add vegetation height information, building a distribution of height measurements at a given location. This will help refine spaceborne canopy height measurements, by reducing uncertainty and revealing the fundamental bias (assuming one in fact exists) associated with TTE canopy surface measurements from HRSI DSMs. The opportunity for high-resolution monitoring of the TTE is growing. The archives of existing GLAS along with increasing HRSI stereo coverage (used to derive DSMs) will continue to add complementary pieces of information on TTE vegetation structure, particularly forest height. The launch of NASA's ICESat-2 satellite will add measurements of vegetation height and ground elevation to existing datasets, and will increase the spatial and temporal sampling of TTE vegetation structure. While significant uncertainties may exist from TTE vegetation structure estimates derived from ICESat-2 data alone, photon-counting LiDAR measurements in tandem with other datasets may help reduce measurement uncertainty of forest characteristics at critical scales.

4.6. Conclusions

At the plot-scale in northern Siberia *Larix* forests, complementary measurements from GLAS and HRSI_{WV1} DSMs can produce canopy height estimates in sparse TTE stands primarily <10 m in height. These TTE stand measurements combine archival ground elevation from GLAS and current canopy surface elevation from HRSI stereo image pairs. With a linear model, spaceborne canopy height predicted these TTE stand heights, between ~5 m and ~10 m tall, with an R^2 of 0.55 (0.36–0.74, 95% CI) and an uncertainty ranging from ± 0.86 to 1.37 m.

This study provides a means for directly measuring TTE forest height from a combination of LiDAR and multispectral spaceborne sensors. This uncertainty of these height estimates in TTE stands can be better characterized by analyzing GLAS and HRSI DSMs across a broader range of sensor and target conditions. The use of HRSI DSMs compiled from image pairs whose satellite geometry minimize the uncertainty in height estimates for TTE stands will clarify the potential for plot-scale measurements of subtle vegetation structure signals from spaceborne data. Scaling up these plot-scale height and uncertainty measurements to the forest patch scale will allow these estimates to be spatially continuous, rather than limited to GLAS footprint samples.

Chapter 5: Spaceborne Potential for Examining Taiga-Tundra Ecotone Form and Vulnerability

5.1. Abstract

In the taiga-tundra ecotone (TTE), vegetation structure change can be subtle and site-dependent, yet occur across the circumpolar region. This asynchronous change may be related to the horizontal and vertical patterns of vegetation structure such as tree density and height within TTE forest patches (i.e., ecotone form) that is driven by local site conditions and linked to ecotone dynamics. The unique circumstance of subtle, variable and widespread vegetation change warrants the application of spaceborne data including high-resolution (<5m) spaceborne imagery (HRSI) across broad scales for examining TTE form and predicting dynamics.

Recent work demonstrates the fundamental uncertainty of spaceborne-derived forest biomass density and height estimates in sparse boreal forests at the plot-scale. Patch-scale analyses of forest structure in the TTE provide a means to examine both vertical and horizontal components of ecotone form, their association with landscape characteristics and environmental factors, and a basis for examining the variation of patch characteristics across sites. In this study we demonstrate the potential of spaceborne data for integrating forest height and density information to assess TTE form. We map forest patches in study sites along the TTE in northern Siberia with HRSI and attribute patches with tree cover and spectral data from Landsat 7, backscatter power from ALOS PALSAR and canopy height data based on a HRSI-derived digital surface model and ICESat-GLAS ground elevation, and HRSI-derived surface roughness. We examine the uncertainty of forest patch height from this suite of spaceborne data across ecotone sites of primarily diffuse TTE forms.

Spaceborne data provides a circumpolar potential for consistent analysis of TTE form. Results demonstrate the opportunities for improving patch-scale spaceborne estimates of forest height, the vertical

component of TTE form. The distribution of relative maximum height uncertainty based on prediction intervals is centered at ~40%. We discuss this uncertainty in light of a conceptual model of general ecotone forms. We highlight how the uncertainty of spaceborne estimates of height can contribute to the uncertainty in identifying TTE forms. A focus on reducing height estimates of forest patches may improve depiction of TTE form, which may help explain variable forest responses in the TTE to climate change and the vulnerability of portions of the TTE to forest structure change.

5.2. Introduction

5.2.1. The Structure of Vegetation in the TTE

The transition from continuous forest, to forest patches, to continuous tundra defines the transition zone between boreal forest and tundra, also known as the tree-line or the taiga-tundra ecotone (TTE). The location, extent, and vegetation structure and patterns of the TTE influence interactions between the biosphere and the atmosphere through changes to the surface energy balance and distribution of carbon (Bonan, 2008; Callaghan, Werkman, & Crawford, 2002b). These TTE vegetation characteristics also affect local and regional arctic and sub-arctic biodiversity (Hofgaard et al., 2012). The vegetation structure and patterns of the TTE are controlled by a variety of factors that are scale-dependent (F.-K. Holtmeier & Broll, 2005). At local scales the spatial configuration of trees is determined largely by site-level heterogeneity in hydrology, disturbance, topography (aspect, slope, elevation), land use and the geomorphologic conditions associated with each (Dalen & Hofgaard, 2005; Danby & Hik, 2007; Frost, Epstein, & Walker, 2014; Haugo, Halpern, & Bakker, 2011; K.-F. Holtmeier & Broll, 2010).

5.2.2. Influence of TTE Structure on Dynamics

In north-central Siberia, where the TTE exhibits a latitudinally defined gradient of tree cover from south to north, TTE forest cover characteristics include a general decrease in height and cover and a variety of spatial patterns (K.-F. Holtmeier & Broll, 2010). These structural characteristics influence TTE dynamics. Dufour-Tremblay et al. (2012) note that rapid growth changes forms, thus altering recruitment

dynamics (Dufour-Tremblay, Lévesque, & Boudreau, 2012). Loranty et al. (2013) discuss the vegetation controls on the snow-albedo feedback in the arctic (Loranty et al., 2013). D'Odorico et al. (2012) explain that the height and canopy cover of trees and shrubs affect site-level radiative cooling, whereby larger canopies increase nocturnal warming and influence regeneration (D'Odorico et al., 2012). Such tree height and canopy controls over the transmission of solar energy have been well documented (Davis et al., 1997; Hardy, Davis, Jordan, Ni, & Woodcock, 1998; Wenge Ni, Li, Woodcock, Roujean, & Davis, 1997; Y. Zhang, 2004). Vegetation height also influences permafrost, whereby taiga patches trap snow and lower permafrost temperatures (Roy-Léveillé, Burn, & McDonald, 2014). Ni-Miester et al. (2011) note the importance of accounting for vegetation heterogeneity in schemes addressing surface radiation dynamics because of the effects on rates of snowmelt in the boreal (Ni-Meister & Gao, 2011). A modeling study by Ni and Woodcock (2000) supports the importance of tree heights on boreal forest albedo, which is a function of canopy structure, the snow regime, and the angular distribution of irradiance (Wenge Ni & Woodcock, 2000). Bonfils et al. (2012) explain that better representation of vegetation height and cover are needed to improve climate prediction in the high northern latitudes (Bonfils et al., 2012).

5.2.3. A TTE Conceptual Model

Forest ecotones are a form of self-organizing system because there are feedbacks between the spatial patterns of groups of trees and ecological processes (Bekker, 2005; Malanson, Zeng, & Walsh, 2006). The patterns and structural characteristics of TTE forest patches have been conceptualized with a few general and globally recognized ecotone forms (M. A. Harsch & Bader, 2011; K.-F. Holtmeier & Broll, 2010). In the TTE, these general ecotone forms (diffuse, abrupt, island, krummholz) reflect the spatial patterns of forest patches and tree structural characteristics, and have different primary mechanisms controlling tree growth. The variation in ecotone form may help explain regional asynchronicity of TTE forest change because these forms are linked to site factors, the variation in which may in part control the heterogeneity of change seen across the circumpolar TTE (M. A. Harsch & Bader,

2011; Lloyd, Rupp, Fastie, & Starfield, 2002). Further investigation is needed into the link between observed changes in vegetation and local factors that may control these changes (Virtanen et al., 2010).

5.2.4. The Scale of TTE Observation

In the TTE, fine-scale data that resolves individual trees and groups of trees, may help reveal ecotone forms (Danby & Hik, 2007; Hansen-Bristow & Ives, 1985; Hofgaard et al., 2012; Hofgaard, Dalen, & Hytteborn, 2009; K.-F. Holtmeier & Broll, 2010; Mathisen, Mikheeva, Tutubalina, Aune, & Hofgaard, 2013). Without resolving groups of individual trees, coarse studies of the land surface may misrepresent ecotone form, be less frequently corroborated with ground data, and disguise the structural heterogeneity of sparse forests. In a TTE landscape this structural heterogeneity is critical for understanding biodiversity, and biogeochemical and biophysical characteristics such as carbon sources, sinks and fluxes, permafrost dynamics, surface roughness, albedo, and evapotranspiration (Bonan, 2008). Furthermore, understanding at a fine-scale where the TTE is likely to change may improve understanding of the potential effects of changing TTE structure on these regional and global processes.

5.2.5. The Uncertainty of Spaceborne Data of TTE Structure

Spaceborne remote sensing may facilitate linking TTE form with vegetation change and local site factors (Callaghan et al., 2010; Callaghan, Werkman, & Crawford, 2002b; M. A. Harsch & Bader, 2011; Kent, Gill, Weaver, & Armitage, 1997). However, a spaceborne assessment of forest structure from single active sensors across a gradient of boreal forest structure shows broad ranges of uncertainty at plot-scales (Montesano, Nelson, Dubayah, Sun, Cook, et al., 2014a; Montesano et al., 2015). A spaceborne remote sensing approach that identifies forest patches may provide insight into structural characteristics of forest patches that are indicative of these general ecotone forms at scales that are dictated by the homogeneity of forest structure itself. A patch-based approach to understanding forest height and forest height uncertainty in the ecotone acknowledges the influence that horizontal structure may have on the uncertainty of vertical structure measurements from remote sensing. Remote sensing from high resolution spaceborne imagery (HRSI) coupled with spaceborne LiDAR and medium spatial resolution

(5m-50m) sensors can provide consistent observations to evaluate patch characteristics and may provide insight into local-scale ecotone form across the broader circumpolar domain.

5.2.6. Patch-based TTE Analysis

The patch-based approach of remotely measuring TTE forest structure addresses the imperative for site-scale detail of TTE vegetation, whereby individual trees can be resolved, while acknowledging the influence of clusters of trees (patches) and their density on TTE attributes and dynamics. This approach is a way of coarsening data, reducing spatial detail. However, from a biogeographic perspective, this reduction in detail is not arbitrary as are image pixel reductions when images are coarsened by means of down-sampling. Rather, image features and ancillary datasets inform the coarsening procedure, creating patch boundaries that are based on spectral and textural characteristics of images as well as other landscape information. Polygonal patches, particularly when vegetation patterns and heterogeneity are key landscape features, may be more informative than pixels particularly for studies at fine scales. Furthermore, patches provide a means to integrate remote sensing data across an area and extend sample measurements (Kellndorfer et al., 2010; M. A. Lefsky, 2010; Montesano et al., 2013; van Aardt, Wynne, & Oderwald, 2006; Wulder & Seemann, 2003; Wulder et al., 2007).

5.2.7. Towards Identifying TTE Form: Remote Sensing Data Integration and Scaling

The integration of remote sensing data across patches helps address issues data scaling issues. First, medium-resolution sensors such as Landsat and ALOS may not be suited for identifying the horizontal patch structure at the resolution required to study TTE structure, however, their spectral or backscatter information may still have value for predicting patch characteristics. Using the spatial detail of the HRSI to define patch boundaries helps integrate coarser data into an analysis while maintaining the spatial fidelity of patches. Second, patch-level analysis helps attenuate high frequency noise. For example, ALOS PALSAR backscatter has significant pixel-level speckle (Le Toan et al., 2011; Mette, Papathanassiou, & Hajnsek, 2004; Shamsoddini & Trinder, 2012) which, when grouped with coincident HRSI patch boundaries, can be averaged to reduce this high frequency noise.

A long term goal for monitoring vegetation in the TTE is to not only evaluate the magnitude of change over time and between sites, but also to separate portions of the TTE that are vulnerable to changes in structure (i.e. changes in height, canopy cover, tree density) from those whose structure is more resilient, and the rates associated with these changes (Epstein et al., 2004). The spatial patterns of this structural vulnerability will help gap models predict the consequences of TTE structure change on regional and global processes. The short term goal addressed in this study is to examine the uncertainty of mapped forest patch heights using spaceborne remote sensing data integration and to discuss the implication of this uncertainty for both identifying TTE form and predicting dynamics, with regard to separating vulnerable from resilient TTE structure regimes.

5.3. Methods

5.3.1. Study Area

We visually interpreted HRSI to identify sites in northern Siberia within the TTE where forest cover was sparse and where forest patches exhibited diffuse, abrupt or island ecotone patch forms. The sites are primarily situated on the Kheta-Khatanga Plain, north of the Kheta River, which is a tributary of the Khatanga River flowing north into the Laptev Sea. One site, which sits just south of the Novaya River on the Taymyr Peninsula, includes a portion of Ary-Mas, the world's northernmost forest (Bondarev, 1997; V. Kharuk, Ranson, & Dvinskaya, 2007; Naurzbaev & Vaganov, 2000).

The region is subject to a severe continental climate, generally exhibits a sparse gradient in tree cover, features elevations generally < 50 m.a.s.l., and is underlain with continuous permafrost (Bondarev, 1997; Naurzbaev et al., 2004). The forest cover, exclusively *Larix gmelini*, exists at the climatic limit of forest vegetation, coinciding closely with the July 10°C isotherm (Osawa & Kajimoto, 2009). Sites were chosen based on the presence of cloud-free multispectral and stereo pair data from HRSI available in the Digital Globe archive, and patches of forest cover (Neigh, Masek, & Nickeson, 2013a). The geographic footprints of all sites for which forest patches were examined are shown in Figure 5-1. Individual tree measurements at circular plots coincident with ICESat-GLAS LiDAR footprints were collected during an

August 2008 expedition to the south of this study area, along the Kotuykan River, and were used as either calibration or validation data in this study (Montesano, Sun, Dubayah, & Ranson, 2014b).

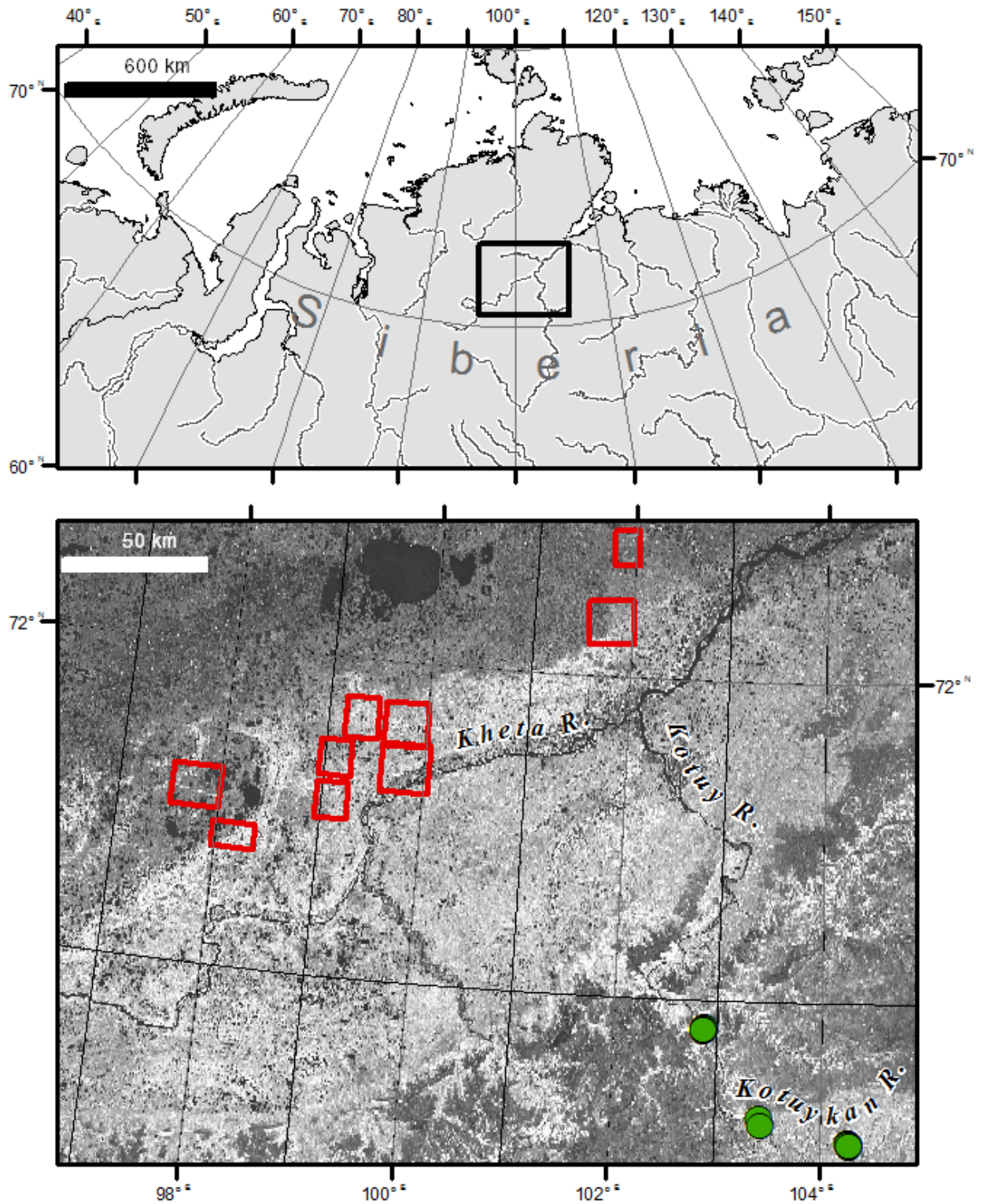


Figure 5-1. Study area in northern Siberia showing the 9 sites for which forest patches were examined (red boxes) and the field sites along the Kotuykan River (green dots) at which individual tree height measurements in circular plots coincident with ICESat-GLAS LiDAR footprints were collected.

5.3.2. Remote Sensing Data Acquisition and Processing

A variety of spaceborne remote sensing datasets were used in this study to delineate and attribute forest patches and predict forest patch height. Table 5-1 lists the individual data sets along with their period of acquisition. These data were collected within ~8 year period (2004 - 2012) across sites for which, based on visual inspection of HRSI, there were no signs of disturbance from fires, and for which the rate of tree growth is well below that which would be detectable from spaceborne data in that time interval. The data include passive optical derived from Landsat-7 ETM and Worldview-1 & -2, synthetic aperture radar (SAR) from ALOS PALSAR, and light detection and ranging (LiDAR) data from the ICESat satellite's Geoscience Laser Altimeter System (GLAS). All data were compiled and processed in a geographic information system (GIS) to maintain the critical association of coincident geographic characteristics from one layer to the next.

Data were primarily images covering the full extent of each study site that were all resampled from their original un-projected format during a re-projection into the Universal Transverse Mercator coordinate system (Zone 48). The images were either medium (25m-30m pixels) or high (<5m pixels) resolution. The medium resolution spaceborne imagery included the Landsat multispectral composite and vegetation continuous fields tree cover (VCF) products described in Hansen et al (2013) and ALOS PALSAR tiled yearly mosaics (2007 - 2010) (Hansen et al., 2013; Shimada et al., 2014). The four ALOS PALSAR yearly mosaics were processed into an average temporal mosaic of dual polarization (HH and HV) backscatter power. The high resolution data consisted of HRSI multispectral (Worldview-2 satellite) and panchromatic (Worldview-1 satellite) data acquired from the National Geospatial Intelligence Agency through an agreement with the US Government (Neigh, Masek, & Nickeson, 2013a).

The LiDAR data from ICESat-GLAS featured ground footprint samples of binned elevation returns of features within each footprint. These LiDAR data provided ground surface elevation samples

as described in Montesano et al. (2014). The set of GLAS data coincident with the digital surface model (DSM) of the study sites were filtered in an effort to remove LiDAR footprints for which within-footprint elevation changes precluded capturing heights of trees generally less than 12m tall. GLAS footprints used satisfied the following conditions; (1) the set of coincident DSM pixels had a standard deviation $\leq 5m$, (2) the length of the LiDAR waveform $\leq 20m$, and (3) the difference between the maximum and minimum DSM values within a 10m radius of the GLAS LiDAR centroid was $\leq 25m$.

Table 5-1. Summary of datasets used to delineate or attribute forest patches.

Dataset	Date	Attribute	Scale
Landsat-7 cloud-free composite, continuous fields of tree cover	circa 2013	Top-of-atmosphere reflectance (SWIR, NIR, red, green); tree cover	30m pixel
HRSI: WorldView 1 & 2	circa 2012	DSM, NDVI, roughness, CRM	~ 0.5m - 2m pixel
ALOS PALSAR composite	2007-2010	backscatter power (HH, HV)	25m pixel
ICESat-GLAS LiDAR	2003-2006	ground surface elevation, waveform length	~60m diameter footprint

This HRSI was processed in accordance with Montesano et al. (2014) to generate a DSM for each study site. In addition to DSM production, the HRSI data were processed to compute three other image layers that were used to delineate and attribute forest patches with the mean and variance of corresponding image pixel values. First, a normalized difference vegetation index (NDVI) layer was computed to create a mask separating areas of vegetation from non-vegetation within the HRSI. This algorithm, widely used in for terrestrial remote sensing science, was based on the near-infrared (NIR) and red channels of the multispectral HRSI $((NIR-Red) / (NIR+Red))$. Second, the first of two image roughness datasets was derived for each site. This roughness data was based on the textural characteristics of each site's panchromatic HRSI and was computed using the output layers from the

bright and dark edge detection (described in Steps 10-12 of Table 2 in Johansen et al.) (Johansen et al., 2014). The result was a single image layer showing increased brightness values corresponding to increasingly textured surface features. This layer was used within the vegetation mask, creating a forest mask sub-category. At this point, forest was separated from non-forest based on a panchromatic HRSI roughness threshold value = 5.5, where higher values represented rougher vegetation and were classified as forest. Next, the second of two image roughness layers, a canopy roughness model (CRM), was calculated from each DSM. A low pass (averaging) filter (kernel size = 25 x 25) was applied to a version of the DSM that was coarsened by a factor of 8. The filtering generated a smoothed estimated terrain elevation ($elev_{terrain}$) layer that removed the elevation spikes from the sparse tree cover that is evident in the DSM. This $elev_{terrain}$ layer was then re-binned to the original pixel grid. Surface feature roughness was computed as the difference between the DSM and $elev_{terrain}$, and were represented as heights above $elev_{terrain}$. Pixels within the forest mask formed the CRM. The panchromatic-based roughness data along with the DSM-based CRM provided two HRSI-derived estimates of vegetation roughness. A CRM threshold value = 1 re-classified existing non-forest regions into the forest class. Finally, remaining non-forest areas with a mean roughness > 3 and mean NDVI < 0.25 was classified as forest.

5.3.3. Forest Patch Delineation and Attribution

We analyzed forest structure at the study sites first by delineating forest patch boundaries and attributing these patches with remotely sensed data in order to model forest patch height. This delineation and attribution framework used the segmentation algorithms in Definiens Developer 8.7. This framework modifies the multi-step, iterative segmentation and classification procedure discussed in previous work (Montesano et al., 2013). The central difference is that this approach uses exclusively data from HRSI to identify a vegetation mask, a subset of which is a forest mask, applies a segmentation to this forest mask to separate distinct forest patches, and then attributes those patches with the mean and standard deviation of pixel values from coincident HRSI, medium resolution Landsat and ALOS PALSAR, and GLAS LiDAR.

The procedure to separate distinct forest patches from within the forest mask involved 2 steps. First, this forest mask was divided to separate portion of forest whose roughness values were > 2 standard deviations above the median roughness value. Next, patches were broken apart according to surface elevation values provided from each site's DSM. Patches were attributed with the mean and standard deviation of image pixel values within the boundary of each patch. Those patches with a minimum size of 0.5 hectares were exported into a GIS to gather coincident LiDAR footprint samples of forest patch height (direct estimates) determined according to an existing approach discussed below.

5.3.4. Predicting Forest Patch Height Directly at LiDAR footprints

Spaceborne LiDAR sampling of forest canopy height provided a means to estimate average patch canopy height through direct spaceborne height measurements. Where forest patches coincide with GLAS footprints, the canopy surface elevation from the DSMs and the ground elevation from either the DSMs or GLAS within a GLAS footprint provide a sampling of forest height within the patch. First, we applied the methodology presented in Montesano et al. (2014) to compile spaceborne-derived canopy height within GLAS footprints and convert those heights to plot-scale maximum canopy height with a linear model. Finally, these plot-scale canopy height predictions from all GLAS footprints within a given patch were used to directly determine the mean predicted forest patch height and the mean height error from the prediction interval of the canopy height linear model.

5.3.5. Modeling Forest Patch Height Indirectly (without LiDAR Samples)

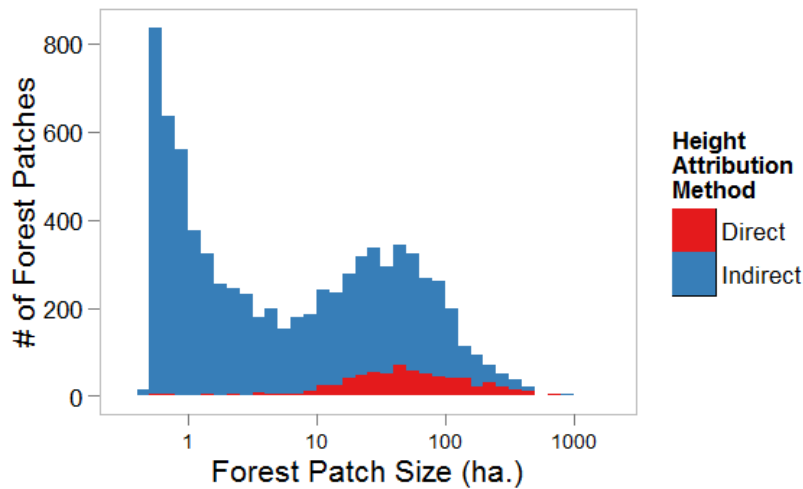
Canopy height predictions were made indirectly for forest patches without direct spaceborne sampling of forest canopy height. This indirect method, used for the vast majority (~90%) of forest patches > 0.5 ha across the study sites, involves (1) building a model from the set of forest patches with spaceborne LiDAR samples relating the predicted forest patch canopy height (response variable) to spaceborne image data (predictor variables) and (2) applying that model to predict forest patch canopy height for those patches with no direct spaceborne height samples. These methods, described in Montesano et al. 2013 and Kellndorfer et al. 2010, use the Random Forest regression tree approach for

prediction (Breiman, 2001). This approach includes specifying the both number of decision trees that are averaged to produce the random forest prediction and the number of randomly selected predictor variables used to determine each split in each regression tree. The result is a prediction model that is valid for the range of predictions on which the model was built and reduces overfitting, or, the degree to which the prediction model is applicable to only the specific set of input data.

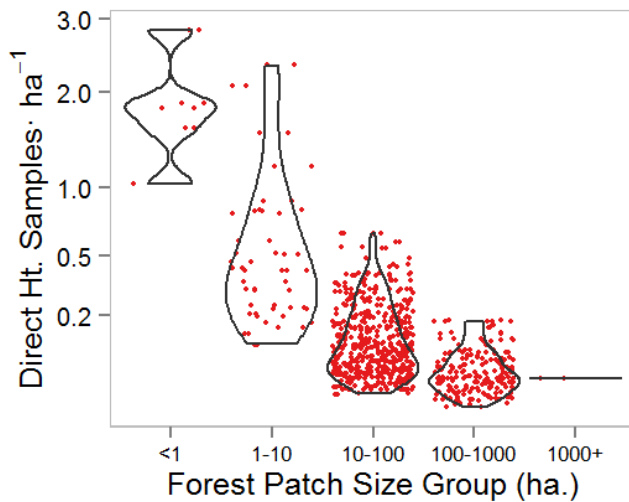
5.4. Results

5.4.1. Forest Patch Delineation and Direct Sample Density

Across the 9 study sites, 3931 forest patches were delineated based on *NDVI*, panchromatic texture and DSMs all from the HRSI data. Of this total, 364 patches (9%) coincided with at least one GLAS footprint at which a height sample was computed and used in the direct estimation of patch canopy height (Figure 5-2a). The bimodal distribution that features a peak in the number of forest patches ~1 ha in size is evidence of the heterogeneous nature of forest cover in this region. The violin plots in Figure 5-2b group forest patches, for which direct height estimates were made, into categories based on patch area. They show the general distribution of sampling density of direct height estimates within these patches. All patches with direct height samples featured a sampling density of < 3 samples ha^{-1} . The majority (94%) of sampled patches had sampling densities < 0.5 samples ha^{-1} , of which most had patch areas > 10 ha.



(a)



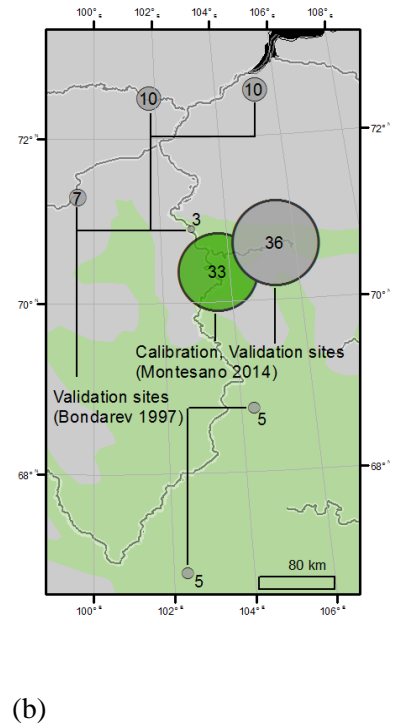
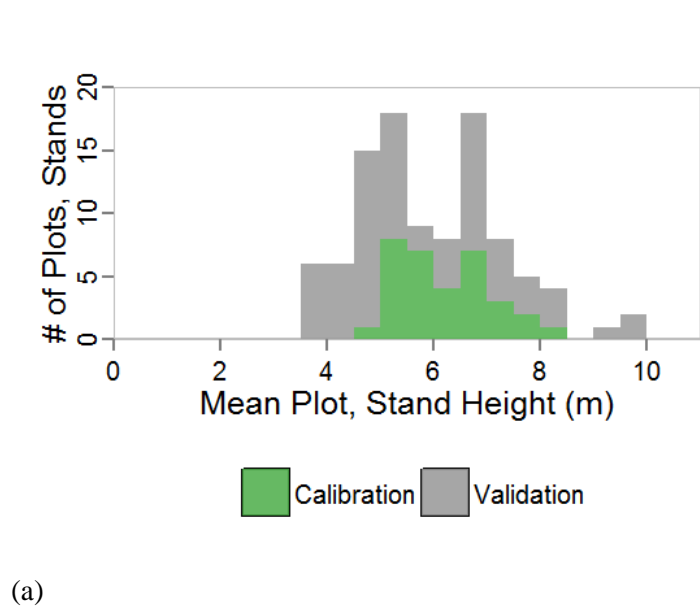
(b)

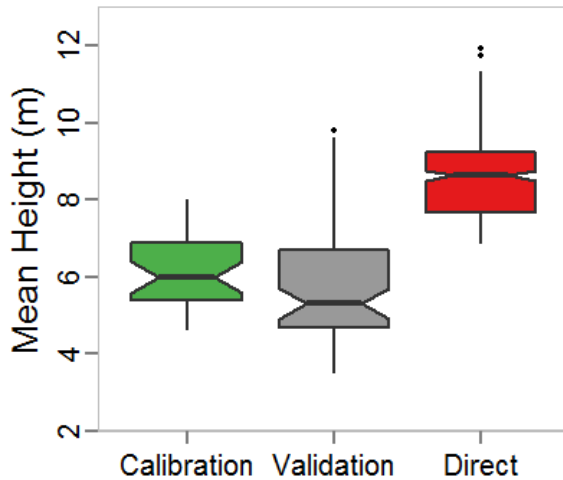
Figure 5-2. (a) The distributions of forest patch size in hectares according to height attribution method. (b) Violin plots, overlain with dots representing individual patches (red), of the distribution of direct height sample density for forest patch size group.

5.4.2. Comparison of Stand Height Calibration and Validation Data

Figure 5-3a shows the distributions of mean plot or stand height for measurements collected in plots along the Kotuykan River for this study ($n=69$) and those from regionally coincident stands ($n=40$) at 6 sites in northern Siberia from Bondarev (1997) (Figure 5-3b). A portion of the Kotuykan River plots were used to calibrate ($n=33$) the model used to estimate spaceborne canopy height at plot-scales after Montesano et al. (2014), which was applied in the direct estimation of forest patch height. The

remaining portion of the Kotuykan River plots (n=36) and stands from Bondarev (1997) (n=40) serve as independent validation of the distribution of forest patch heights derived from direct spaceborne height estimation. Mean heights of forest patches, plots, and stands are used to compare distributions of calibration and validation data because this was the height metric that was consistently available across the set of forest patches, the calibration plots and the validation plots and stands. The distributions in Figure 5-3c show the proportion of forest patch heights of those for which direct height estimates were made. This distribution of direct forest patch heights is shown alongside those individual tree measurements averaged across plots or stands from (1) the calibration plots in Montesano et al. (2014), (2) the remaining Kotuykan River validation plots, and (3) the validation stands from Bondarev et al. (Bondarev, 1997).





(c)

Figure 5-3. (a) Histogram of mean plot and stand heights from calibration and validation data. (b) Map of locations of calibration and validation sites in northern Siberia with the number of stands or plots associated with each site. The circles representing general site locations are sized according to the number of stands. (c) Notched boxplots showing the 25th, 50th, and 75th percentiles as horizontal lines and 1.5 times the inter-quartile range as vertical lines. Notches roughly indicate the 95% confidence interval for the median.

5.4.3. Indirect Forest Patch Height Estimates

Maximum and mean forest heights were predicted for 91% of forest patches across the study sites. Random Forest regression tree models for 5 sets of spaceborne data predictor variables were used to estimate maximum and mean patch height indirectly for patches with no coincident direct spaceborne height estimates. Figure 5-4 shows the residual standard error (RSE) and R^2 of the best performing model (based on R^2) for each spaceborne data predictor set (a particular combination of spaceborne data). The predictor set ‘All’ that included all spaceborne data layers (HRSI multispectral, HRSI panchromatic, HRSI DSMs & CSR, Landsat products, ALOS PALSAR mosaic) explained > 60% of overall variation in modeled patch height. This ‘All’ model shows only incremental improvement over the model using only HRSI-derived predictors. The Landsat & ALOS spaceborne variables explain < 40% of variation within the modeled relationship between spaceborne predictors and patch height.

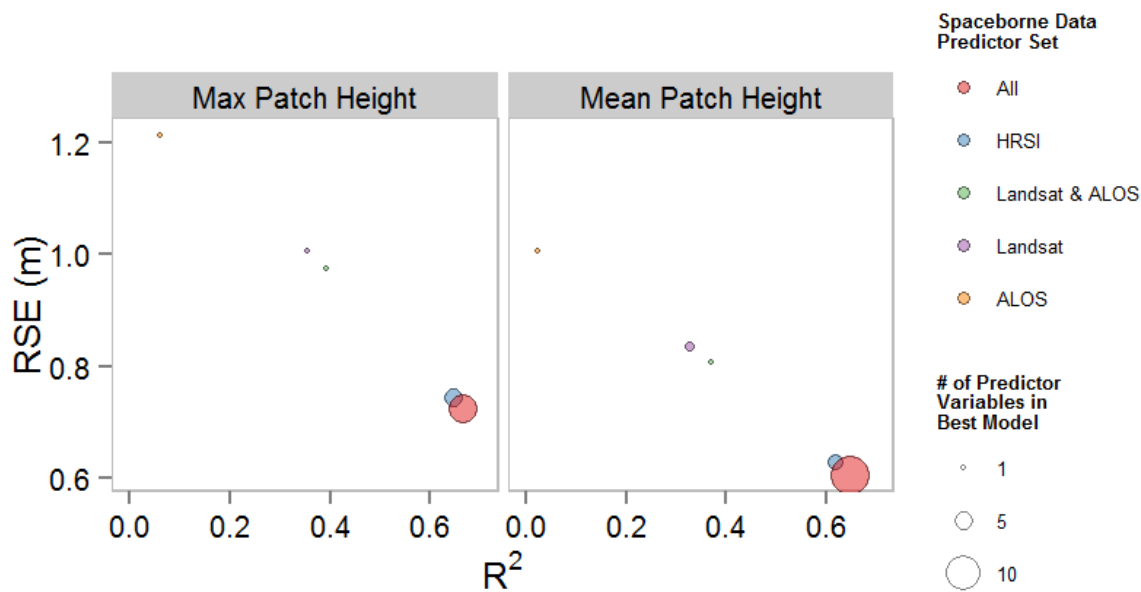
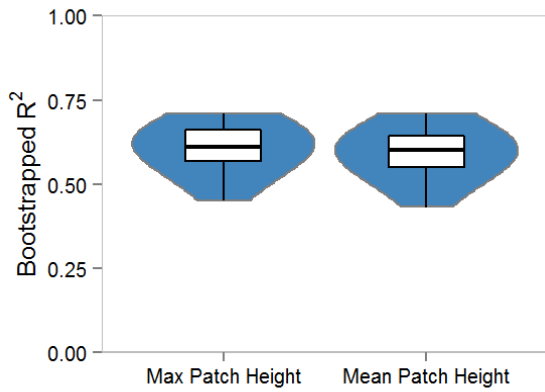


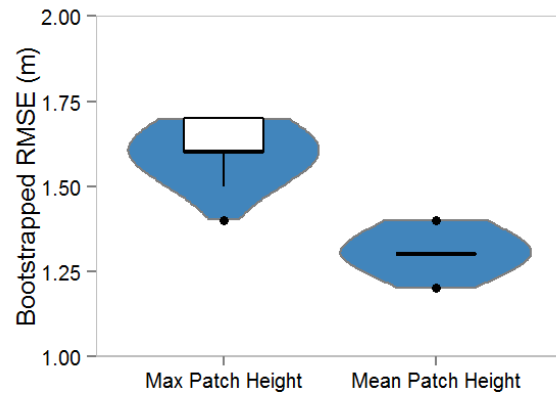
Figure 5-4. Results from Random Forest indirect forest patch height estimation for 5 spaceborne data predictor sets.

5.4.4. Uncertainty of Forest Patch Height Estimates

We assessed the best performing Random Forest model for indirectly estimating maximum and mean forest patch heights. The best performing models were those from the ‘All’ predictor sets, described above, where the number of predictor variables was 14 and 15, for maximum and mean forest patch height, respectively. Assessments were based on model R^2 and RMSE for the maximum and mean patch height models, where 50% of patches with direct height estimates from which the indirect models were built were used for model training and 50% were used for model testing. The results of a bootstrapping procedure to examine the distribution of R^2 and RMSE from the Random Forest models applied to the set of testing data is shown in Figure 5-5a ,b. The violin plots show the bootstrapped distributions of best performing model R^2 and RMSE, and are overlain with boxplots. The Random Forest models for maximum and mean patch height explain 61% (+/- 14% at 2σ) and 59% (+/- 14% at 2σ) of the variation with errors of 1.6m (+/- 0.2m at 2σ) and 1.3 (+/- 0.2m at 2σ), respectively, where 2σ represents the 95% confidence interval.



(a)



(b)

Figure 5-5. The bootstrap-derived distributions of Random Forest model (a) R^2 and (b) RMSE for the indirect forest patch height prediction method whereby all spaceborne variables were used to predict maximum and mean forest patch height.

We computed 95% prediction intervals for patches receiving both direct and indirect height estimates. These prediction intervals show the uncertainty associated with patch-level estimates of both maximum and mean patch heights. Figure 5-6a shows these height estimates and prediction intervals for all patches in this study across the continuum of patch sizes. Figure 5-6b shows the relative prediction error, which was computed as the difference between the upper and lower prediction interval range divided by the predicted height value.

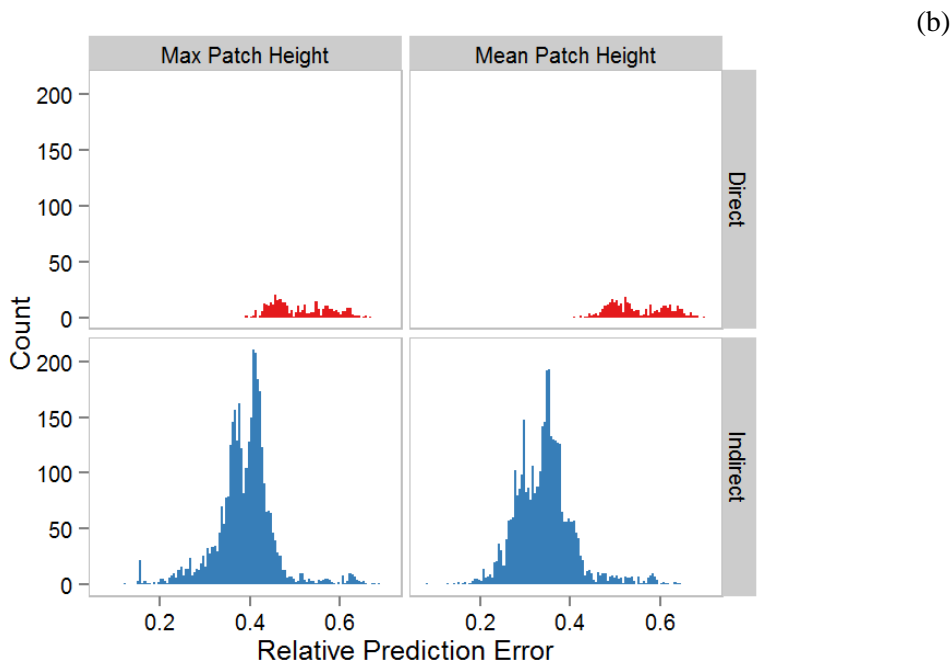
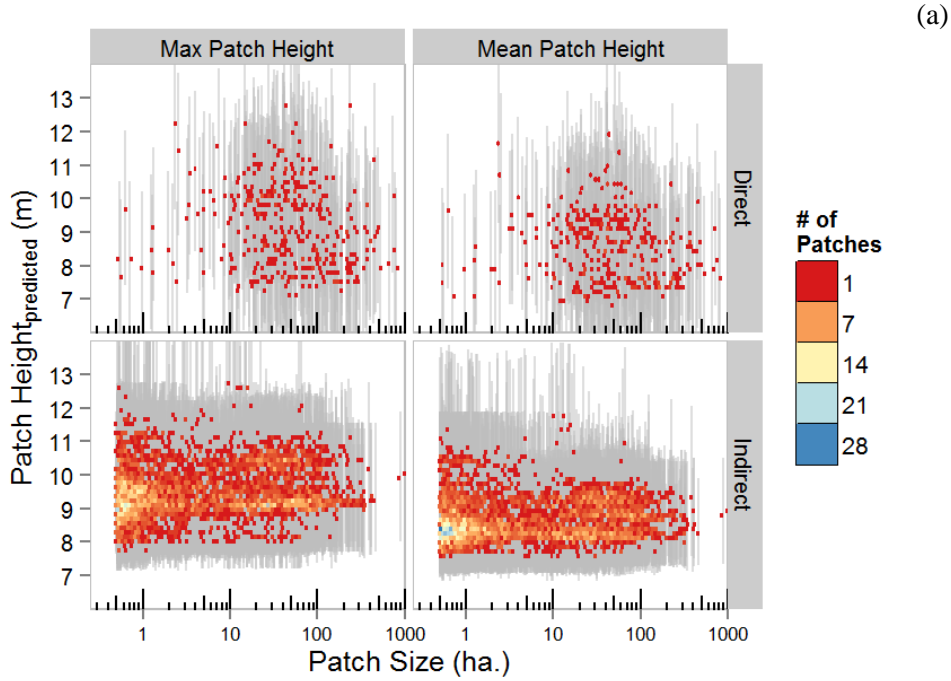


Figure 5-6. (a) Patch height and 95% prediction intervals (grey lines) for patches from direct prediction and indirect prediction shown across the continuum of patch sizes. (b) Distributions of relative prediction error (95% prediction interval) for patch height predictions.

5.5. Discussion

Site-scale monitoring of forest structure may help quantify the potential for change in forest structure and the effects on broader TTE dynamics. Such detailed monitoring is needed to resolve both the variability in TTE forest structure at fine spatial scales and the variability in structural responses to changes in environmental drivers that are observed across the TTE. The high resolution delineation of forest patches at our study sites in the TTE of northern Siberia demonstrates the detailed spaceborne monitoring that is possible for examining spatial patterns of forest structure across the circumpolar domain. The forest patch height prediction intervals are estimates of the uncertainty of measurement error at the forest patch scale that may help discern TTE form linked to variable changes in TTE forest structure.

We first review these estimates of uncertainty and then examine them in the context of a conceptual biogeographic model of TTE forest structure presented in recent literature. Such a model helps clarify and focus spaceborne approaches to examining characteristics of TTE forest structure and its vulnerability to change.

5.5.1. Forest Patch Height Uncertainty

There are four central results regarding the uncertainty of forest patch height across the study area. First, direct forest patch height estimates from a combination of coincident GLAS LiDAR ground surface and HRSI DSM-derived canopy elevations was made for ~9% of forest patches in the study area. Second, the sampling density of these direct height estimates, driven by the sampling scheme of the spaceborne LiDAR, is < 0.5 samples ha^{-1} for 94% of sampled patches. This sampling density is well below the critical density of 16 samples ha^{-1} recommended for sampling forest biomass at the 1ha plot-scale (Huang et al., 2013). These results suggest that the cost of increasing forest patch sizes is a decrease in the density of direct height measurements. This is likely an artifact of the GLAS sampling scheme, whose sampling is regular in the along track direction (1 sample every ~170m), but whose coverage of ground tracks was highly irregular across the landscape. Third, the model that explained the most

variation included all remote sensing data layers. The most important variables were from HRSI. These variables, *NDVI* and *SD_CSR*, are indications of vegetation and its density within forest patches. Fourth, the RMSE and RMSE uncertainty from the best regression tree models predicting maximum and mean forest patch height show forest patch height errors, including error uncertainty at 2σ (95% confidence interval) $< 2\text{m}$. However, the maximum and mean patch height prediction intervals show the uncertainty in the predictions on a patch by patch basis of $\sim 40\%$. These patch-level prediction intervals translate to a maximum patch height error of $\pm 4\text{m}$ for patches with maximum heights of 10m . These errors indicate that patches with maximum heights of 5m and 10m would be statistically indistinguishable on the basis of height. Height is a key attribute of the diffuse TTE forms, which generally feature a gradual decrease of height and tree density across the ecotone. Diffuse forms are the most likely type of general form to demonstrate treeline advance, where 80% of diffuse ecotone sites examined in a meta-analysis show such treeline advance (Harsh and Bader 2009).

These local-scale uncertainties improve upon recent global-scale spaceborne maps of vegetation height. These maps provide height uncertainties (RMSE) of $\sim 6\text{m}$ which is expected given that coarse-scale ($>500\text{m}$) global maps of forest height aggregate many of these height measurement samples across broad spatial extents (M. A. Lefsky, 2010; Simard et al., 2011). This uncertainty can be the difference between the presence or absence of a forest patch in the TTE and is therefore not suited for evaluating the link between TTE forest structure and heterogeneous local scale site factors. The height uncertainty of forest patches, $\sim 90\%$ of which have prediction intervals less than $< 50\%$ of the predicted heights, improves the uncertainty and spatial resolution of TTE forest height measurements. However, this study's primary benefit is in the fidelity of the spatial extent of TTE forest patches. The scale of these patches are more appropriate than coarse, global-scale estimates of forest structure for reporting site-specific forest structure estimates that are critical for understanding forest characteristics at this biome boundary in flux.

5.5.2. Improving the Modeling of Forest Patch Height

A potentially large source of uncertainty of patch height estimates may be attributed to the use of direct height estimates for calibration of the indirect patch height prediction method. A patch's height was determined directly from coincident spaceborne sampling of canopy surface and ground elevations if samples were coincident with the patch. These patches with direct height samples were used to calibrate the Random Forest model relating a suite of satellite image data, averaged across the patch, for indirectly predicting patch heights for those with no coincident direct spaceborne sampling of height. However, the sampling of patch height with coincident LiDAR footprints, which provided the ground surface elevation component of the sampled height estimate, involves sampling a very small portion of overall patch. In theory, the patch itself is a homogenous unit with similar tree structure characteristics throughout, however, the extent to which this assumption holds was not examined. For patches with a high degree of tree structure heterogeneity, a single direct sample of height may not be sufficient to represent either maximum or mean patch heights. These data, when used to train a Random Forest model, will degrade the modeled relationship of mean patch level image characteristics to patch height, because the sample used to determine patch height might not be representative of actual patch height.

There are two ways to address this source of uncertainty. The first is to accumulate more direct samples of forest heights within a patch. This can be accomplished by first identifying ground surfaces within the forest patch and then by using the ground surface elevation measurements from the HRSI DSMs to supplement those from GLAS. This has to be done carefully so as not to introduce errors associated with HRSI DSM ground surface elevation within forested areas (Montesano, Sun, Dubayah, & Ranson, 2014b). Second, the homogeneity of forest patches can be improved by refining algorithms associated with delineating forest patches. This could include decreasing patch size, improving the canopy surface roughness algorithm, and including multi-temporal HRSI to help separate surface features whose reflectance characteristics differ throughout the growing season. These refinements may improve the modeling of forest patch height and ultimately the ability to discern diffuse TTE forms.

5.5.3. Spaceborne Sensing of TTE Form

The conceptual model of ecotone forms presented by Harsch and Bader (2011) describe form as a result of the relative dominance of different controlling mechanisms. Only some of these mechanisms are primarily driven by climate. For the diffuse TTE form, the primary controlling mechanism of this conceptual pattern is the growth-limitation of trees, whereby tree-growth is driven by warming of summer or winter temperatures. Characterization of diffuse TTE forms (discussed in 5.2) by integrating horizontal and vertical structure by forest patch across the TTE with spaceborne data may provide insight into the vulnerability to climate warming of current TTE structure.

5.5.4. Integrating Horizontal and Vertical Vegetation Structure by Forest Patch

This study's spaceborne remote sensing analysis of height within forest patches provided a means to simultaneously account for the horizontal and vertical components of the spatial patterns (biogeography) of trees in the TTE that may help improve depictions of the diffuse TTE form. Recent literature on the biogeography of trees in the TTE explain how tree density and height create for varying forest patterns across the ecotone, that these patterns are important because they may provide clues as to the dynamics of TTE forest structure, and that they should be explored with detailed remote sensing (Bader, Rietkerk, & Bregt, 2007; M. A. Harsch & Bader, 2011; F.-K. Holtmeier & Broll, 2007).

A key element of this study involved integrating and scaling spatially detailed remote sensing observations to map forest patches. These mapped patches help explore the biogeography of TTE forest structure in the context of a conceptual model that highlights the importance of both tree density and height for examining patterns of trees in the TTE. From a remote sensing perspective, tree density is addressed with the delineation of forest patches that use the horizontal structure captured with HRSI. This horizontal structure manifests itself as image texture or the frequency of vegetation across a spatial extent, and may be quantified in terms of surface roughness, canopy cover or stem density. The patch-based approach for aggregating height information was a means to break apart the forested portions of each site by reducing the heterogeneity in horizontal structure. Essentially, the use of the roughness

information derived from HRSI helped establish a basis for the analysis of height by using it as a proxy for vegetation density, and by expressing it as a contiguous patch that served as the fundamental unit by which height was aggregated. This data integration should provide more information for discerning diffuse TTE forms than individual assessments of either tree height or tree density. Finally, the integration of spaceborne data across a range of scales is critical. This suite of data that is available for the entire TTE enables a standardized approach to TTE structure mapping that is appropriate for the broad spatial domain of the TTE while adhering to requirements of site-specific forest structure detail.

The site-scale, patch-based analysis is a fundamental shift away from a pure pixel-based treatment of the landscape. It is driven by two central needs. The first is the need for site-level understanding of TTE vegetation structure characteristics. The second is the need to understand the hierarchy of spatial patterns of trees across the landscape, because of the link between vegetation patterns and ecological processes. This analytical approach should be pursued to more deeply explore the patterns of tree cover across the landscape that are not only formed by height and density of tree cover, but also the size, shape, connectivity and spatial autocorrelation of varying types of forest patches across the TTE.

5.5.5. Implications for Understanding TTE Structure Vulnerability

Understanding the vulnerability of TTE structure is a key objective of research into expected changes in the high northern latitudes (Callaghan, Crawford, Eronen, Hofgaard, et al., 2002a). Vulnerability may be defined as the susceptibility of vegetation structure within the TTE to change, thus shifting the position and character of the TTE (Gonzalez, Neilson, Lenihan, & Drapek, 2010). Multiple lines of evidence indicate that vegetation changes are occurring in the TTE, and that these changes are asynchronous across the circumpolar domain. The most rapid TTE vegetation responses to climate change will occur where climate is the main factor controlling TTE vegetation (Epstein et al., 2004). This suggests that TTE structure is most vulnerable at sites both controlled by, and undergoing changes in, climate. Currently, the reported patch-level forest height uncertainty precludes a clear understanding of the most vulnerable portions of the TTE. However, this remote sensing approach framed by the

conceptual model of TTE form provides a clear directive for near-term work of examining the biogeography of forest structure in the TTE, and understanding and forecasting vegetation responses in the TTE based on the potential for changes (i.e. vulnerability) that these general patterns of forest structure suggest.

Mapped TTE patterns of horizontal and vertical structure, i.e. TTE form, can be integrated with climate data to suggest a gradient of TTE structure vulnerability. These maps can (1) provide information on the patterns of environmental variables that are key drivers of tree growth, and (2) inform plant community and forest gap models that combine temperature, soil and disturbance data to examine the drivers of vegetation structure and forecast its potential for change in the TTE (Epstein, Walker, Chapin, & Starfield, 2000; Xiaodong & Shugart, 2005). For example, understanding form in areas where vegetation structural changes have been noted may help explain the variability of structure change. Furthermore, TTE form categories can serve as a basis for stratifying the TTE to examine the relative importance that other microsite environmental factors such as disturbance regime, aspect, slope and soil conditions have on TTE structure vulnerability across broad scales. Finally, whereas it is unlikely to derive the dominant mechanisms controlling TTE forest structure directly from remote sensing, these mechanisms may be inferred from remotely sensed TTE form. Resolving diffuse TTE forms through better forest patch height estimates will provide evidence as to the general mechanisms that give rise to these diffuse forms (e.g. temperature-limited growth), and could also provide spatially explicit information to individual-based models to help account for the variability in TTE forest structure responses across the circumpolar domain. This will aid long-term forecasting by suggesting the most likely sites for changes to vegetation-disturbance feedbacks and the extent to which biogeophysical interactions may shift (e.g. vegetation effects on surface albedo). The vulnerability of TTE structure to temperature-induced change is one of many factors that may alter ecological processes in the high northern latitudes.

5.6. Conclusions

The vertical component of TTE form, maximum and mean forest patch height, as derived from a suite of spaceborne sensors, has an uncertainty of ~40%. With this uncertainty, forest patches with maximum heights of 5m and 10m are statistically indistinguishable on the basis of height. Height is a key attribute of the diffuse TTE forms, which generally feature a gradual decrease of height and tree density across the ecotone and are the most likely form to demonstrate treeline advance. Differences in patch height are a central feature of the diffuse TTE form where significant structural changes have been observed, and these differences suggests that improving the remote sensing of patch height is a key TTE forest structure variable for examining TTE structure vulnerability to temperature-induced change. The conceptual model of TTE form should continue to guide the application of multi-sensor spaceborne data in the HNL toward classifying the TTE according to form. These forms can be more informative than tree density and height alone, because of the information provided by the structural patterns of groups of forest patches. This work clarifies how improved height estimates at the scale of forest patches can help capture a key characteristic of TTE vulnerability - the portions of the TTE for which temperature is likely the primary control of forest structure. A focus on forest patch height from spaceborne data will provide domain-wide potential for examining TTE structure characteristics.

Chapter 6: Conclusion

6.1. Summary of Findings

Chapter 2 presents a close look at the measurements of boreal forest structure from airborne and spaceborne LiDAR and SAR. The goal of this work was to evaluate the fundamental uncertainty of inferred AGB from these remote sensing measurements coincident with ground-derived AGB, which was the common variable collected across the study sites in Howland, Maine, Aurskog, Norway, and northern Siberia. Given the site-scale importance of vegetation structure in the TTE and the recommendations for observations with remote sensing noted in a number of recent ecological studies, this uncertainty is the first step in evaluating the basic sensitivity to sparse forest structure of frequently used remote sensing platforms. In a statistical gradient of AGB similar to the range of forest structure encountered in the TTE of northern Siberia, airborne LiDAR and SAR produced strong relationships with ground-measured AGB. Airborne SAR and all LiDAR data showed reductions in AGB error as AGB increases from 0-60 Mg·ha⁻¹. Spaceborne LiDAR models with ground AGB were weaker due to significant scatter across the range of measurements, and result in errors from 50-100% for AGB < 80 Mg·ha⁻¹. Spaceborne SAR models were particularly weak, which may be due to a combination of the high-frequency speckle of SAR pixels, scale mismatch between pixels and the ground plots, and forest structure heterogeneity represented in the SAR pixels that is not captured in small ground plots. Airborne SAR models were stronger, likely due to larger ground plots relative to the SAR pixel size, which results in a better estimate of mean backscatter within a plot and thus better correlation with the plot's vegetation structure.

The uncertainty of inferred AGB from current sensors led to inquiry into whether this uncertainty would be addressed with a near-term spaceborne mission. The focus in Chapter 3 is on the potential sensitivity of a new spaceborne LiDAR, ICESat-2, to forest structure in sparse *Larix* forests. The ICESat-2 measurement method (micro-pulse photon counting LiDAR) will be fundamentally different than that of ICESat-GLAS, and questions persist as to how best to use these data for characterizing forest structure.

As such, the goal of this work was to use a radiative transfer model to examine the sensitivity that might be expected from ICESat-2 across a forest structure gradient characteristic of that which exists in the TTE in northern Siberia and then examine the uncertainty of this data for inferring AGB. We used AGB as the surrogate for forest structure in the same manner as in Chapter 1 to provide context for this study's uncertainty results. A key feature of this study was the focus on the optimal link-scale for aggregating data on sparse forest structure. The results show that in *Larix* forests most LiDAR shots will have photons returned to the sensor (>79%), the majority of all photons from all shots (~67%) were signal photons, and that half of the modeled LiDAR shots produced 1 signal photon. These modeling details help explain the effectiveness of this remote sensing technique for producing sparse forest structure data. In synthetic *Larix* stands >20 Mg·ha⁻¹ the distribution of the number of signal returns don't vary significantly. The study also examined the error of AGB measurements derived from the modeled data. The link-scale of 50m optimized the resolution of forest structure, for which there is a trade-off between horizontal precision of the measurement and vertical structure detail. At this scale AGB > 20 Mg·ha⁻¹ have errors ranging from 20-50%, which indicate the difficulty of identifying actual differences in AGB at 10 Mg·ha⁻¹ intervals with ICESat-2.

The results from the previous two chapters suggest broad uncertainty in current and near-term single-sensor spaceborne estimates of TTE forest structure. Chapter 4 sought to mitigate single-sensor uncertainty with a methodology to combine canopy and ground surface elevation measurements from multiple sensors. With ground-measured tree heights in plots coincident with ICESat-GLAS footprints, we assessed the uncertainty of plot-scale spaceborne canopy height measurements. This novel approach combined canopy surface elevations, derived from digital surface models from Worldview-1 stereo image pairs, with coincident ground surface elevation measurements from ICESat-GLAS LiDAR. Modeled canopy height for stands ~5-10m tall produced a moderate model fit with a height error range < 1.5m. This multi-sensor direct height estimation provided an alternative to estimates of canopy height from single sensor by capitalizing on the complementary nature of the surface elevation measurements from each sensor. This approach provided the basis for direct forest patch estimation in Chapter 5.

In Chapter 5, I applied a remote sensing approach to estimate TTE forest height at the patch-scale and explained the importance of the uncertainty of patch height estimates for examining patterns of forest structure and the process to which they are linked. I examined these estimates and their uncertainty within the context of a conceptual biogeographic framework that explains the link between patterns of TTE forest structure and its dynamics. I explained that there remains the potential to identify TTE form with spaceborne data integration, because the patch height uncertainty results reported in this chapter precludes distinguishing patches on the basis of height. A focus on improving forest patch delineation and height estimates at the scale of the forest patch will help identify diffuse TTE forms, which may explain the variability of TTE forest structure change and TTE forest structure vulnerability.

6.2. Synthesis and Implications of Findings

6.2.1. Synthesis

The goals of this dissertation were to examine the uncertainty of remote sensing measurements of forest structure in the taiga-tundra ecotone, integrate spaceborne remote sensing measurements of forest structure in a data fusion approach, and evaluate the uncertainty of spaceborne measurements of forest patch height in the TTE.

This work has demonstrated broad uncertainty in spaceborne structure measurements at plot-scales. These plot-scales suggest the scales at which ground and satellite observations must coincide in order to have confidence in measurements from space. If these plot-scale measurements are represented empirically with spaceborne models that explain, for example < 35% of the plot-level variation in AGB as was the case for the spaceborne SAR models in Chapter 1, this is valuable evidence for exploring coarser scales at which this data can provide information on vegetation structure. Since site-level detail is particularly important for exploring TTE dynamics, the ground plots used for this study effectively represent target scales at which ecologists and biogeographers require spaceborne data for studying patterns of TTE vegetation structure.

This broad uncertainty of TTE vegetation structure at plot-scales drives approaches to data integration. This work explores one approach by integrating spaceborne LiDAR and HRSI measurements of surface elevation at plot-scales to estimate forest canopy height and its uncertainty. The key with this data integration approach and others is to uncover the strengths of individual data sets and link them according to how they may provide complementary information on vegetation structure. For example, GLAS provides high fidelity ground surface elevations measurements in sparse forests even though its overall waveform is not reliable for measuring the heights of sparse and short stature forests. When complemented by canopy surface elevations from HRSI DSMs, we can sample heights of TTE forests in a way that is suited for capturing the canopies of small trees, and aggregate these measurements across a variety of scales.

Spaceborne data integration approaches for examining forest height and density provided the means to assess the uncertainty of mapped TTE forest patch height estimates. This uncertainty was examined within a biogeographic framework that establishes the general categories of forest structure patterns that describe the form of the TTE. These uncertainty estimates demonstrate the challenges and opportunities for improving maps of TTE structure in order to reveal TTE form, which is linked to TTE dynamics and the vulnerability of growth-limited TTE forest structure.

6.2.2. Importance of resolving current TTE structure

This work refines understanding of current TTE structure patterns through an evaluation of the uncertainty of vertical structure in the TTE at scales that ecologists suggest will reveal actual TTE structure variability. This focus on current uncertainty and patterns precedes an attempt for a broad-scale analysis of site-scale forest structure change. This structural uncertainty and these spatial patterns of TTE forest structure, TTE form, which vary across the circumpolar domain are important for two reasons. First, assessment of fine-scale changes across a broad domain may not be reliable if the magnitude of the uncertainty in TTE structure disguises actual variability in structure and exceeds the magnitude of structural changes seen in ground observations. Second, this variability in form may guide future

analyses of change by providing geographic focus as to where the most significant change might be expected, which will provide valuable input for predictions from ecosystem models. Careful examination of the uncertainty of structure observations from spaceborne approaches to TTE mapping will help resolve actual structural variability across the TTE, the patterns of which will reveal varying TTE structure vulnerability.

6.2.3. Emerging Potential for Identifying TTE Structure Vulnerability

The study of site-level TTE structure change, which provides evidence of the vulnerability of TTE structure across broad scales, has been difficult for a number of reasons. For much of the circumpolar domain, structure change takes place on the order of decades, requiring from spaceborne data a time-series with sufficient spatial detail to resolve these changes. The spaceborne data that facilitates site-scale structure analysis (commercial HRSI) has existed in limited quantities since the launch of IKONOS in 1999, with HRSI data volumes and repeat coverage increasing with subsequent launches of Quickbird (2001), and Worldview-1 (2007), -2 (2009) and -3 (2014). The volume of HRSI data across such a broad domain has limited the pool of scientists to only those with access to large data storage capacity, powerful parallel computer processing, and software that can automate routines on raw data. This combination of the a short (< 15 years) times series of HRSI data, limited repeat coverage, the decade-scale nature of TTE forest structure change, and hardware and software limitations has slowed progress on domain-wide analysis of site-scale changes in TTE structure. However, the improvement of open-source software for processing HRSI data (AMES Stereo Pipeline; (Moratto et al., 2010)) along with the opening of commercial data archives (Neigh, Masek, & Nickeson, 2013a), funding for broad-scale studies in the Arctic/Boreal (<http://above.nasa.gov/>), and the availability of cloud storage and super-computer access facilitate circumpolar assessment of TTE structure with a ‘Big Data’ approach that includes integrating repeat and time-series measurements of TTE vegetation from multiple spaceborne sources to examine the spatial patterns of TTE structure.

There are also emerging opportunities to improve our understanding of these spatial patterns from space. These opportunities include the integration of spaceborne observations from recently launched spaceborne sensors that have begun to contribute to domain-wide measurements of TTE structure and its patterns (e.g. Worldview-3 and PALSAR-2 in 2014 and Tandem-X in 2010) and near-term spaceborne LiDAR and SAR (e.g. ICESat-2 and NISAR). Each of these sensors will provide finely-scaled coverage of the entire TTE domain. Adapting the methods presented in this dissertation to incorporate data that can resolve site-scale TTE forest characteristics should improve characterization of the horizontal and vertical patterns of TTE vegetation structure. For example, one factor associated with identifying TTE form is the sampling of height measurements across patches. This is, in part, limited by the number of ground surface measurements. In sparse forests, ICESat-2 is expected to provide strong ground surface returns at a very fine scale along a transect. This data collection scheme will not only provide much needed ground surface elevations samples, but also offer flexibility for how these samples may be aggregated to refine elevation measurements along each transect (e.g., variable segment lengths, moving segment length averaging). These samples will add to those from ICESat-GLAS to improve forest patch height estimates. Finally, spaceborne L-band SAR from PALSAR-2 and NISAR should offer data at spatial resolutions that are better suited for examining TTE structure patterns. Specifically, these data can add to forest density and roughness inputs that help to delineate forest patch boundaries.

Specific methodological approaches to exploring the variability in the characteristics and dynamics of TTE structure will continue to evolve. This work pursued a means for exploring this variability with a remote sensing analysis focused on the uncertainty of spaceborne measurements of forest structure for resolving TTE structure patterns. What remains to be seen is if spaceborne measurements can provide sufficient spatial detail across the TTE domain with a level of certainty that will allow for a deeper understanding of vegetation patterns, the drivers of those patterns, and accurate prediction of fine-scale ecosystem responses to the changes in earth system processes that are underway.

Appendix: Description of Field Sites

A.1. Introduction

Field sites in and around central Maine, central Siberia, and Aurskog, Norway provided data used to form the statistical gradient of forest structure analysis in Chapter 2. Chapters 3-5 used field data collected along the Kotuykan River in central Siberia in 2008. The information below includes descriptions of the study areas and stand characteristics for field sites in Maine, Siberia and Norway.

A.2. Central Maine Field Sites

Field campaigns were conducted in central Maine in 2009, 2010, and 2011 to collect individual tree structure measurements (DBH, height) at circular field plots (10m radius) coincident with LVIS LiDAR footprints (Figure A1). Field plots were associated with three general forest category. These categories were (1) Bog Edges: semi-natural forest transitions at bog (poor fen) edges where forest transitions to open bog (e.g., Alton Bog) (Schauffler, Jacobson, Pugh, & Norton, 1996), (2) Howland Stem Map: an old growth site (> 100 yrs) associated with the Howland Forest stem map (G. Sun et al., 2011), and (3) Howland Forest: stands associated with frequent and recurring forest thinning in the Northern Experimental Forest in Howland, Maine. These categories yielded field plot estimates of AGB ranging from 0 - 358 Mg·ha⁻¹ (Figure A2). The portion of these field sites ranging from 0 - 100 Mg·ha⁻¹ were used to report AGB error and error uncertainty in Chapter 2.

Unlike sites in Norway and Siberia, the sites in Maine are located in southern boreal-temperate forest transition zone (Hollinger et al., 1999; Olson et al., 2001). The sites selected, however, helped form a statistical gradient of AGB that correspond to AGB gradients in the TTE of northern Siberia. Stand dominance differed between general forest types. *Larix sp.* and *Pinus sp.* account for the majority of individuals at Bog Edges. *Picea sp.*, *Thuja sp.* and *Tsuga sp.* dominate the canopy of the Howland Stem Map while *Abies sp.* is the most prominent individual in the understory. At sites across Howland

Forest *Abies sp.*, *Betula sp.*, *Tsuga sp.*, and *Picea sp.* account for the majority of individuals. Conifer-dominance was consistent across the vast majority of stands sampled. Stems densities at sites < 100 Mg·ha⁻¹ across all forest types in Maine were < 3000 stems ha⁻¹ and included only one site within the Howland Stem Map. Stem densities for stands in Howland Forest did not increase with AGB in the same manner as those at Bog Edges, which is likely a result of the management practices at work across this Experimental Forest (Figure A3). Stem densities for plots were calculated from stems with DBH ≥ 5cm at Bog Edges and ≥ 3cm elsewhere.

A.3. Siberia Field Sites

Field campaigns were conducted in central Siberia in 2007 (Kochechum River), 2008 (Kotuykan River), and 2010 (West Siberian Plains) to collect individual tree structure measurements (DBH, height) at circular field plots (10m or 15m radius) coincident with ICESat-GLAS LiDAR footprints. These campaigns yielded field plot estimates of AGB ranging from 0-459 Mg·ha⁻¹ (Figure A4). The portion of these field sites ranging from 0-100 Mg·ha⁻¹ was used to report AGB error and error uncertainty in Chapter 2. Chapters 3-5 used exclusively the Kotuykan River dataset, the most northerly portion of the field sites.

These campaigns covered two general ecological regions; the Eastern Siberian Taiga (Kochechum River, Kotuykan River) and the Western Siberian Taiga (referred to as the West Siberian Plains) (Olson et al., 2001). Navigation by river was necessary during the 2007 and 2008 expeditions down the Kochechum and Kotuykan Rivers in the Siberian Traps geologic province in the absence of roads where there is little direct human influence on the landscape. In the West Siberian Plains in 2010, navigation with a 4-wheel drive vehicle was possible given road access in the Tomsk Oblast, a region with a history of extensive human use and management of forests. All field expedition sites are subject to severe continental climates.

The sites surveyed along the Kochechum and Kotuykan Rivers include natural forest stands whose canopy is exclusively *Larix gmelinii* (Rupr.). Figure A5 shows the distribution of structural

characteristics (DBH and height) for trees surveyed during the three campaigns. The Kotuykan River sites (~70°N) and the Kochechum River sites (62°N-66°N) featured open canopy stands with mean tree heights of 6.5m +/- 2.2 m and 6.7m +/-2.6m respectively. Stands surveyed at these sites grow on flat or gently sloping terrain and are associated with continuous permafrost (Gruber, 2012). At some sites along the Kochechum River *Betula pendula* Roth was observed but not included in tree inventories of trees \geq 3cm DBH. Fire return intervals vary from ~ 77 - ~320 years at the Kochechum sites. An interval of ~164 years at the Kotuykan sites is likely a conservative estimate because the mean age of sampled trees was greater than 250 yrs (V. Kharuk et al., 2013b; V. I. Kharuk et al., 2011; V. Kharuk, Dvinskaya, & Ranson, 2013a).

The sites surveyed in the West Siberian Plains in 2010 included a mix of natural forest and post-harvest regeneration (Bergen et al., 2008). The dominant canopy species, which varied according to site, were primarily *Pinus sylvestris* and *Betula pendula* and to a lesser extent *Populus tremula*, *Pinus siberica*, *Picea obovata*, and *Abies siberica*. There is no permafrost associated with these sites and fires and human harvesting are the primary disturbances in the region. These sites were included in this study primarily to incorporate AGB sites from 70 - 100 Mg·ha⁻¹. Incorporating these sites into the study involved a trade-off whereby more AGB sites at the high end of the statistical gradient were gained. The cost was that including these sites introduced stands with species composition that differed significantly from those sites with pure *Larix* stands along the Kochechum and Kotuykan Rivers. Furthermore, the association of stem densities with plot AGB is clearly different at the Western Siberian Plains sites from those of the pure *Larix* stands (Figure A6).

A.4. Norway Field Sites

The ALS-based estimates of AGB at ICESat-GLAS footprints in Aurskog, Norway used in Chapter 2 were derived from field surveys and airborne stand inventories described in recent literature (Breidenbach, Næsset, Lien, Gobakken, & Solberg, 2010; Næsset et al., 2011; Næsset & Gobakken, 2008). Naesset et al. (2008) provide a description of the forest stands associated with this Aurskog,

Norway dataset in Table 2 (area 8), where they describe conifer-dominant young stands composed of 39% spruce, 49% pine and 12% deciduous species. Mature stands were divided into two categories: those associated with poor and good site conditions based on mean annual increment of less than (poor) or greater than or equal to (good) $4.5 \text{ m}^2 \text{ ha}^{-1} \text{ yr}^{-1}$. Mature stands at poor sites featured Pine species dominance (79%) with 16% spruce species and 5% deciduous. Mature stands at good sites featured more even proportions of Spruce (51) and Pine species (46) with 3% deciduous. The Aurskog stands used in this dissertation spanned a range of AGB from 0-100 $\text{Mg} \cdot \text{ha}^{-1}$, which are described as comprising a portion of the natural variation found in the Nordic boreal forest.

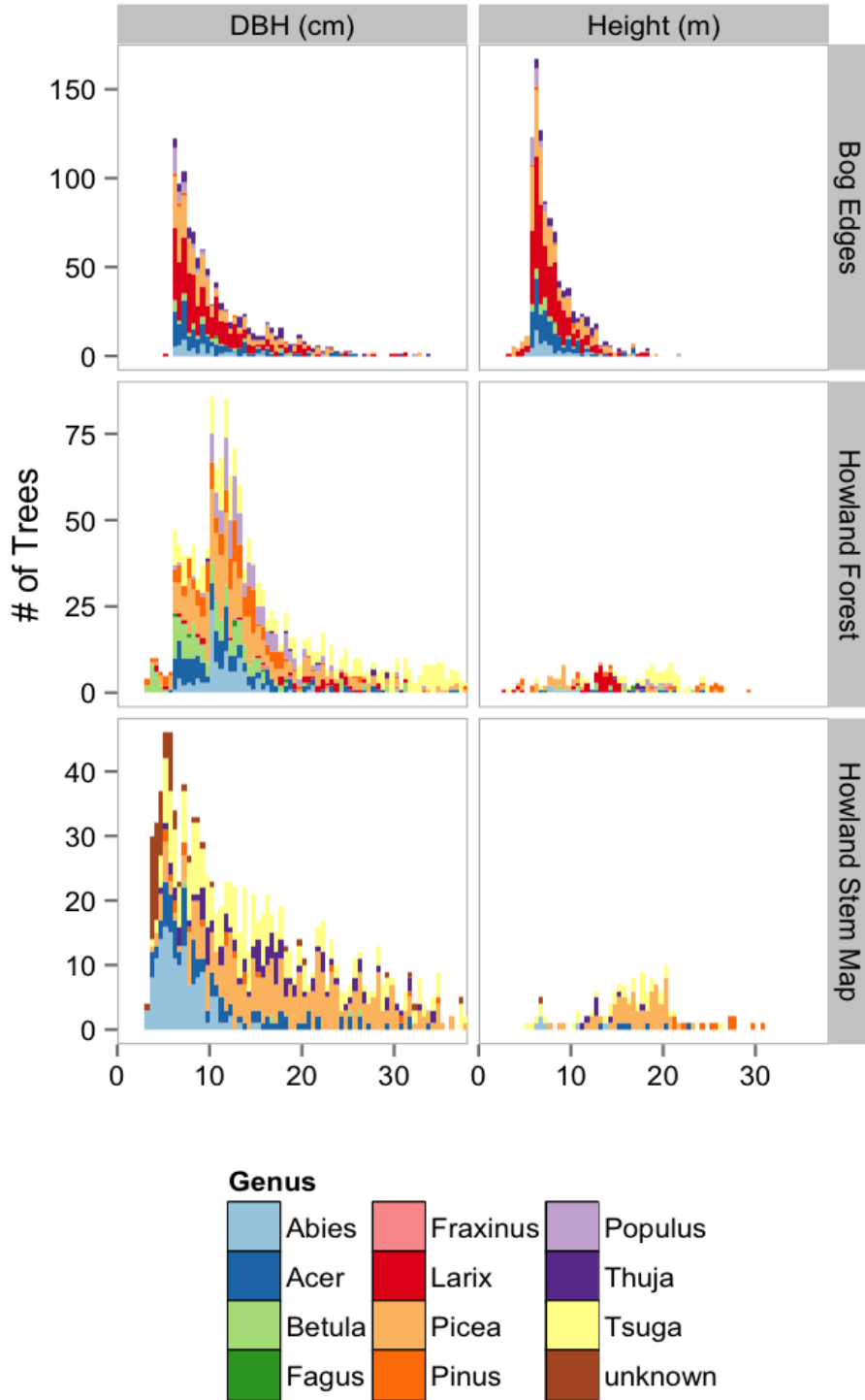


Figure A1. Histograms showing the distribution of DBH and height measurements of individual trees, broken down by genus, in field plots for each forest category in the central Maine study area.

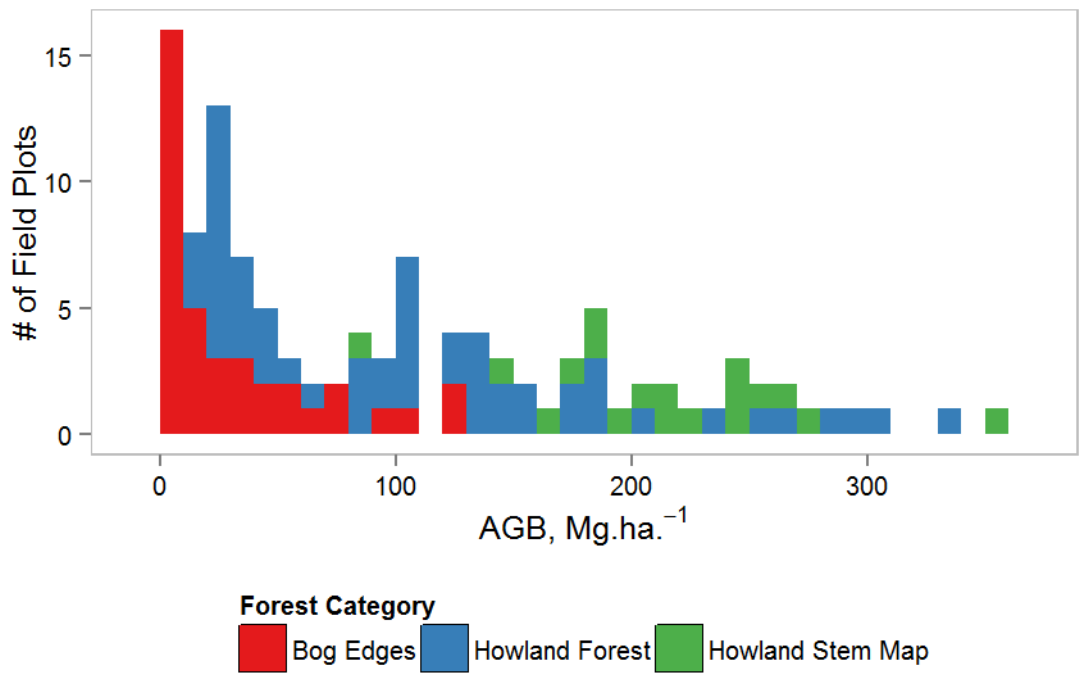


Figure A2. Histogram showing the distribution of field-inferred AGB calculated by field plot for each forest category in the central Maine study area.

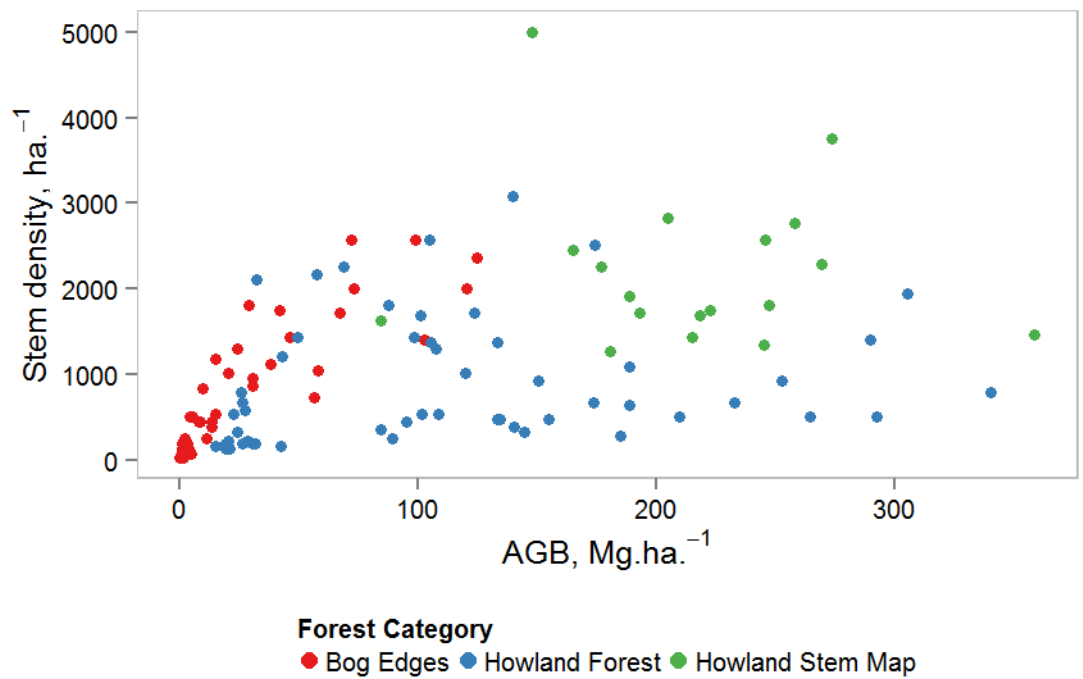


Figure A3. Scatterplot showing the stem density and AGB for each plot across the 3 forest categories in the central Maine study area.

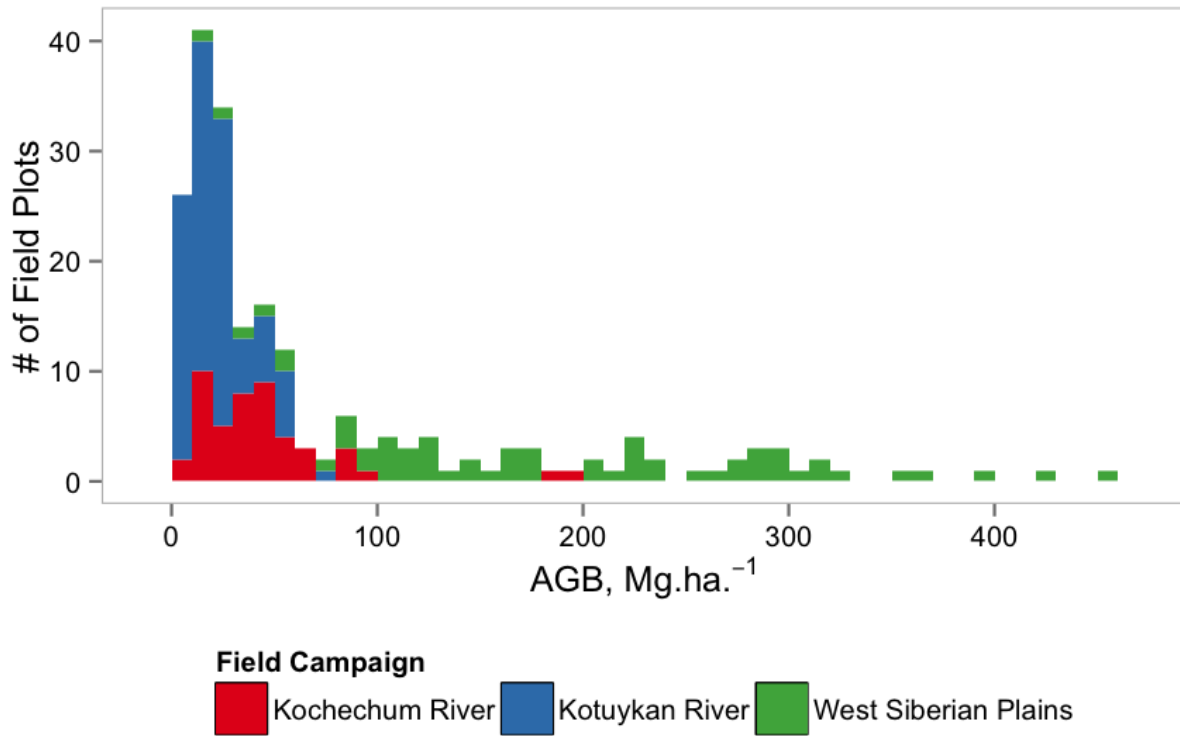


Figure A4. Histogram showing the distribution of field-inferred AGB calculated by field plot for each of field campaign in the Siberia study area.

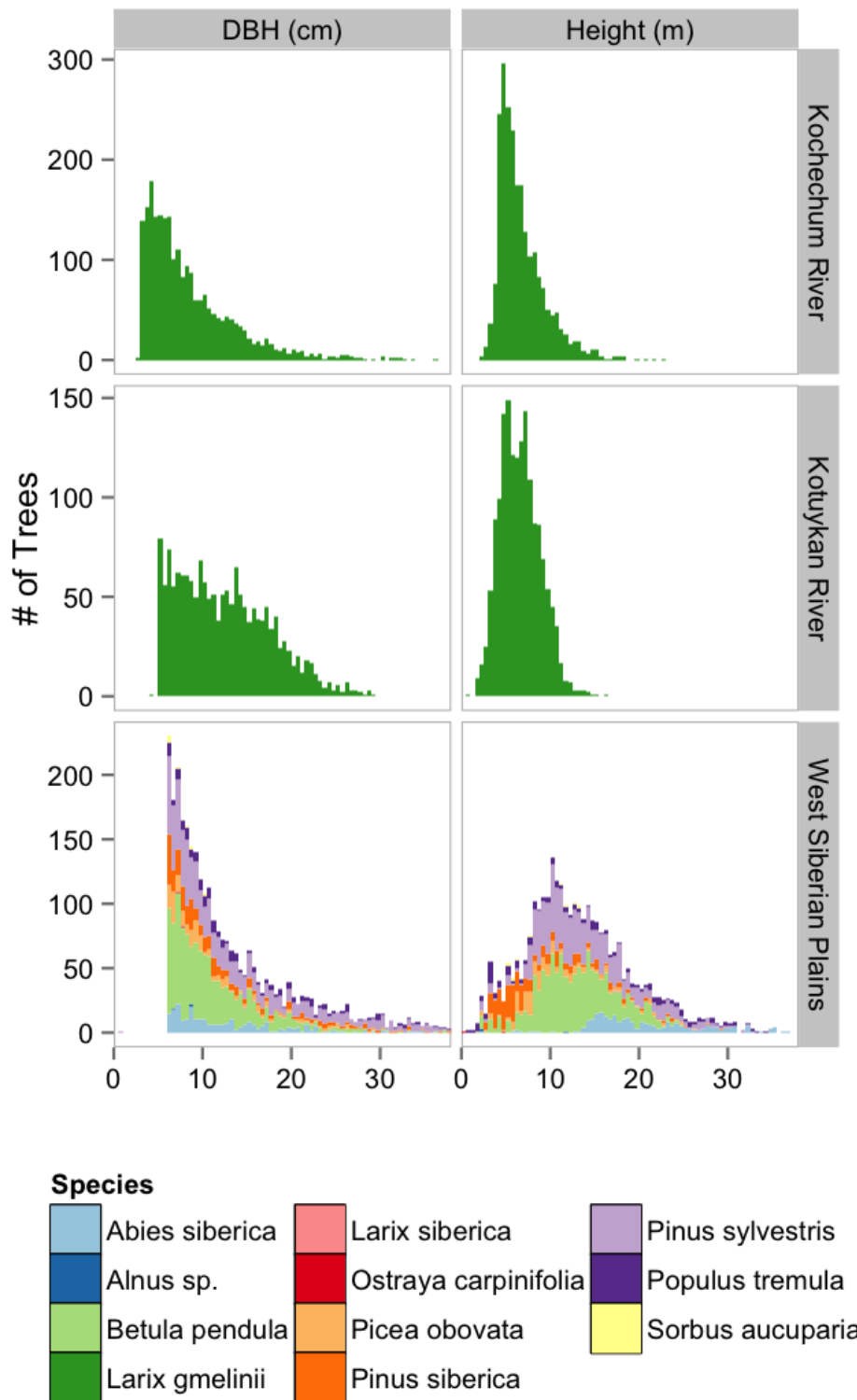


Figure A5. Histograms showing the distribution of DBH and height measurements of individual trees, broken down by species, in field plots for each field campaign in the Siberia study area.

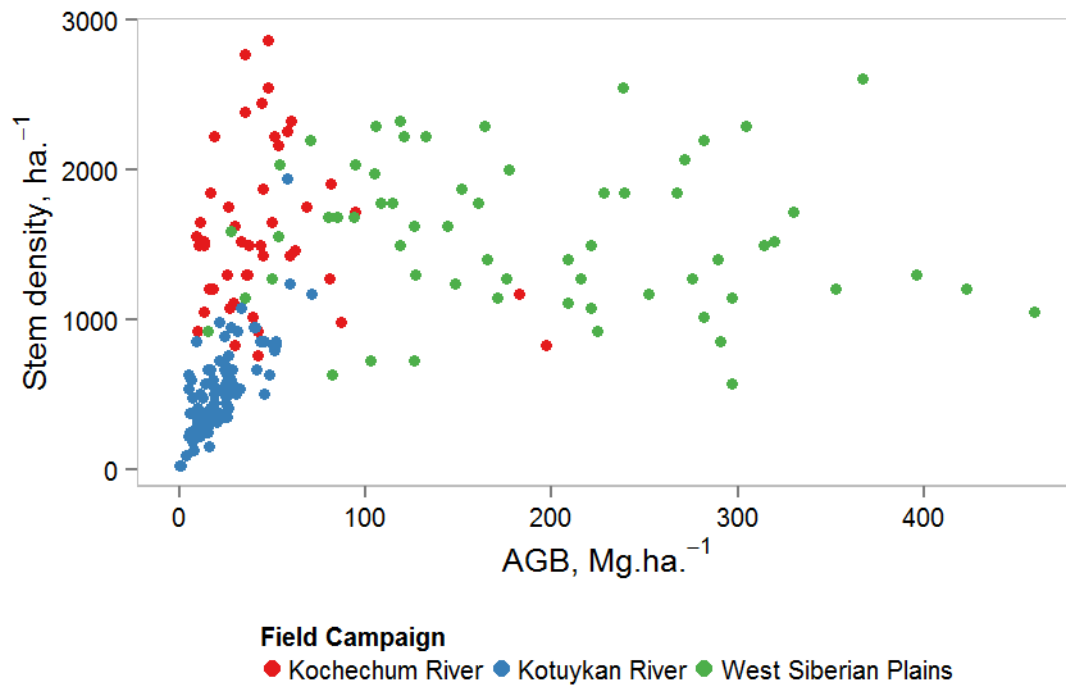


Figure A6. Scatterplot showing the stem density and AGB for each plot across the 3 field campaigns in the Siberia study area.

Bibliography

- Abaimov, A. P. (2009). Geographical Distribution and Genetics of Siberian Larch Species. In *Ecological Studies* (Vol. 209, pp. 41–58). Dordrecht: Ecological Studies. doi:10.1007/978-1-4020-9693-8_3
- Abdalati, W., Zwally, H. J., Bindenschadler, R., Csatho, B., Farrell, S. L., Fricker, H. A., et al. (2010). The ICESat-2 laser altimetry mission. *Proceedings of the IEEE*, 98(5), 735–751.
- Abshire, J. B., Sun, X., Riris, H., Sirota, J. M., McGarry, J. F., Palm, S., et al. (2005). Geoscience Laser Altimeter System (GLAS) on the ICESat mission: on-orbit measurement performance. *Geophysical Research Letters*, 32(21), L21S02.
- ACIA. (2004). *Impacts of a Warming Arctic*. Cambridge University Press.
- ACIA. (2005). *Arctic Climate Impact Assessment*. Cambridge University Press.
- Aguilar, M. A., del Mar Saldana, M., & Aguilar, F. J. (2014). Generation and quality assessment of stereo-extracted DSM from GeoEye-1 and WorldView-2 imagery. *Geoscience and Remote Sensing, IEEE Transactions on*, 52(2), 1259–1271.
- Ahmed, R., Siqueira, P., & Hensley, S. (2013). Analyzing the Uncertainty of Biomass Estimates From L-Band Radar Backscatter Over the Harvard and Howland Forests. *IEEE Transactions on Geoscience and Remote Sensing*, 1–19. doi:10.1109/TGRS.2013.2273738
- Alexeyev, V. A., & Birdsey, R. A. (1998). Carbon storage in forests and peatlands of Russia. *General Technical Report NE-244*. Radnor, PA: U.S. Department of Agriculture, Forest Service, Northeastern Research Station, 137.
- Baccini, A., Laporte, N., & Goetz, S. (2008). A first map of tropical Africa's above-ground biomass derived from satellite imagery. *Environmental Research Letters*, 3(4), 045011.
- Bader, M. Y., Rietkerk, M., & Bregt, A. K. (2007). Vegetation Structure and Temperature Regimes of Tropical Alpine Treelines. *Arctic, Antarctic, and Alpine Research*, 39(3), 353–364. doi:10.1657/1523-0430(06-055)[BADER]2.0.CO;2
- Baskerville, G. L. (1972). Use of Logarithmic Regression in the Estimation of Plant Biomass. *Canadian Journal of Forest Research*, 2(1), 49–53.
- Beck, P. S. A., Goetz, S. J., Mack, M. C., Alexander, H. D., Jin, Y., Randerson, J. T., & Loranty, M. M. (2011a). The impacts and implications of an intensifying fire regime on Alaskan boreal forest composition and albedo. *Global Change Biology*, 17(9), 2853–2866. doi:10.1111/j.1365-2486.2011.02412.x
- Beck, P. S. A., Juday, G. P., Alix, C., Barber, V. A., Winslow, S. E., Sousa, E. E., et al. (2011b). Changes in forest productivity across Alaska consistent with biome shift. *Ecology Letters*, 14(4), 373–379. doi:10.1111/j.1461-0248.2011.01598.x
- Bekker, M. F. (2005). Positive feedback between tree establishment and patterns of subalpine forest advancement, Glacier National Park, Montana, USA. *Arctic, Antarctic, and Alpine Research*, 37(1), 97–107.
- Bergen, K. M., Goetz, S. J., Dubayah, R. O., Henebry, G. M., Hunsaker, C. T., Imhoff, M. L., et al. (2009). Remote sensing of vegetation 3-D structure for biodiversity and habitat: Review and implications for lidar and radar spaceborne missions. *Journal of Geophysical Research*, 114. doi:10.1029/2008JG000883
- Bergen, K. M., Zhao, T., Kharuk, V., Blam, Y., Brown, D. G., Peterson, L. K., & Miller, N. (2008). Changing regimes: Forested land cover dynamics in Central Siberia 1974 to 2001. *Photogrammetric Engineering & Remote Sensing*, 74(6), 787–798.
- Berner, L. T., Beck, P. S. A., Bunn, A. G., & Goetz, S. J. (2013). Plant response to climate change along the forest-tundra ecotone in northeastern Siberia. *Global Change Biology*, 3449–3462. doi:10.1111/gcb.12304
- Berner, L. T., Beck, P. S. A., Loranty, M. M., Alexander, H. D., Mack, M. C., & Goetz, S. J. (2012). Cajander larch (*Larix cajanderi*) biomass distribution, fire regime and post-fire recovery in northeastern Siberia. *Biogeosciences*, 9(10), 3943–3959. doi:10.5194/bg-9-3943-2012

- Betts, R. A. (2000). Offset of the potential carbon sink from boreal forestation by decreases in surface albedo. *Nature*, 408(6809), 187–190.
- Bjarnadottir, B., Inghammar, A. C., Brinker, M. M., & Sigurdsson, B. D. (2007). Single tree biomass and volume functions for young Siberian larch trees (*Larix sibirica*) in eastern Iceland. *Icelandic Agricultural Sciences*, 20, 125–135.
- Blair, J., Rabine, D., & Hofton, M. (1999). The Laser Vegetation Imaging Sensor: a medium-altitude, digitisation-only, airborne laser altimeter for mapping vegetation and topography. *ISPRS Journal of Photogrammetry and Remote Sensing*, 54(2), 115–122.
- Blok, D., Heijmans, M., Schaepman-Strub, G., Kononov, A. V., Maximov, T. C., & Berendse, F. (2010). Shrub expansion may reduce summer permafrost thaw in Siberian tundra. *Global Change Biology*, 16(4), 1296–1305.
- Blok, D., Schaepman-Strub, G., Bartholomeus, H., Heijmans, M. M. P. D., Maximov, T. C., & Berendse, F. (2011). The response of Arctic vegetation to the summer climate: relation between shrub cover, NDVI, surface albedo and temperature. *Environmental Research Letters*, 6(3), 035502. doi:10.1088/1748-9326/6/3/035502
- Bonan, G. B. (2008). Forests and Climate Change: Forcings, Feedbacks, and the Climate Benefits of Forests. *Science*, 320(5882), 1444–1449. doi:10.1126/science.1155121
- Bonan, G. B., Chapin, F. S., & Thompson, S. L. (1995). Boreal forest and tundra ecosystems as components of the climate system. *Climatic Change*, 29(2), 145–167.
- Bonan, G. B., Pollard, D., & Thompson, S. L. (1992). Effects of boreal forest vegetation on global climate. *Nature*, 359.
- Bondarev, A. (1997). Age distribution patterns in open boreal Dahurican larch forests of Central Siberia. *Forest Ecology and Management*, 93(3), 205–214.
- Bonfils, C. J. W., Phillips, T. J., Lawrence, D. M., Cameron-Smith, P., Riley, W. J., & Subin, Z. M. (2012). On the influence of shrub height and expansion on northern high latitude climate. *Environmental Research Letters*, 7(1), 015503. doi:10.1088/1748-9326/7/1/015503
- Boyle, S. A., Kennedy, C. M., Torres, J., Colman, K., Pérez-Estigarribia, P. E., & la Sancha, de, N. U. (2014). High-Resolution Satellite Imagery Is an Important yet Underutilized Resource in Conservation Biology. *PLoS ONE*, 9(1), e86908. doi:10.1371/journal.pone.0086908.t002
- Breidenbach, J., Næsset, E., Lien, V., Gobakken, T., & Solberg, S. (2010). Prediction of species specific forest inventory attributes using a nonparametric semi-individual tree crown approach based on fused airborne laser scanning and multispectral data. *Remote Sensing of Environment*, 114(4), 911–924. doi:10.1016/j.rse.2009.12.004
- Breiman, L. (2001). Random forests. *Machine Learning*, 45(1), 5–32.
- Callaghan, T. V., Bergholm, F., Christensen, T. R., Jonasson, C., Kokfelt, U., & Johansson, M. (2010). A new climate era in the sub-Arctic: Accelerating climate changes and multiple impacts. *Geophysical Research Letters*, 37(14), L14705. doi:10.1029/2009GL042064
- Callaghan, T. V., Crawford, R. M., Eronen, M., Hofgaard, A., Payette, S., Rees, W. G., et al. (2002a). The dynamics of the tundra-taiga boundary: an overview and suggested coordinated and integrated approach to research. *Ambio*, 3–5.
- Callaghan, T. V., Werkman, B. R., & Crawford, R. M. (2002b). The tundra-taiga interface and its dynamics: Concepts and applications. *Ambio*, 6–14.
- Capaldo, P. (2012). DSM generation from high resolution imagery: applications with WorldView-1 and Geoeye-1. *Italian Journal of Remote Sensing*, 41–53. doi:10.5721/ItJRS20124414
- Carabajal, C. C., & Harding, D. J. (2006). SRTM C-band and ICESat laser altimetry elevation comparisons as a function of tree cover and relief. *Photogrammetric Engineering & Remote Sensing*, 72(3), 287–298.
- Cartus, O., Kellndorfer, J., Rombach, M., & Walker, W. (2012). Mapping Canopy Height and Growing Stock Volume Using Airborne Lidar, ALOS PALSAR and Landsat ETM. *Remote Sensing*, 4(11), 3320–3345. doi:10.3390/rs4113320
- Chapin, F. (2000). Consequences of changing biodiversity. *Nature*, 405, 234–242.

- Chapin, F. S. (2005). Role of Land-Surface Changes in Arctic Summer Warming. *Science*, 310(5748), 657–660. doi:10.1126/science.1117368
- Chapin, F. S., Mcguire, A. D., Randerson, J., Pielke, R., Baldocchi, D., Hobbie, S. E., et al. (2000). Arctic and boreal ecosystems of western North America as components of the climate system. *Global Change Biology*, 6(S1), 211–223.
- Chopping, M. (2011). CANAPI: canopy analysis with panchromatic imagery. *Remote Sensing Letters*, 2(1), 21–29. doi:10.1080/01431161.2010.486805
- Cook, B., Corp, L., Nelson, R., Middleton, E., Morton, D., McCorkel, J., et al. (2013). NASA Goddard's LiDAR, Hyperspectral and Thermal (G-LiHT) Airborne Imager. *Remote Sensing*, 5(8), 4045–4066. doi:10.3390/rs5084045
- D'Odorico, P., He, Y., Collins, S., De Wekker, S. F. J., Engel, V., & Fuentes, J. D. (2012). Vegetation-microclimate feedbacks in woodland-grassland ecotones. *Global Ecology and Biogeography*, 22(4), 364–379. doi:10.1111/geb.12000
- Dalen, L., & Hofgaard, A. (2005). Differential regional treeline dynamics in the Scandes Mountains. *Arctic, Antarctic, and Alpine Research*, 37(3), 284–296.
- Danby, R. K. (2011). Monitoring forest–tundra ecotones at multiple scales. *Geography Compass*, 5(9), 623–640.
- Danby, R. K., & Hik, D. S. (2007). Variability, contingency and rapid change in recent subarctic alpine tree line dynamics. *Journal of Ecology*, 95(2), 352–363. doi:10.1111/j.1365-2745.2006.01200.x
- Davis, R. E., Hardy, J. P., Ni, W., Woodcock, C., McKenzie, J. C., Jordan, R., & Li, X. (1997). Variation of snow cover ablation in the boreal forest: A sensitivity study on the effects of conifer canopy. *Journal of Geophysical Research: Atmospheres (1984–2012)*, 102(D24), 29389–29395.
- Devi, N. M., Hagedorn, F., Moiseev, P., Bugmann, H., Shiyatov, S. G., Mazepa, V. S., & Rigling, A. (2008). Expanding forests and changing growth forms of Siberian larch at the Polar Urals treeline during the 20th century. *Global Change Biology*, 14(7), 1581–1591. doi:10.1111/j.1365-2486.2008.01583.x
- Dietze, M. C., Wolosin, M. S., & Clark, J. S. (2008). Capturing diversity and interspecific variability in allometries: A hierarchical approach. *Forest Ecology and Management*, 256(11), 1939–1948. doi:10.1016/j.foreco.2008.07.034
- Dobson, M. C., Ulaby, F. T., LeToan, T., Beaudoin, A., Kasischke, E. S., & Christensen, N. (1992). Dependence of radar backscatter on coniferous forest biomass. *Geoscience and Remote Sensing, IEEE Transactions on*, 30(2), 412–415.
- Drake, J., Dubayah, R., Clark, D., Knox, R., Blair, J. B., Hofton, M., et al. (2002). Estimation of tropical forest aboveground biomass using large-footprint lidar. *Remote Sensing of Environment*, 79, 305–319.
- Dubayah, R. O., Sheldon, S. L., Clark, D. B., Hofton, M. A., Blair, J. B., Hurtt, G. C., & Chazdon, R. L. (2010). Estimation of tropical forest height and biomass dynamics using lidar remote sensing at La Selva, Costa Rica. *Journal of Geophysical Research*, 115, G00E09. doi:10.1029/2009JG000933
- Dubayah, R., & Drake, J. (2000). Lidar remote sensing for forestry. *Journal of Forestry*, 98(8), 44–46.
- Dufour-Tremblay, G., Lévesque, E., & Boudreau, S. (2012). Dynamics at the treeline: differential responses of *Picea mariana* and *Larix laricina* to climate change in eastern subarctic Québec. *Environmental Research Letters*, 7(4), 044038. doi:10.1088/1748-9326/7/4/044038
- Duncanson, L. I., Niemann, K. O., & Wulder, M. A. (2010). Estimating forest canopy height and terrain relief from GLAS waveform metrics. *Remote Sensing of Environment*, 114(1), 138–154.
- Dungan, J. L. (2006). Toward a comprehensive view of uncertainty in remote sensing analysis. In G. M. Foody & P. M. Atkinson, *Uncertainty in remote sensing and GIS* (pp. 25–35). Wiley Online Library.
- Elmendorf, S. C., Henry, G. H. R., Hollister, R. D., Björk, R. G., Boulanger-Lapointe, N., Cooper, E. J., et al. (2012). Plot-scale evidence of tundra vegetation change and links to recent summer warming. *Nature Climate Change*, 2(6), 453–457. doi:10.1038/nclimate1465
- Epstein, H. E., Beringer, J., Gould, W. A., Lloyd, A. H., Thompson, C. D., Chapin, F. S., et al. (2004). The nature of spatial transitions in the Arctic. *Journal of Biogeography*, 31(12), 1917–1933.

- Epstein, H. E., Myers-Smith, I., & Walker, D. A. (2013). Recent dynamics of arctic and sub-arctic vegetation. *Environmental Research Letters*, 8(1), 015040. doi:10.1088/1748-9326/8/1/015040
- Epstein, H. E., Walker, M. D., Chapin, F. S., III, & Starfield, A. M. (2000). A transient, nutrient-based model of arctic plant community response to climatic warming. *Ecological Applications*, 10(3), 824–841.
- Esper, J., & Schweingruber, F. H. (2004). Large-scale treeline changes recorded in Siberia. *Geophysical Research Letters*, 31(6), L06202. doi:10.1029/2003GL019178
- Euskirchen, E. S., Mcguire, A. D., Kicklighter, D. W., Zhuang, Q., Clein, J. S., Dargaville, R. J., et al. (2006). Importance of recent shifts in soil thermal dynamics on growing season length, productivity, and carbon sequestration in terrestrial high-latitude ecosystems. *Global Change Biology*, 12(4), 731–750. doi:10.1111/j.1365-2486.2006.01113.x
- Evans, J. S., Hudak, A. T., Faux, R., & Smith, A. M. S. (2009). Discrete Return Lidar in Natural Resources: Recommendations for Project Planning, Data Processing, and Deliverables. *Remote Sensing*, 1(4), 776–794. doi:10.3390/rs1040776
- Flewellling, J. W., & Pienaar, L. V. (1981). Multiplicative regression with lognormal errors. *Forest Science*, 27(2), 281–289.
- Forbes, B. C., Fauria, M. M., & Zetterberg, P. (2010). Russian Arctic warming and “greening” are closely tracked by tundra shrub willows. *Global Change Biology*, 16(5), 1542–1554. doi:10.1111/j.1365-2486.2009.02047.x
- Frazer, G. W., Magnussen, S., Wulder, M. A., & Niemann, K. O. (2011). Simulated impact of sample plot size and co-registration error on the accuracy and uncertainty of LiDAR-derived estimates of forest stand biomass. *Remote Sensing of Environment*, 115(2), 636–649. doi:10.1016/j.rse.2010.10.008
- Frey, C., Penman, J., Hanle, L., Monni, S., & Ogle, S. (2006). Volume 1: General Guidelines and Reporting. *2006 IPCC Guidelines for National Greenhouse Gas Inventories, National Greenhouse Gas Inventories Programme, Inter-Governmental Panel on Climate Change, 2004-2006*.
- Frost, G. V., & Epstein, H. E. (2014). Tall shrub and tree expansion in Siberian tundra ecotones since the 1960s. *Global Change Biology*, 20(4), 1264–1277. doi:10.1111/gcb.12406
- Frost, G. V., Epstein, H. E., & Walker, D. A. (2014). Regional and landscape-scale variability of Landsat-observed vegetation dynamics in northwest Siberian tundra. *Environmental Research Letters*, 9(2), 025004. doi:10.1088/1748-9326/9/2/025004
- Gamache, I., & Payette, S. (2005). Latitudinal response of subarctic tree lines to recent climate change in eastern Canada. *Journal of Biogeography*, 32(5), 849–862. doi:10.1111/j.1365-2699.2004.01182.x
- Gobakken, T., & Næsset, E. (2009). Assessing effects of positioning errors and sample plot size on biophysical stand properties derived from airborne laser scanner data. *Canadian Journal of Forest Research*, 39(5), 1036–1052. doi:10.1139/X09-025
- Goetz, S., & Dubayah, R. (2011). Advances in remote sensing technology and implications for measuring and monitoring forest carbon stocks and change. *Carbon Management*, 2(3), 231–244.
- Goetz, S., Epstein, H. E., Bhatt, U. S., Jia, G. J., Kaplan, J. O., Lischke, H., et al. (2010). *Eurasian Arctic Land Cover and Land Use in a Changing Climate*. (G. Gutman & A. Reissell) (pp. 9–36). Dordrecht: Springer Netherlands. doi:10.1007/978-90-481-9118-5_2
- Gonzalez, P., Neilson, R. P., Lenihan, J. M., & Drapek, R. J. (2010). Global patterns in the vulnerability of ecosystems to vegetation shifts due to climate change. *Global Ecology and Biogeography*, 19(6), 755–768. doi:10.1111/j.1466-8238.2010.00558.x
- Groisman, P., & Soja, A. J. (2009). Ongoing climatic change in Northern Eurasia: justification for expedient research. *Environmental Research Letters*, 4(4), 045002. doi:10.1088/1748-9326/4/4/045002
- Gruber, S. (2012). Derivation and analysis of a high-resolution estimate of global permafrost zonation. *The Cryosphere*, 6(1), 221–233. doi:10.5194/tc-6-221-2012
- Hall, F. G., Bergen, K., Blair, J. B., Dubayah, R., Houghton, R., Hurtt, G., et al. (2011). Characterizing 3D vegetation structure from space: Mission requirements. *Remote Sensing of Environment*, 115(11), 2753–2775. doi:10.1016/j.rse.2011.01.024

- Hansen, M. C., Potapov, P. V., Moore, R., Hancher, M., Turubanova, S. A., Tyukavina, A., et al. (2013). High-Resolution Global Maps of 21st-Century Forest Cover Change. *Science*, 342(6160), 850–853. doi:10.1126/science.1244693
- Hansen-Bristow, K. J., & Ives, J. D. (1985). Composition, Form, and Distribution of the Forest-Alpine Tundra Ecotone, Indian Peaks, Colorado, USA (Zusammensetzung, Form und Verbreitung des Übergangssaumes zwischen der Waldstufe und der alpinen Tundrastufe im Indian Peaks Gebiet, Front Range, Colorado, USA). *Erdkunde*, 286–295.
- Hardy, J. P., Davis, R. E., Jordan, R., Ni, W., & Woodcock, C. E. (1998). Snow ablation modelling in a mature aspen stand of the boreal forest. *Hydrological Processes*, 12(1011), 1763–1778.
- Harper, K. A., Danby, R. K., De Fields, D. L., Lewis, K. P., Trant, A. J., Starzomski, B. M., et al. (2011). Tree spatial pattern within the forest–tundra ecotone: a comparison of sites across Canada. *Canadian Journal of Forest Research*, 41(3), 479–489. doi:10.1139/X10-221
- Harsch, M. A., & Bader, M. Y. (2011). Treeline form - a potential key to understanding treeline dynamics. *Global Ecology and Biogeography*, 20(4), 582–596. doi:10.1111/j.1466-8238.2010.00622.x
- Harsch, M., Hulme, P., McGlone, M., & Duncan, R. (2009). Are treelines advancing? A global meta-analysis of treeline response to climate warming. *Ecology Letters*, 12(10), 1040–1049.
- Haugo, R. D., Halpern, C. B., & Bakker, J. D. (2011). Landscape context and long-term tree influences shape the dynamics of forest-meadow ecotones in mountain ecosystems. *Ecosphere*, 2(8), 91. doi:10.1890/ES11-00110.1
- Heiskanen, J. (2006). Estimating aboveground tree biomass and leaf area index in a mountain birch forest using ASTER satellite data. *International Journal of Remote Sensing*, 27(6), 1135–1158. doi:10.1080/01431160500353858
- Hensley, S., Oveisgharan, S., Saatchi, S., Simard, M., Ahmed, R., & Haddad, Z. (2014). An Error Model for Biomass Estimates Derived From Polarimetric Radar Backscatter. *IEEE Transactions on Geoscience and Remote Sensing*, 52(7), 4065–4082.
- Herzfeld, U. C., McDonald, B. W., Wallin, B. F., Neumann, T. A., Markus, T., Brenner, A., & Field, C. (2012). Algorithm for detection of ground and canopy cover in micropulse photon-counting lidar altimeter data in preparation for the ICESat-2 mission.
- Hieu Duong, Lindenbergh, R., Pfeifer, N., & Vosselman, G. (2009). ICESat Full-Waveform Altimetry Compared to Airborne Laser Scanning Altimetry Over The Netherlands. *IEEE Transactions on Geoscience and Remote Sensing*, 47(10), 3365–3378. doi:10.1109/TGRS.2009.2021468
- Hirschmugl, M., Ofner, M., Raggam, J., & Schardt, M. (2007). Single tree detection in very high resolution remote sensing data. *Remote Sensing of Environment*, 110(4), 533–544.
- Hobi, M. L., & Ginzler, C. (2012). Accuracy Assessment of Digital Surface Models Based on WorldView-2 and ADS80 Stereo Remote Sensing Data. *Sensors*, 12(12), 6347–6368. doi:10.3390/s120506347
- Hodgson, M. E., & Bresnahan, P. (2004). Accuracy of airborne lidar-derived elevation: empirical assessment and error budget. *Photogrammetric Engineering & Remote Sensing*, 70(3), 331–340.
- Hofgaard, A., & Harper, K. A. (2011). Tree recruitment, growth, and distribution at the circumpolar forest–tundra transition: introduction. *Canadian Journal of Forest Research*, 41(3), 435–436. doi:10.1139/X10-238
- Hofgaard, A., Dalen, L., & Hytteborn, H. (2009). Tree recruitment above the treeline and potential for climate-driven treeline change. *Journal of Vegetation Science*, 20(6), 1133–1144.
- Hofgaard, A., Harper, K. A., & Golubeva, E. (2012). The role of the circumpolar forest–tundra ecotone for Arctic biodiversity. *Biodiversity*, 13(3-4), 174–181. doi:10.1080/14888386.2012.700560
- Hofgaard, A., Rees, G., Tømmervik, H., Tutubalina, O., Golubeva, E., Lukina, N., et al. (2010). Role of disturbed vegetation in mapping the boreal zone in northern Eurasia. *Applied Vegetation Science*, 13(4), 460–472. doi:10.1111/j.1654-109X.2010.01086.x
- Hofgaard, A., Tømmervik, H., Rees, G., & Hanssen, F. (2013). Latitudinal forest advance in northernmost Norway since the early 20th century. *Journal of Biogeography*, 40(5), 938–949.

doi:10.1111/jbi.12053

- Hollinger, D. Y., Goltz, S. M., Davidson, E. A., Lee, J. T., TU, K., & Valentine, H. T. (1999). Seasonal patterns and environmental control of carbon dioxide and water vapour exchange in an ecotonal boreal forest. *Global Change Biology*, 5, 891–902.
- Holtmeier, F. K. (2009). *Mountain Timberlines: Ecology, Patchiness and Dynamics*. Netherlands: Kluwer Academic Publishers.
- Holtmeier, F.-K., & Broll, G. (2005). Sensitivity and response of northern hemisphere altitudinal and polar treelines to environmental change at landscape and local scales. *Global Ecology and Biogeography*, 14(5), 395–410.
- Holtmeier, F.-K., & Broll, G. (2007). Treeline advance - driving processes and adverse factors. *Landscape Online*, 1–32. doi:10.3097/LO.200701
- Holtmeier, K.-F., & Broll, G. (2010). Altitudinal and polar treelines in the northern hemisphere Causes and response to climate change (Obere und polare Baumgrenze auf der nördlichen Hemisphäre Ursachen und Antwort auf den Klimawandel). *Polarforschung*, 79(3), 139–153.
- Huaguo, H., & Biao, C. (2011). Experiment on extracting forest canopy height from Worldview-2 (Vol. 4, pp. 2614–2617). Presented at the Fuzzy Systems and Knowledge Discovery (FSKD), 2011 Eighth International Conference on. doi:10.1109/FSKD.2011.6019949
- Huang, W., Sun, G., Dubayah, R., Cook, B., Montesano, P., Ni, W., & Zhang, Z. (2013). Remote Sensing of Environment. *Remote Sensing of Environment*, 134(C), 319–332. doi:10.1016/j.rse.2013.03.017
- Hufkens, K., Scheunders, P., & Ceulemans, R. (2009). Ecotones in vegetation ecology: methodologies and definitions revisited. *Ecological Research*, 24(5), 977–986. doi:10.1007/s11284-009-0584-7
- Hyde, P., Dubayah, R., Walker, W., Blair, J., Hofton, M., & Hunsaker, C. (2006). Mapping forest structure for wildlife habitat analysis using multi-sensor (LiDAR, SAR/InSAR, ETM plus , Quickbird) synergy. *Remote Sensing of Environment*, 102(1-2), 63–73. doi:10.1016/j.rse.2006.01.021
- Iida, S., Ohta, T., Matsumoto, K., Nakai, T., Kuwada, T., Kononov, A. V., et al. (2009). Evapotranspiration from understory vegetation in an eastern Siberian boreal larch forest. *Agricultural and Forest Meteorology*, 149(6-7), 1129–1139. doi:10.1016/j.agrformet.2009.02.003
- Jacobsen, K. (2003). DEM generation from satellite data. *EARSeL Ghent*, 273–276.
- Jenkins, J., Chojnacky, D., Heath, L., & Birdsey, R. (2003). National-scale biomass estimators for United States tree species. *Forest Science*, 49(1), 12–35.
- Johansen, K., Sohlbach, M., Sullivan, B., Stringer, S., Peasley, D., & Phinn, S. (2014). Mapping Banana Plants from High Spatial Resolution Orthophotos to Facilitate Plant Health Assessment. *Remote Sensing*, 6(9), 8261–8286. doi:10.3390/rs6098261
- Jorgenson, M. T., Romanovsky, V., Harden, J., Shur, Y., O'Donnell, J., Schuur, E. A. G., et al. (2010). Resilience and vulnerability of permafrost to climate change This article is one of a selection of papers from The Dynamics of Change in Alaska's Boreal Forests: Resilience and Vulnerability in Response to Climate Warming. *Canadian Journal of Forest Research*, 40(7), 1219–1236. doi:10.1139/X10-060
- Kaartinen, H., Hyypä, J., Yu, X., Vastaranta, M., Hyypä, H., Kukko, A., et al. (2012). An International Comparison of Individual Tree Detection and Extraction Using Airborne Laser Scanning. *Remote Sensing*, 4(12), 950–974. doi:10.3390/rs4040950
- Kajimoto, T., Osawa, A., Usoltsev, V. A., & Abaimov, A. P. (2009). Biomass and Productivity of Siberian Larch Forest Ecosystems. In *Ecological Studies* (Vol. 209, pp. 99–122). Dordrecht: Ecological Studies. doi:10.1007/978-1-4020-9693-8_6
- Kellndorfer, J. M., Walker, W. S., LaPoint, E., Kirsch, K., Bishop, J., & Fiske, G. (2010). Statistical fusion of lidar, InSAR, and optical remote sensing data for forest stand height characterization: A regional-scale method based on LVIS, SRTM, Landsat ETM plus , and ancillary data sets. *Journal of Geophysical Research-Biogeosciences*, 115, G00E08. doi:10.1029/2009JG000997
- Kent, M., Gill, W. J., Weaver, R. E., & Armitage, R. P. (1997). Landscape and plant community boundaries in biogeography. *Progress in Physical Geography*, 21(3), 315–353.
- Kharuk, V. I., Dvinskaya, M. L., Ranson, K. J., & Im, S. T. (2005). Expansion of evergreen conifers to

- the larch-dominated zone and climatic trends. *Russian Journal of Ecology*, 36(3), 164–170.
- Kharuk, V. I., Ranson, K. J., Dvinskaya, M. L., & Im, S. T. (2011). Wildfires in northern Siberian larch dominated communities. *Environmental Research Letters*, 6(4), 045208. doi:10.1088/1748-9326/6/4/045208
- Kharuk, V. I., Ranson, K. J., Im, S. T., & Naurzbaev, M. M. (2006). Forest-tundra larch forests and climatic trends. *Russian Journal of Ecology*, 37(5), 291–298. doi:10.1134/S1067413606050018
- Kharuk, V., Dvinskaya, M. L., & Ranson, K. J. (2013a). Fire return intervals within the northern boundary of the larch forest in Central Siberia. *International Journal of Wildland Fire*, 22(2), 207. doi:10.1071/WF11181
- Kharuk, V., Ranson, K. J., Im, S. T., Oskorbin, P. A., Dvinskaya, M. L., & Ovchinnikov, D. V. (2013b). Tree-Line Structure and Dynamics at the Northern Limit of the Larch Forest: Anabar Plateau, Siberia, Russia. *Arctic, Antarctic, and Alpine Research*, 45(4), 526–537. doi:10.1657/1938-4246-45.4.526
- Kharuk, V., Ranson, K., & Dvinskaya, M. L. (2007). Evidence of Evergreen Conifer Invasion into Larch Dominated Forests During Recent Decades in Central Siberia. *Eurasian Journal of Forest Research*, 10(2), 163–171.
- Kirdyanov, A. V., Hagedorn, F., Knorre, A. A., Fedotova, E., Vaganov, E. A., Naurzbaev, M. M., et al. (2011). 20th century tree-line advance and vegetation changes along an altitudinal transect in the Putorana Mountains, northern Siberia. *Boreas*, 41(1), 56–67. doi:10.1111/j.1502-3885.2011.00214.x
- Kobayashi, H., Delbart, N., Suzuki, R., & Kushida, K. (2010). A satellite-based method for monitoring seasonality in the overstory leaf area index of Siberian larch forest. *Journal of Geophysical Research*, 115(G1), G01002. doi:10.1029/2009JG000939
- Kobayashi, H., Suzuki, R., & Kobayashi, S. (2007). Reflectance seasonality and its relation to the canopy leaf area index in an eastern Siberian larch forest: Multi-satellite data and radiative transfer analyses. *Remote Sensing of Environment*, 106(2), 238–252.
- Koetz, B., Morsdorf, F., Sun, G., Ranson, K., Itten, K., & Allgower, B. (2006). Inversion of a lidar waveform model for forest biophysical parameter estimation. *Geoscience and Remote Sensing Letters, IEEE*, 3(1), 49–53.
- Lawrence, D. M., & Swenson, S. C. (2011). Permafrost response to increasing Arctic shrub abundance depends on the relative influence of shrubs on local soil cooling versus large-scale climate warming. *Environmental Research Letters*, 6(4), 045504. doi:10.1088/1748-9326/6/4/045504
- Le Toan, T., Quegan, S., Davidson, M. W. J., Balzter, H., Paillou, P., Papathanassiou, K., et al. (2011). Remote Sensing of Environment. *Remote Sensing of Environment*, 115(11), 2850–2860. doi:10.1016/j.rse.2011.03.020
- Lefsky, M. A. (2010). A global forest canopy height map from the Moderate Resolution Imaging Spectroradiometer and the Geoscience Laser Altimeter System. *Geophysical Research Letters*, 37(15), L15401. doi:10.1029/2010GL043622
- Lefsky, M. A., Harding, D. J., Keller, M., Cohen, W. B., Carabajal, C. C., Del Bom Espirito-Santo, F., et al. (2005). Estimates of forest canopy height and aboveground biomass using ICESat. *Geophysical Research Letters*, 32(22).
- Lefsky, M. A., Harding, D., Cohen, W., Parker, G., & Shugart, H. (1999). Surface lidar remote sensing of basal area and biomass in deciduous forests of eastern Maryland, USA. *Remote Sensing of Environment*, 67(1), 83–98.
- Lefsky, M., Cohen, W., Parker, G., & Harding, D. (2002). Lidar remote sensing for ecosystem studies. *Bioscience*, 52(1), 19–30.
- Li, R., Niu, X., Liu, C., Wu, B., & Deshpande, S. (2009). Impact of imaging geometry on 3D geopositioning accuracy of stereo IKONOS imagery. *Photogramm. Eng. Remote Sens.*, 75(9), 1119–1125.
- Li, R., Zhou, F., Niu, X., & Di, K. (2007). Integration of IKONOS and QuickBird imagery for geopositioning accuracy analysis. *Photogrammetric Engineering & Remote Sensing*, 73(9), 1067.
- Liebs, S., Snyder, P. K., & Harding, K. J. (2011). The effects of boreal forest expansion on the summer

- Arctic frontal zone. *Climate Dynamics*, 38(9-10), 1805–1827. doi:10.1007/s00382-011-1064-7
- Liu, K. B. (1990). Holocene paleoecology of the boreal forest and Great Lakes-St. Lawrence forest in northern Ontario. *Ecological Monographs*, 60(2), 179–212.
- Lloyd, A. H., Bunn, A. G., & Berner, L. T. (2011). A latitudinal gradient in tree growth response to climate warming in the Siberian taiga. *Global Change Biology*, 17(5), 1935–1945. doi:10.1111/j.1365-2486.2010.02360.x
- Lloyd, A. H., Rupp, T. S., Fastie, C. L., & Starfield, A. M. (2002). Patterns and dynamics of treeline advance on the Seward Peninsula, Alaska. *Journal of Geophysical Research*, 108(D2), 8161. doi:10.1029/2001JD000852
- Loranty, M. M., & Goetz, S. J. (2012). Shrub expansion and climate feedbacks in Arctic tundra. *Environmental Research Letters*, 7(1), 011005. doi:10.1088/1748-9326/7/1/011005
- Loranty, M. M., Berner, L. T., Goetz, S. J., Jin, Y., & Randerson, J. T. (2013). Vegetation controls on northern high latitude snow-albedo feedback: observations and CMIP5 model predictions. *Global Change Biology*, 20(2), 594–606. doi:10.1111/gcb.12391
- Loranty, M. M., Goetz, S. J., & Beck, P. S. A. (2011). Tundra vegetation effects on pan-Arctic albedo. *Environmental Research Letters*, 6, 024014.
- Los, S. O., Rosette, J. A. B., Kljun, N., North, P. R. J., Chasmer, L., Suárez, J. C., et al. (2012). Vegetation height and cover fraction between 60° S and 60° N from ICESat GLAS data. *Geoscientific Model Development*, 5(2), 413–432. doi:10.5194/gmd-5-413-2012
- Lu, D., Chen, Q., Wang, G., Moran, E., Batistella, M., Zhang, M., et al. (2012). Aboveground Forest Biomass Estimation with Landsat and LiDAR Data and Uncertainty Analysis of the Estimates. *International Journal of Forestry Research*, 2012(2), 1–16. doi:10.1109/TGRS.2004.831889
- MacDonald, G. M., Edwards, T. W. D., Moser, K. A., Pienitz, R., & Smol, J. P. (1993). Rapid response of treeline vegetation and lakes to past climate warming. *Nature*, 361(6409), 243–246. doi:10.1038/361243a0
- MacDonald, G. M., Kremenetski, K. V., & Beilman, D. W. (2008). Climate change and the northern Russian treeline zone. *Philosophical Transactions of the Royal Society B: Biological Sciences*, 363(1501), 2283–2299. doi:10.1098/rstb.2007.2200
- MacDonald, G., Velichko, A., Kremenetski, C., Borisova, O., Goleva, A., Andreev, A., et al. (2000). Holocene treeline history and climate change across Northern Eurasia. *Quaternary Research*, 53, 302–311.
- Macias-Fauria, M., Forbes, B. C., Zetterberg, P., & Kumpula, T. (2012). Eurasian Arctic greening reveals teleconnections and the potential for structurally novel ecosystems. *Nature Climate Change*, 2(8), 613–618. doi:10.1038/nclimate1558
- Malanson, G. P., Zeng, Y., & Walsh, S. J. (2006). Complexity at advancing ecotones and frontiers. *Environment and Planning A*, 38(4), 619–632. doi:10.1068/a37340
- Mascaro, J., Detto, M., Asner, G. P., & Muller-Landau, H. C. (2011). Evaluating uncertainty in mapping forest carbon with airborne LiDAR. *Remote Sensing of Environment*, 115(12), 3770–3774. doi:10.1016/j.rse.2011.07.019
- Mathisen, I. E., Mikheeva, A., Tutubalina, O. V., Aune, S., & Hofgaard, A. (2013). Fifty years of tree line change in the Khibiny Mountains, Russia: advantages of combined remote sensing and dendroecological approaches. *Applied Vegetation Science*, 17(1), 6–16. doi:10.1111/avsc.12038
- Mazepa, V. S., & Devi, N. M. (2007). Development of multistemmed life forms of Siberian larch as an indicator of climate change in the timberline ecotone of the Polar Urals. *Russian Journal of Ecology*, 38(6), 440–443. doi:10.1134/S1067413607060112
- McDonald, K. C., Dobson, M. C., & Ulaby, F. T. (1990). Using MIMICS to model L-band multiangle and multitemporal backscatter from a walnut orchard. *IEEE Transactions on Geoscience and Remote Sensing*, 28(4), 477–491.
- McGill, M., Markus, T., Scott, V. S., & Neumann, T. (2013). The Multiple Altimeter Beam Experimental Lidar (MABEL): An Airborne Simulator for the ICESat-2 Mission. *Journal of Atmospheric and Oceanic Technology*, 30(2), 345–352. doi:10.1175/JTECH-D-12-00076.1

- McMahon, S. M., Dietze, M. C., Hersh, M. H., Moran, E. V., & Clark, J. S. (2009). A Predictive Framework to Understand Forest Responses to Global Change. *Annals of the New York Academy of Sciences*, 1162(1), 221–236. doi:10.1111/j.1749-6632.2009.04495.x
- Mette, T., Papathanassiou, K., & Hajnsek, I. (2004). Biomass estimation from polarimetric SAR interferometry over heterogeneous forest terrain. *Geoscience and Remote Sensing Symposium, 2004. IGARSS'04. Proceedings. 2004 IEEE International*, 1, 511–514.
- Miyahara, M., Takenaka, C., Tomioka, R., & Ohta, T. (2011). Root responses of Siberian larch to different soil water conditions. *Hydrological Research Letters*, 5, 93–97. doi:10.3178/hrl.5.93
- Montesano, P. M., Cook, B. D., Sun, G., Simard, M., Nelson, R. F., Ranson, K. J., et al. (2013). Achieving accuracy requirements for forest biomass mapping: A spaceborne data fusion method for estimating forest biomass and LiDAR sampling error. *Remote Sensing of Environment*, 130(C), 153–170. doi:10.1016/j.rse.2012.11.016
- Montesano, P. M., Nelson, R. F., Dubayah, R. O., Sun, G., Cook, B. D., Ranson, K., et al. (2014a). The uncertainty of biomass estimates from LiDAR and SAR across a boreal forest structure gradient. *Remote Sensing of Environment*, 154, 398–407. doi:10.1016/j.rse.2014.01.027
- Montesano, P. M., Rosette, J., Sun, G., North, P., Nelson, R. F., Dubayah, R. O., et al. (2015). The uncertainty of biomass estimates from modeled ICESat-2 returns across a boreal forest gradient. *Remote Sensing of Environment*, 158, 95–109. doi:10.1016/j.rse.2014.10.029
- Montesano, P., Nelson, R., Sun, G., Margolis, H., Kerber, A., & Ranson, K. (2009). MODIS tree cover validation for the circumpolar taiga-tundra transition zone. *Remote Sensing of Environment*, 113(10), 2130–2141.
- Montesano, P., Sun, G., Dubayah, R., & Ranson, K. (2014b). The Uncertainty of Plot-Scale Forest Height Estimates from Complementary Spaceborne Observations in the Taiga-Tundra Ecotone. *Remote Sensing*, 6(10), 10070–10088. doi:10.3390/rs61010070
- Moratto, Z. M., Broxton, M. J., Beyer, R. A., Lundy, M., & Husmann, K. (2010). Ames Stereo Pipeline, NASA's open source automated stereogrammetry software, 41, 2364.
- Morton, D. C., Nagol, J., Carabajal, C. C., Rosette, J., Palace, M., Cook, B. D., et al. (2014). Amazon forests maintain consistent canopy structure and greenness during the dry season. *Nature*, 506(7487), 221–224. doi:10.1038/nature13006
- Myers-Smith, I. H., Forbes, B. C., Wilmsking, M., Hallinger, M., Lantz, T., Blok, D., et al. (2011). Shrub expansion in tundra ecosystems: dynamics, impacts and research priorities. *Environmental Research Letters*, 6(4), 045509. doi:10.1088/1748-9326/6/4/045509
- Naurzbaev, M. M., & Vaganov, E. A. (2000). Variation of early summer and annual temperature in east Taymir and Putoran (Siberia) over the last two millennia inferred from tree rings. *Journal of Geophysical Research-Atmospheres*, 105(D6), 7317–7326.
- Naurzbaev, M. M., Hughes, M. K., & Vaganov, E. A. (2004). Tree-ring growth curves as sources of climatic information. *Quaternary Research*, 62(2), 126–133. doi:10.1016/j.yqres.2004.06.005
- Neigh, C. S., Masek, J. G., & Nickeson, J. E. (2013a). High-Resolution Satellite Data Open for Government Research. *Eos, Transactions American Geophysical Union*, 94(13), 121–123.
- Neigh, C. S., Nelson, R. F., Ranson, K. J., Margolis, H. A., Montesano, P. M., Sun, G., et al. (2013b). Taking stock of circumboreal forest carbon with ground measurements, airborne and spaceborne LiDAR. *Remote Sensing of Environment*, 137, 274–287. doi:10.1016/j.rse.2013.06.019
- Neigh, C., Masek, J., Bourget, P., Cook, B., Huang, C., Rishmawi, K., & Zhao, F. (2014). Deciphering the Precision of Stereo IKONOS Canopy Height Models for US Forests with G-LiHT Airborne LiDAR. *Remote Sensing*, 6(3), 1762–1782. doi:10.3390/rs6031762
- Nelson, R. (2010). Model effects on GLAS-based regional estimates of forest biomass and carbon. *International Journal of Remote Sensing*, 31(5), 1359–1372.
- Nelson, R., Krabill, W., & Tonelli, J. (1988). Estimating forest biomass and volume using airborne laser data. *Remote Sensing of Environment*, 24(2), 247–267.
- Nelson, R., Ranson, K. J., Sun, G., Kimes, D. S., Kharuk, V., & Montesano, P. (2009). Estimating Siberian timber volume using MODIS and ICESat/GLAS. *Remote Sensing of Environment*, 113(3),

- 691–701. doi:10.1016/j.rse.2008.11.010
- Nelson, R., Ståhl, G., Holm, S., Gregoire, T., Næsset, E., & Gobakken, T. (2010). Using airborne & space lidars for large-area inventory. *Geoscience and Remote Sensing Symposium (IGARSS), 2010 IEEE International*, 2463–2466.
- Ni, Wenge, & Woodcock, C. E. (2000). Effect of canopy structure and the presence of snow on the albedo of boreal conifer forests. *Journal of Geophysical Research: Atmospheres (1984–2012)*, *105*(D9), 11879–11888.
- Ni, Wenge, Li, X., Woodcock, C. E., Roujean, J. L., & Davis, R. E. (1997). Transmission of solar radiation in boreal conifer forests: Measurements and models. *Journal of Geophysical Research: Atmospheres (1984–2012)*, *102*(D24), 29555–29566.
- Ni, Wenjian, Ranson, K. J., Zhang, Z., & Sun, G. (2014). Remote Sensing of Environment. *Remote Sensing of Environment*, *149*(C), 47–57. doi:10.1016/j.rse.2014.04.001
- Ni-Meister, W., & Gao, H. (2011). Assessing the impacts of vegetation heterogeneity on energy fluxes and snowmelt in boreal forests. *Journal of Plant Ecology*, *4*(1-2), 37–47. doi:10.1093/jpe/rtr004
- Ni-Meister, W., Jupp, D., & Dubayah, R. (2001). Modeling lidar waveforms in heterogeneous and discrete canopies. *IEEE Transactions on Geoscience and Remote Sensing*, *39*(9), 1943–1958.
- North, P. R. J. (1996). Three-dimensional forest light interaction model using a Monte Carlo method. *Geoscience and Remote Sensing, IEEE Transactions on*, *34*(4), 946–956.
- North, P. R. J., Rosette, J. A. B., Suárez, J. C., & Los, S. O. (2010). A Monte Carlo radiative transfer model of satellite waveform LiDAR. *International Journal of Remote Sensing*, *31*(5), 1343–1358. doi:10.1080/01431160903380664
- Næsset, E. (2011). Estimating above-ground biomass in young forests with airborne laser scanning. *International Journal of Remote Sensing*, *32*(2), 473–501. doi:10.1080/01431160903474970
- Næsset, E., & Gobakken, T. (2008). Estimation of above- and below-ground biomass across regions of the boreal forest zone using airborne laser. *Remote Sensing of Environment*, *112*(6), 3079–3090. doi:10.1016/j.rse.2008.03.004
- Næsset, E., & Nelson, R. (2007). Using airborne laser scanning to monitor tree migration in the boreal–alpine transition zone. *Remote Sensing of Environment*, *110*(3), 357–369. doi:10.1016/j.rse.2007.03.004
- Næsset, E., Gobakken, T., Solberg, S., Gregoire, T. G., Nelson, R., Ståhl, G., & Weydahl, D. (2011). Model-assisted regional forest biomass estimation using LiDAR and InSAR as auxiliary data: A case study from a boreal forest area. *Remote Sensing of Environment*, *115*(12), 3599–3614. doi:10.1016/j.rse.2011.08.021
- Olson, D. M., Dinerstein, E., Wikramanayake, E. D., Burgess, N. D., Powell, G. V. N., Underwood, E. C., et al. (2001). Terrestrial Ecoregions of the World: A New Map of Life on Earth. *Bioscience*, *11*(51), 933–938.
- Osawa, A., & Kajimoto, T. (2009). Development of Stand Structure in Larch Forests. In *Ecological Studies* (Vol. 209, pp. 123–148). Dordrecht: Ecological Studies. doi:10.1007/978-1-4020-9693-8_7
- Ott, L., & Longnecker, M. (2010). *An introduction to statistical methods and data analysis* (6 ed.). Brooks/Cole.
- Overpeck, J., Hughen, K., Hardy, D., Bradley, R., Case, R., Douglas, M., et al. (1997). Arctic Environmental Change of the Last Four Centuries. *Science*, *278*(5341), 1251–1256. doi:10.2307/2894183?ref=no-x-route:8fb7ddd8a0b762b774b9c61432590b64
- Payette, S., & Gagnon, R. (1985). Late Holocene deforestation and tree regeneration in the forest-tundra of Quebec. *Nature*, *313*(14), 570–572.
- Payette, S., Eronen, M., & Jasinski, J. (2002). The circumboreal tundra-taiga interface: Late Pleistocene and Holocene changes. *Ambio*, 15–22.
- Payette, S., Fortin, M. J., & Gamache, I. (2001). The subarctic forest-tundra: the structure of a biome in a changing climate. *Bioscience*, *51*(9), 709–718.
- Pearson, R. G., Phillips, S. J., Lorant, M. M., Beck, P. S. A., Damoulas, T., Knight, S. J., & Goetz, S. J. (2013). Shifts in Arctic vegetation and associated feedbacks under climate change. *Nature Climate*

- Change*, 3(4), 1–5. doi:10.1038/nclimate1858
- Peterson, B., Nelson, K., & Wylie, B. (2013). Towards integration of GLAS into a national fuel mapping program. *Photogrammetric Engineering & Remote Sensing*, 79(2), 175–183.
- Petrou, Z. I., Manakos, I., Stathaki, T., Tarantino, C., Adamo, M., & Blonda, P. (2014). A vegetation height classification approach based on texture analysis of a single VHR image. *IOP Conference Series: Earth and Environmental Science*, 17, 012210. doi:10.1088/1755-1315/17/1/012210
- Popescu, S. C., Zhao, K., Neuenschwander, A., & Lin, C. (2011). Satellite lidar vs. small footprint airborne lidar: Comparing the accuracy of aboveground biomass estimates and forest structure metrics at footprint level. *Remote Sensing of Environment*, 1–12. doi:10.1016/j.rse.2011.01.026
- Post, E., Forchhammer, M. C., Bret-Harte, M. S., Callaghan, T. V., Christensen, T. R., Elberling, B., et al. (2009). Ecological dynamics across the Arctic associated with recent climate change. *Science*, 325(5946), 1355–1358.
- Praks, J., Hallikainen, M., Antropov, O., & Molina, D. (2012). Boreal forest tree height estimation from interferometric TanDEM-X images. *IEEE International Conference on Geoscience and Remote Sensing Symposium, 2012*, 1262–1265.
- R Development Core Team. (2012). R: A language and environment for statistical computing. Vienna, Austria: R Foundation for Statistical Computing. Retrieved from <http://www.R-project.org/>
- Raggam, H., Franke, M., Ofner, M., & Gutjahr, K. (2005). Accuracy assessment of vegetation height mapping using spaceborne IKONOS as well as aerial UltraCam stereo images. *Proceedings of the EARSeL 3D Remote Sensing Workshop, Porto, Portugal, 6–11 June 2005*, 1–12.
- Ranson, K. J., Montesano, P. M., & Nelson, R. (2011). Object-based mapping of the circumpolar taiga–tundra ecotone with MODIS tree cover. *Remote Sensing of Environment*, 115(12), 3670–3680. doi:10.1016/j.rse.2011.09.006
- Ranson, K., & Sun, G. (1997). An evaluation of AIRSAR and SIR-C/X-SAR images for mapping northern forest attributes in Maine, USA. *Remote Sensing of Environment*, 59(2), 203–222.
- Ranson, K., Sun, G., Kharuk, V., & Kovacs, K. (2004). Assessing tundra–taiga boundary with multi-sensor satellite data. *Remote Sensing of Environment*, 93(3), 283–295.
- Risser, P. G. (1995). The status of the science examining ecotones. *Bioscience*, 45(5), 318–325.
- Ropars, P., & Boudreau, S. (2012). Shrub expansion at the forest–tundra ecotone: spatial heterogeneity linked to local topography. *Environmental Research Letters*, 7(1), 015501. doi:10.1088/1748-9326/7/1/015501
- Rosen, P. A., Hensley, S., Wheeler, K., Sadowy, G., Miller, T., Shaffer, S., et al. (2006). UAVSAR: a new NASA airborne SAR system for science and technology research. *Proceedings on the IEEE Conference on Radar*, 8 pp.
- Rosenqvist, A., Shimada, M., Ito, N., & Watanabe, M. (2013). ALOS PALSAR: A Pathfinder Mission for Global-Scale Monitoring of the Environment. *IEEE Transactions on Geoscience and Remote Sensing*, 45(11), 3307–3316. doi:10.1109/TGRS.2007.901027
- Rosette, J., Field, C., Nelson, R., DeCola, P., & Cook, B. (2011). A new photon-counting lidar system for vegetation analysis (pp. 1–8). Presented at the Proceedings of the Silvilaser 2011 Conference.
- Rosette, J., North, P. R. J., Rubio-Gil, J., Cook, B., Los, S., Suarez, J., et al. (2013). Evaluating Prospects for Improved Forest Parameter Retrieval From Satellite LiDAR Using a Physically-Based Radiative Transfer Model. *IEEE Journal of Selected Topics in Applied Earth Observations and Remote Sensing*, 6(1), 45–53. doi:10.1109/JSTARS.2013.2244199
- Rosette, J., North, P., Suarez, J., & Los, S. (2010). Uncertainty within satellite LiDAR estimations of vegetation and topography. *International Journal of Remote Sensing*, 31(5), 1325–1342.
- Roy-Léveillé, P., Burn, C. R., & McDonald, I. D. (2014). Vegetation-Permafrost Relations within the Forest-Tundra Ecotone near Old Crow, Northern Yukon, Canada. *Permafrost and Periglacial Processes*, 25(2), 127–135.
- Santoro, M., Cartus, O., Fransson, J., Shvidenko, A., McCallum, I., Hall, R., et al. (2013). Estimates of Forest Growing Stock Volume for Sweden, Central Siberia, and Québec Using Envisat Advanced Synthetic Aperture Radar Backscatter Data. *Remote Sensing*, 5(9), 4503–4532.

doi:10.3390/rs5094503

- Santoro, M., Fransson, J., Eriksson, L., Magnusson, M., Ulander, L., & Olsson, H. (2009). Signatures of ALOS PALSAR L-band backscatter in Swedish forest. *Geoscience and Remote Sensing, IEEE Transactions on*, 47(12), 4001–4019.
- Schaefer, K., Zhang, T., Bruhwiler, L., & Barrett, A. P. (2011). Amount and timing of permafrost carbon release in response to climate warming. *Tellus B*, 63(2), 165–180. doi:10.1111/j.1600-0889.2011.00527.x
- Schauffler, M., Jacobson, G. L., Pugh, A. L., & Norton, S. A. (1996). Influence of vegetational structure on capture of salt and nutrient aerosols in a Maine peatland. *Ecological Applications*, 6(1), 263–268.
- Schulze, E. D., Wirth, C., Mollicone, D., Lüpke, von, N., Ziegler, W., Achard, F., et al. (2012). Factors promoting larch dominance in central Siberia: fire versus growth performance and implications for carbon dynamics at the boundary of evergreen and deciduous conifers. *Biogeosciences*, 9(4), 1405–1421. doi:10.5194/bg-9-1405-2012
- Selkowitz, D. J., Green, G., Peterson, B., & Wylie, B. (2012). A multi-sensor lidar, multi-spectral and multi-angular approach for mapping canopy height in boreal forest regions. *Remote Sensing of Environment*, 121(C), 458–471. doi:10.1016/j.rse.2012.02.020
- Shamsoddini, A., & Trinder, J. C. (2012). Edge-detection-based filter for SAR speckle noise reduction. *International Journal of Remote Sensing*, 33(7), 2296–2320. doi:10.1080/01431161.2011.614286
- Shimada, M., Itoh, T., Motooka, T., Watanabe, M., Shiraiishi, T., Thapa, R., & Lucas, R. (2014). Remote Sensing of Environment. *Remote Sensing of Environment*, 155(C), 13–31. doi:10.1016/j.rse.2014.04.014
- Shiyatov, S. G., & Mazepa, V. S. (2012). Climate-driven dynamics of the forest-tundra vegetation in the Polar Ural Mountains. *Contemporary Problems of Ecology*, 4(7), 758–768. doi:10.1134/S1995425511070071
- Shuman, J. K., Shugart, H. H., & O'Halloran, T. L. (2011). Sensitivity of Siberian larch forests to climate change. *Global Change Biology*, 17(7), 2370–2384.
- Simard, M., Pinto, N., & Fisher, J. (2011). Mapping forest canopy height globally with spaceborne lidar. *Journal of Geophysical Research*, 116(G04021).
- Small, D. (2011). Flattening Gamma: Radiometric Terrain Correction for SAR Imagery. *Geoscience and Remote Sensing, IEEE Transactions on*, (99), 1–13. doi:10.1109/TGRS.2011.2120616
- Soja, A., Tchebakova, N., French, N., Flannigan, M., Shugart, H., Stocks, B., et al. (2007). Climate-induced boreal forest change: predictions versus current observations. *Global and Planetary Change*, 56(3-4), 274–296.
- Sturm, M., Racine, C., & Tape, K. (2001). Increasing shrub abundance in the Arctic. *Nature*, 411(6837), 546–547.
- Sugimoto, A., Yanagisawa, N., Naito, D., Fujita, N., & Maximov, T. C. (2002). Importance of permafrost as a source of water for plants in east Siberian taiga. *Ecological Research*, 17(4), 493–503. doi:10.1046/j.0912-3814.2002.00506.x
- Sun, G., & Ranson, K. J. (2000). Modeling lidar returns from forest canopies. *IEEE Transactions on Geoscience and Remote Sensing*, 38(6), 2617–2626. doi:10.1109/36.885208
- Sun, G., Ranson, K. J., Guo, Z., Zhang, Z., Montesano, P., & Kimes, D. (2011). Forest biomass mapping from lidar and radar synergies. *Remote Sensing of Environment*, 1–11. doi:10.1016/j.rse.2011.03.021
- Sun, G., Ranson, K. J., Kharuk, V. I., & Kovacs, K. (2004). Changes in the Taiga-Tundra boundary observed with Landsat (Vol. 2, pp. 722–724). Presented at the Geoscience and Remote Sensing Symposium, 2004. IGARSS '04. Proceedings. 2004 IEEE International. doi:10.1109/IGARSS.2004.1368503
- Sun, G., Ranson, K. J., Masek, J., Guo, Z., Pang, Y., Fu, A., & Wang, D. (2008a). Estimation of tree height and forest biomass from GLAS data. *Journal of Forest Planning*, 13, 157–164.
- Sun, G., Ranson, K., Kimes, D., Blair, J., & Kovacs, K. (2008b). Forest vertical structure from GLAS: An evaluation using LVIS and SRTM data. *Remote Sensing of Environment*, 112(1), 107–117. doi:10.1016/j.rse.2006.09.036

- Sveinbjörnsson, B., Hofgaard, A., & Lloyd, A. (2002). Natural causes of the tundra-taiga boundary. *Ambio*, 23–29.
- Swann, A. L., Fung, I. Y., Levis, S., Bonan, G. B., & Doney, S. C. (2010). Changes in Arctic vegetation amplify high-latitude warming through the greenhouse effect. *Proceedings of the National Academy of Sciences*, 107(4), 1295–1300. doi:10.1073/pnas.0913846107
- Tape, K., Sturm, M., & Racine, C. (2006). The evidence for shrub expansion in northern Alaska and the Pan-Arctic. *Global Change Biology*, 12(4), 686–702.
- Tchebakova, N. M., Parfenova, E., & Soja, A. J. (2009). The effects of climate, permafrost and fire on vegetation change in Siberia in a changing climate. *Environmental Research Letters*, 4(4), 045013. doi:10.1088/1748-9326/4/4/045013
- Ter-Mikaelian, M. T., & Korzukhin, M. D. (1997). Biomass equations for sixty-five North American tree species. *Forest Ecology and Management*, 97(1), 1–24.
- Thompson, C., Beringer, J., Chapin, F. S., & Mcguire, A. D. (2004). Structural complexity and land-surface energy exchange along a gradient from arctic tundra to boreal forest. *Journal of Vegetation Science*, 15(3), 397–406.
- Tinkham, W. T., Smith, A. M. S., Hoffman, C., Hudak, A. T., Falkowski, M. J., Swanson, M. E., & Gessler, P. E. (2012). Investigating the influence of LiDAR ground surface errors on the utility of derived forest inventories. *Canadian Journal of Forest Research*, 42(3), 413–422. doi:10.1139/x11-193
- Ueyama, M., Ichii, K., Hirata, R., Takagi, K., Asanuma, J., Machimura, T., et al. (2010). Simulating carbon and water cycles of larch forests in East Asia by the BIOME-BGC model with AsiaFlux data. *Biogeosciences*, 7(3), 959–977.
- Urban, M., Forkel, M., Eberle, J., Hüttich, C., Schmullius, C., & Herold, M. (2014). Pan-Arctic Climate and Land Cover Trends Derived from Multi-Variate and Multi-Scale Analyses (1981–2012). *Remote Sensing*, 6(3), 2296–2316. doi:10.3390/rs6032296
- Urban, T. J., Schutz, B. E., & Neuenschwander, A. L. (2008). A Survey of ICESat Coastal Altimetry Applications: Continental Coast, Open Ocean Island, and Inland River. *Terrestrial, Atmospheric and Oceanic Sciences*, 19(1-2), 1. doi:10.3319/TAO.2008.19.1-2.1(SA)
- Usoltsev, V. A., Koltunova, A. I., Kajimoto, T., Osawa, A., & KOIKE, T. (2002). Geographical gradients of annual biomass production from larch forests in northern Eurasia. *Eurasian Journal of Forest Research*, 5(1), 55–62.
- Vaganov, E. A., & Kirilyanov, A. V. (2009). *Dendrochronology of Larch Trees Growing on Siberian Permafrost*. (A. Osawa, O. A. Zyryanova, Y. Matsuura, T. Kajimoto, & R. W. Wein) (Vol. 209, pp. 347–363). Dordrecht: Ecological Studies. doi:10.1007/978-1-4020-9693-8_18
- Vaganov, E. A., Hughes, M. K., Kirilyanov, A. V., Schweingruber, F. H., & Silkin, P. P. (1999). Influence of snowfall and melt timing on tree growth in subarctic Eurasia. *Nature*, 400(6740), 149–151.
- van Aardt, J., Wynne, R., & Oderwald, R. (2006). Forest volume and biomass estimation using small-footprint lidar-distributional parameters on a per-segment basis. *Forest Science*, 52(6), 636–649.
- Vepakomma, U., St-Onge, B., & Kneeshaw, D. (2011). Response of a boreal forest to canopy opening: assessing vertical and lateral tree growth with multi-temporal lidar data. *Ecological Applications*, 21(1), 99–121.
- Vermote, E. F., Tanré, D., Deuze, J.-L., Herman, M., & Morcette, J.-J. (1997). Second simulation of the satellite signal in the solar spectrum, 6S: An overview. *IEEE Transactions on Geoscience and Remote Sensing*, 35(3), 675–686.
- Virtanen, R., Luoto, M., Rämä, T., Mikkola, K., Hjort, J., Grytnes, J.-A., & Birks, H. J. B. (2010). Recent vegetation changes at the high-latitude tree line ecotone are controlled by geomorphological disturbance, productivity and diversity. *Global Ecology and Biogeography*, 19(6), 810–821. doi:10.1111/j.1466-8238.2010.00570.x
- Walker, D. A., Epstein, H. E., Reynolds, M. K., Kuss, P., Kopecky, M. A., Frost, G. V., et al. (2012). Environment, vegetation and greenness (NDVI) along the North America and Eurasia Arctic

- transects. *Environmental Research Letters*, 7(1), 015504. doi:10.1088/1748-9326/7/1/015504
- Wasser, L., Day, R., Chasmer, L., & Taylor, A. (2013a). Influence of Vegetation Structure on Lidar-derived Canopy Height and Fractional Cover in Forested Riparian Buffers During Leaf-Off and Leaf-On Conditions. *PLoS ONE*, 8(1), e54776. doi:10.1371/journal.pone.0054776.t008
- Wasser, L., Day, R., Chasmer, L., & Taylor, A. (2013b). Influence of vegetation structure on lidar-derived canopy height and fractional cover in forested riparian buffers during leaf-off and leaf-on conditions. *PLoS ONE*, 8(1), e54776.
- Whitcomb, J., Moghaddam, M., McDonald, K., Kellendorfer, J., & Podest, E. (2009). Mapping vegetated wetlands of Alaska using L-band radar satellite imagery. *Canadian Journal of Remote Sensing*, 35(1), 54–72.
- Whitehurst, A., Swatantran, A., Blair, J., Hofton, M., & Dubayah, R. (2013). Characterization of Canopy Layering in Forested Ecosystems Using Full Waveform Lidar. *Remote Sensing*, 5(4), 2014–2036. doi:10.3390/rs5042014
- Widlowski, J. L., Taberner, M., Pinty, B., Bruniquel-Pinel, V., Disney, M., Fernandes, R., et al. (2007). Third Radiation Transfer Model Intercomparison (RAMI) exercise: Documenting progress in canopy reflectance models. *Journal of Geophysical Research*, 112(D9), D09111. doi:10.1029/2006JD007821
- Wolf, A., Ciais, P., Bellassen, V., Delbart, N., Field, C. B., & Berry, J. A. (2011). Forest biomass allometry in global land surface models. *Global Biogeochemical Cycles*, 25(3), GB3015.
- Wolfe, B., Edwards, T., Aravena, R., Forman, S., Warner, B., Velichko, A., & MacDonald, G. (2000). Holocene paleohydrology and paleoclimate at treeline, north-central Russia, inferred from oxygen isotope records in lake sediment cellulose. *Quaternary Research*, 53, 319–329.
- Woodcock, C. E. (2006). Uncertainty in remote sensing. In G. M. Foody & P. M. Atkinson, *Uncertainty in remote sensing and GIS* (pp. 19–24). Wiley Online Library.
- Wulder, M. A., & Seemann, D. (2003). Forest inventory height update through the integration of lidar data with segmented Landsat imagery. *Canadian Journal of Remote Sensing*, 29(5), 536–543.
- Wulder, M., Han, T., White, J., Sweda, T., & Tsuzuki, H. (2007). Integrating profiling LIDAR with Landsat data for regional boreal forest canopy attribute estimation and change characterization. *Remote Sensing of Environment*, 110(1), 123–137.
- Xiaodong, Y., & Shugart, H. H. (2005). FAREAST: a forest gap model to simulate dynamics and patterns of eastern Eurasian forests. *Journal of Biogeography*, 32(9), 1641–1658. doi:10.1111/j.1365-2699.2005.01293.x
- Xue, B.-L., Kumagai, T., Iida, S., Nakai, T., Matsumoto, K., Komatsu, H., et al. (2011). Influences of canopy structure and physiological traits on flux partitioning between understory and overstory in an eastern Siberian boreal larch forest. *Ecological Modelling*, 222(8), 1479–1490. doi:10.1016/j.ecolmodel.2011.01.021
- Yi, D., Zwally, H. J., & Sun, X. (2005). ICESat measurement of Greenland ice sheet surface slope and roughness. *Annals of Glaciology*, 42(1), 83–89.
- Zhang, N., Yasunari, T., & Ohta, T. (2011). Dynamics of the larch taiga–permafrost coupled system in Siberia under climate change. *Environmental Research Letters*, 6(2), 024003. doi:10.1088/1748-9326/6/2/024003
- Zhang, Y. (2004). Sublimation from snow surface in southern mountain taiga of eastern Siberia. *Journal of Geophysical Research*, 109(D21), D21103. doi:10.1029/2003JD003779
- Zolkos, S. G., Goetz, S. J., & Dubayah, R. (2010). A meta-analysis of terrestrial aboveground biomass estimation using lidar remote sensing. *Remote Sensing of Environment*, 128, 1–10. doi:10.1016/j.rse.2012.10.017
- Zwally, H. J., Schutz, B., Abdalati, W., Abshire, J., Bentley, C., Brenner, A., et al. (2002). ICESat's laser measurements of polar ice, atmosphere, ocean, and land. *Journal of Geodynamics*, 34(3), 405–445.